Shelf biogeochemical interactions and feedback processes in the Benguela upwelling system

Thulwaneng Mashifane

A thesis presented for the degree of
Doctor of Philosophy
June 2017

Department of Oceanography
University of Cape Town
South Africa

Abstract

Two coupled physical–biogeochemical models namely, (Regional Ocean Modelling System and Biogeochemical of Eastern Boundary Upwelling Systems) ROMS–BioEBUS (3D) and (Nucleus for European Modelling of the Ocean and Biogeochemical Flux Model) NEMO–BFM (1D) are applied in the Benguela upwelling system to understand biogeochemical interactions and their related feedback processes. The models are formulated differently but achieve similar objectives with respect to the physics and biogeochemistry. The BioEBUS model is used to simulate nitrogen processes under oxic and suboxic conditions in upwelling systems with no option for other cycles. Intermediary nitrogen processes, nitrous oxide production and nitrogen loss mechanisms are studied using this model. Physical and advection processes that drive the oceanic nitrogen cycle in the region are also studied with BioEBUS. The BFM is used to understand the implications of the nitrogen loss and suboxic–anoxic conditions on related biogeochemical cycles. The 1D model was selected for its low computational costs and flexibility for addition of new code. BFM includes the carbon, nitrogen, phosphorus, silicate, iron cycles and hydrogen sulphide production, which is a known occurrence in the Namibian shelf waters. New variables, nitrite and nitrous oxide production, are added in BFM to complete the nitrogen cycle. The nitrification process in BFM is also formulated in two stages as in BioEBUS to obtain comparative results in both models. Both models are compared and validated with data from the Maria S. Merian (MSM) 19/1b cruise and available products respectively. Simulated results from BioEBUS show primary and secondary nitrite maxima in the Benguela shelf waters. The primary nitrite maxima are attributed to nitrification and nitrate assimilation. Secondary nitrite maxima accumulate in the Angola–Benguela Front (ABF) oxygen minimum zone (OMZ) and are attributed to denitrification. Off Walvis Bay, these secondary nitrite maxima and ammonium are though to be consumed by high rates of anaerobic ammonium oxidation (anammox). The nitrite maxima are restricted to the shelf off Walvis Bay and advected offshore in the ABF region. Interchanges between the poleward South Atlantic Central Water (SACW) and the equatorward, well–oxygenated Eastern South Atlantic Central Water (ESACW) drive the seasonality of nitrogen processes in the Benguela. Nitrous oxide concentrations are high in the ABF as a result of nitrification and accelerated production under suboxic conditions. Off Walvis Bay, nitrous oxide production is low when compared to the ABF. Nitrous oxide production in the ABF occurs in thermocline, intermediate and deeper water masses. Off

Walvis Bay, nitrous oxide production in deeper water masses is missing because of the shallow coast. High fixed nitrogen fluxes in the Benguela are attributed to nitrification rather than anammox and denitrification. Simulated results show denitrification to be the dominant nitrogen loss mechanism in the Benguela shelf waters. Simulated results from BFM show higher nitrogen uptake rates than phosphate in shelf and offshore stations. The uptake rates are high on the shallow shelf due to luxury nutrient uptake. High N:P ratios occur at the stations at 21°S than off Walvis Bay and are attributed to the presence of nutrient–rich, oxygen depleted SACW and denitrification respectively. Increased fixed nitrogen deficits (N*) occur in surface and subsurface waters at shallow stations as opposed to offshore. The positive N* anomalies off Walvis Bay are attributed to organic matter remineralization in deep, offshore stations. In contrast, increased phosphate (P*) concentrations occur in surface and subsurface waters. Phosphate is regenerated in subsurface waters and released under suboxic–anoxic conditions increasing P* concentrations. Nitrogen loss coupled with hydrogen sulphide production accelerate phosphate release in suboxic–anoxic bottom waters. The N:P stoichiometry, uptake rates, N* and P* concentrations appear to have considerable implications on potential estimated nitrogen fixation in the Benguela. BFM results suggest that the Benguela is a system characterized by excess nitrate in relation to silicate. This has been drawn from the low Si:N ratios observed at the simulated stations. A secondary Si:N peak is shown on the shallow coast due to high denitrification rates in suboxic waters. Note that high silicate concentrations occur in suboxic conditions and can be attributed to organic matter remineralization. The high silicate concentrations in the well-oxygenated offshore station are linked to sinking particles in deep waters. Increased silicate dissolution occurs in warm, surface waters and the particles that pass through the water column undissolved settle at the bottom where dissolution continues. From these results, it can be assumed that increased warming in the Benguela coastal waters should result in silicate being a limiting nutrient. This could affect carbon export as it has been shown that increased POC export is high in coastal waters due to ballasting of diatom biomass. The models used in this study simulated biogeochemical interactions in the Benguela fairly–well and can be applied in other regions.

Supervisors

Associate Professor. Marcello Vichi
Department of Oceanography, University of Cape Town, South Africa

Dr. Howard Waldron
Department of Oceanography, University of Cape Town, South Africa

Dedicated to the memory of my beloved Grandmother Mankepile Makweng (1936/03/22 – 2016/10/15) who to us was the epitome of strength and resilience.

"Robala ka khutšo Hunadi á Kanyane..."

Acknowledgments

Firstly, I would like to express my sincere gratitude to my supervisor A/Prof. Marcello Vichi for the continuous support of my PhD study and related research, for his patience and sharing knowledge in biogeochemical modelling. I would also like to thank my co–supervisor Dr. Howard Waldron for giving me the opportunity to start this PhD in the first place before handing over.

In addition to my supervisors, I would also like to thank Dr. Jennifer Veitch for her initial involvement in this thesis and helping me source funding for my studies. I would also like to thank Dr. Eric Machu for his interest in my topic and providing the initial model data to get things going. Special thanks to Dr. Veronique Garcon, for her insightful comments and discussions during her visit to UCT.

I would like to thank the crew of the Maria S. Merian for assistance during the SPACES training and capacity building cruise during October 2011. The data collected during this cruise was valuable as my thesis questions and hypotheses were formulated after participating in this cruise. Appreciation goes to Csilla Kovacs for technical assistance and guidance during on–board laboratory analysis of nutrient samples during this cruise.

I thank my fellow colleagues, Moagabo Ragoasha, Ngwako Mohale, Juliano Ramanantsoa and all of my friends in the Oceanography department for encouragement and informal discussions during tea–time and outings. Special thanks to everyone who has ever shared working space with me in office 118. There has been a lot of coming and going but the mood in the office was always cheerful.

Lastly, I would like to thank my family: my parents and to my brother Dipoo Mashifane for supporting me throughout this journey and my life in general. To Thabiso Moela, thank you for the good memories, for believing in my dreams and always managing to put a smile on my face when I was down and tired. I would not have reached this far without your patience, kind words and encouragement when I faced adversity. To my beautiful daughter, Goapele, your smile and giggles have made my worries disappear since the day you were brought into this world. You are the center of my universe.

Declaration

I, Thulwaneng Mashifane, declare that the above thesis is my own unaided work, both in concept and execution. In this work I largely used existing model software but I installed the models, designed and ran the simulations. Apart from the normal guidance from my supervisors, I have received no assistance except as stated below:

- The initial BioEBUS model data was provided by IRD but did not include biological diagnostics. I designed and ran the high resolution simulation to calculate the biogeochemical rates and fluxes.

- Scientific discussions and thesis corrections.

Neither the substance nor any part of the above thesis has been submitted in the past, or is being, or is to be submitted for a degree at this University or at any other university.

This work was funded by:

- National Research Foundation and German Academic Exchange Service (NRF–DAAD) In–Country Ph.D. scholarship.
- University of Cape Town Science Faculty Equity Ph.D. fellowship.

Publication based on this work:

- Mashifane T.B., M. Vichi, H.N. Waldron, E. Machu and V. Garon, 2016, Modeling nitrite dynamics and associated feedback processes in the Benguela oxygen minimum zone, Continental Shelf Research, 124:200–212.

Contents

List of Figures

List of Tables

1 | Aim and objectives

The main aim of this thesis is to investigate multiple biogeochemical interactions in the Benguela oxygen minimum zone (OMZ) using coupled physical–biogeochemical models. The model results are initially compared to available in–situ data to validate and compare how close the models are to measurements in order to achieve the set objectives. As such, the first objective of this study is to investigate the nitrogen species including nitrite, ammonium and nitrous oxide in the Benguela to understand their dynamics and dominant production and consumption processes. The majority of models focus on nitrogen species, while the OMZ mediates the cycle of other elements such as phosphorus and silica. These cycles link within the OMZ and it is important to understand how the nitrogen loss affect these implementing the current parameterization in models. Therefore the second objective is to establish the dominant nitrogen loss mechanism in the Benguela and link this to the cycling of the selected cycles. Phosphorus is regenerated from organic matter by heterotrophic bacteria during denitrification. Most cycling and transformation of phosphorus occur in the upper water column including within the OMZ (Paytan and McLaughlin, 2007). In a system where nitrogen loss is known to occur, it is important to investigate potential implications of this on N:P stoichiometry, phosphate release under suboxic conditions and nitrogen fixation.

The silica cycle is linked to the nitrogen and phosphorus cycles through marine primary productivity and the export of carbon to the deep sea (Pondaven et al., 2000). Silica dissolution is mainly controlled by the thermodynamics of solubility, sinking rates of particles, and degradation of organic matter (Bidle and Azam, 1999). Seabeds below OMZs have been found to receive high organic matter inputs from the productive surface waters (Gibson and Atkinson, 2003). This has been attributed to less efficient degradation of organic matter by microbes under anaerobic conditions (Fenchel and Finlay, 1995). It is not known, how factors that control silica dissolution, particularly degradation of organic matter, affect silica cycling in OMZs. The impact of the nitrogen loss on Si:N stoichiometry and biogenic silica concentrations in the OMZ is also not well–documented. As such, the last objective of this study is to investigate Si:N ratios, silica dissolution, biogenic silica production and its contribution to the export of carbon in the Benguela OMZ.

2 | General introduction

The Benguela is an Eastern boundary upwelling system (EBUS) located along the south–western shelf of Africa. It extends from Cape point along the coast of South Africa through the Namibian shelf to the location of the Angola–Benguela Front (ABF) at 16°S in the north. The Benguela is divided into two subsystems by an area of permanent upwelling off Lüderitz. The Benguela occupies a width about 200 to 300 km on the South African and Namibian continental shelf area. The inner and outer continental shelf regions of the Benguela are separated by an estimated distance of 100 km (Carr and Kearns, 2003). The inner shelf width extends to about 100 km and the outer shelf is wider and extends beyond 200 km between 28°S and 32°S. Three main upwelling centers located in Lüderitz, Walvis Bay and Cape Frio control upwelling of South Atlantic Central Waters (SACW) in the Northern Benguela subsystem (Rae, 2005). The southern subsystem consists of the Cape Peninsula, Cape Columbine and Namaqua upwelling centers. The narrow shelf in the northern Benguela results in extensive upwelling (Monteiro and van der Plas, 2006) and consequently, the northern Benguela is estimated to account for 80% of the total upwelled flux in the Benguela (Liu et al., 2010). Maximum biomass in the Benguela is observed where the continental shelf is widest (Carr and Kearns, 2003).

Combined estimated potential production from all four major Eastern Boundary upwelling systems (EBUS) using satellite measurements of ocean color, sea surface temperature, and photosynthetically available radiation is $\sim$ 1 Gt C yr^{-1} (Carr, 2001). Atlantic EBUS are more productive than the Pacific and more sensitive to upwelling favorable winds because of weaker factors inhibiting net primary productivity (Lachkar and Gruber, 2012). These inhibiting factors in EBUS include strong eddy activity, narrow continental shelf, and a deep mixed layer (Lachkar and Gruber, 2012). These factors were found to be weak in the south Atlantic, hence the Benguela has been estimated to be 30–65 times more productive per unit area than the global ocean. Increased primary productivity in EBUS supports major fisheries and plays an important role in ocean nutrient cycles. The high productivity in EBUS also provide the basis for carbon export, therefore reducing the warming effects of carbon dioxide from the atmosphere (Muller-Karger et al., 2005). While the upwelling events promote carbon export, the deeper nutrient rich waters with limited oxygen combined with increased biological oxygen demand create OMZs along the continental shelf.

2.1 Wind field

The high pressure system over the central south Atlantic ocean gyre induces south–easterly trade winds which are influenced by seasonal low pressure over the continent (Nelson and Hutchings, 1983). The Scattered Climatology of Ocean Winds (SCOW) is used to identify annual wind stress patterns in the Benguela (Figure 2.1). The strong and persistent meridional wind stress patterns in the Benguela region result in two distinct and dominant regions of intense annual wind stress. The persistent meridional wind stress is located in the area off Cape Frio and Lüderitz on the Namibian shelf. At a broader scale, annual zonal wind stress in the Benguela is generally weak and characterized by a negative wind stress off the Namibian coast. Regions of weak positive wind stress are identified north of Cape Frio, off Walvis Bay and St Helena Bay. A distinct seasonal cycle of meridional wind stress is observed off Cape Frio and Walvis Bay (Figure 2.2a). The monthly meridional wind stress off Cape Frio peaks during autumn and spring, then weakens during winter and decreases rapidly during austral summer (December to February). Monthly meridional wind stress off Walvis Bay intensifies earlier during autumn (March) and spring (September to October). Similarly, meridional wind stress declines earlier during winter (June). In contrast, meridional wind stress off Walvis Bay does not decline as rapidly as off Cape Frio during summer.

Monthly zonal wind stress off Cape Frio increases steadily during winter and maximal during spring (September)(Figure 2.1b). The increased negative wind stress in this region transforms into a strong Ekman offshore transport (Mohrholz et al., 2001). The monthly zonal wind stress off Walvis Bay follows a similar trend but it is generally weaker and reaches a maximum during late winter (August). The wind stress patterns translate into south–easterly trade winds that drive upwelling of deeper, nutrient rich water in the Benguela (Andrews and Hutchings, 1980; Shannon and Nelson, 1996). Upwelling in the northern Benguela peaks during autumn (March to May) and spring (September to November) in response to intensifying wind stress. The central Benguela region located off Lüderitz experiences perennial upwelling–favoring winds (Shannon, 1985; Shannon and Nelson, 1996).

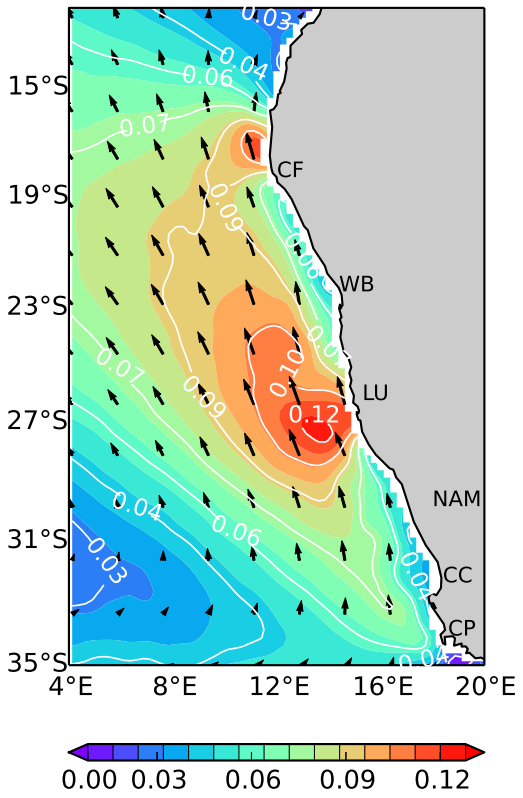

Figure 2.1: Mean annual wind stress [N m^{-2}] in the Benguela derived from SCOW. Locations: CF–Cape Frio, WB–Walvis Bay, LU–Lüderitz, NAM–Namaqua, CC–Cape Columbine and CP–Cape Peninsula.

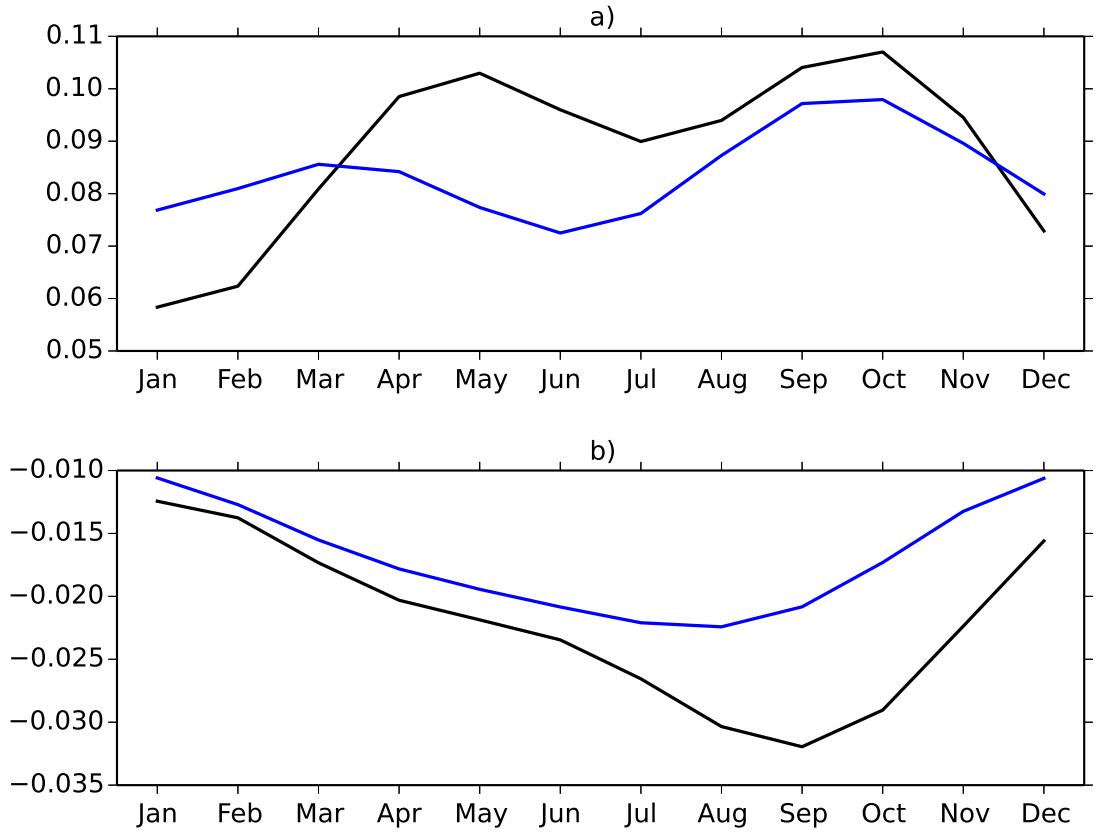

Figure 2.2: Monthly mean annual (a) meridional and (b) zonal wind stress [N m^{-2}] off Cape Frio (black) and Walvis Bay (blue) derived from SCOW.

2.2 General circulation and water masses

Major current systems that influence the Benguela are the eastern boundary current of the south Atlantic (Benguela Current – BC), the cyclonic equatorial circulation in the Angola gyre and the Agulhas current (Rae, 2005). Local circulation of these three major currents control transport and distribution of different thermocline waters in the Benguela (Figure 2.3). The large scale circulation controls distribution of polar intermediate and bottom waters in the Benguela. Thermocline water masses present in the system include tropical and subtropical surface waters, Angola gyre South Atlantic Central Water (SACW) and Cape basin Eastern South Atlantic Central Water (ESACW) (Shannon and Nelson, 1996). Polar water masses include Antarctic Intermediate Water (AAIW), North Atlantic Deep Water (NADW) and Antarctic Bottom Water (ABW). From the north, the Benguela is characterized by poleward flow of warm, nutrient–rich, oxygen–depleted SACW from the Angola gyre also known as the Angola Current (AC). The AC is diverted offshore by southerly winds around 10°S (Mohrholz et al., 2001).

The AC converges with the BC between 15–18°S at the ABF zone (Mohrholz et al., 2008). Poleward flow of oxygen–depleted SACW is prevented by the Lüderitz upwelling cell at 27°S (Rae, 2005). South of the Lüderitz upwelling cell, the equatorward flowing BC dominates. The BC transports well–oxygenated ESACW, formed in the Cape basin by a combination of SACW from the subtropical gyre and Indian Ocean thermocline water transported into the south Atlantic through the Agulhas current retroflection. The smooth transition area (off Walvis Bay) separating the AC and BC lies between the ABF zone and the Lüderitz upwelling cell (Mohrholz et al., 2008). This creates special suite of biogeochemical conditions on the Namibian shelf. Together with the region of intense wind stress located off Cape Frio, it provides a natural laboratory that can be used to understand complex processes in the Benguela.

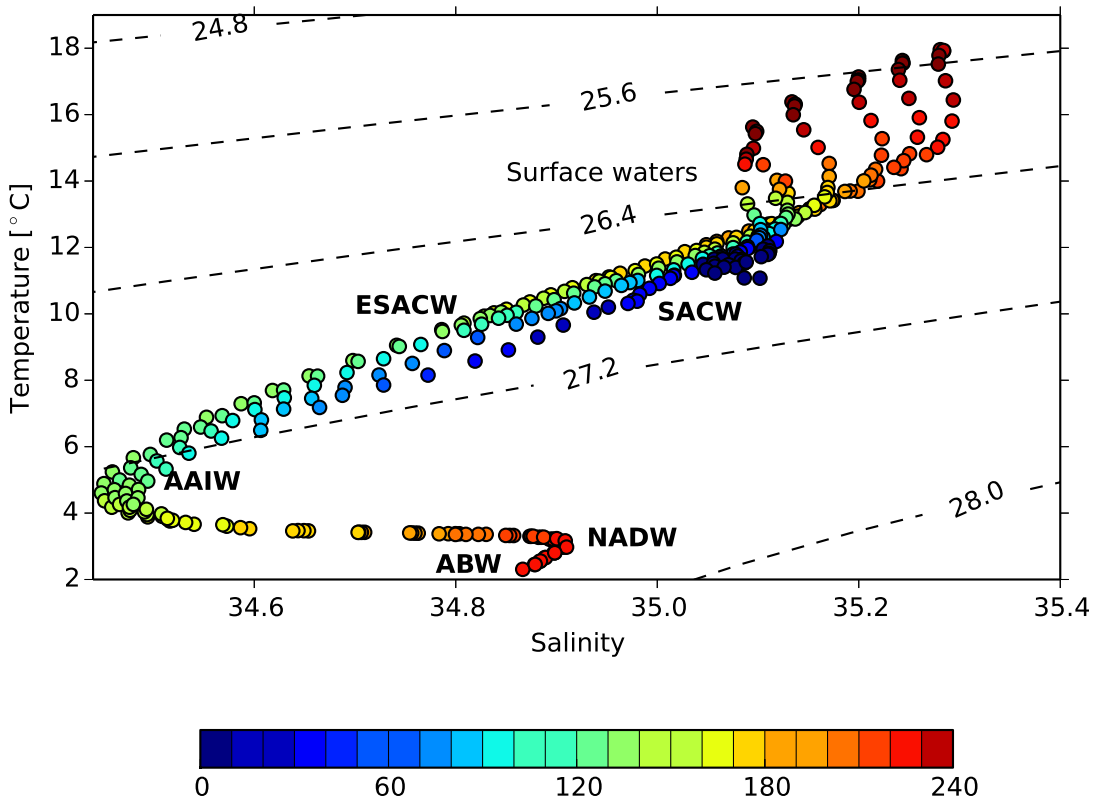

Figure 2.3: TS diagram of water masses along 23°S, 11.5–14.5°E in the Benguela from CARS. The water masses found in the region are: ABW–Antarctic Bottom Water; NADW–North Atlantic Deep Water; AAIW–Antarctic Intermediate Water; Eastern South Atlantic Central Water; SACW–South Atlantic Central Water and surface waters. The colorbar represents oxygen concentrations [mmol O_2 m^{-3}] of the water masses to highlight oxygen–depleted SACW from the Angola gyre and well–oxygenated ESACW from the Cape Basin.

The Walvis Bay monitoring line (at 23°S) which is positioned between this transition has been used to understand the physics and biogeochemistry of the Benguela over the years. More specifically, this region has been the focus to understand low oxygen concentrations and the biogeochemical processes involved (Monteiro and van der Plas, 2006; Kuypers et al., 2005). The shelf area in this region is dominated by poleward flow of the SACW during austral summer (Mohrholz et al., 2008). Ventilation of the shelf occurs during winter when the well–oxygenated ESACW flow equatorward.

2.3 Low oxygen formation and OMZ distribution in the Benguela

During upwelling, water enriched with nutrients reaches the biologically productive surface of the ocean enhancing phytoplankton production. Phytoplankton blooms resulting from these upwelling events provide the biological basis for transporting fixed carbon into the deep ocean (Longhurst, 1991). This is achieved by carbon fixation (photosynthesis) and the processes of export of cells into the deep ocean as particulate organic matter (Lampitt et al., 2008). The rate at which phytoplankton cells and other particles sink depends on size. Large diatoms typically sink faster than small cells. Carbon can be lost rapidly from the surface layers into the deep ocean due to fast sinking rates when these large, heavy diatoms die and sink as organic matter (Salter et al., 2007). The grazing impact of microzooplankton and respiration requirements of mesozooplankton also contribute to carbon fluxes and these are dependent on the community structure (Steinberg and Landry, 2017). While upwelling events promote carbon fixation, the deeper water with limited oxygen exchange create hypoxic areas called OMZs on the continental shelf. The upwelled water is exposed to a mass of dead, decaying matter as it moves into the thermocline and oxygen depletion occurs when sinking organic matter is decomposed by bacteria in the water column. OMZs occur as permanent, seasonal or episodic features and show a general oxygen profile with regional differences in levels of oxygen, thickness and extent of depth (Gibson and Atkinson, 2003). OMZs are common in highly productive EBUS, the Benguela included. The OMZ in this study is defined as oxygen concentrations below 60 mmol O_2 m^{-3}. The Benguela OMZ is estimated to extend from 50 to 500 m in oceanic waters (Ekau et al., 2010). The OMZ extends from the continental shelf to oceanic waters off Cape Frio in the ABF region (Figure 2.4a). Off Walvis Bay, the OMZ is restricted to the shallow continental shelf slope. (Figure 2.4b).

The dominant processes that drive the formation of low oxygen water in the Benguela and the eastern tropical south Atlantic (ETSA) oceanic region occur in the Angola gyre (Monteiro and van der Plas, 2006). Increased phytoplankton new production, a thermocline that limits downward flux of oxygen and a retention zone that limits ventilation in the gyre lead to the formation and maintenance of these low oxygen waters (Monteiro and van der Plas, 2006). The poleward flowing Angola Current transports the low oxygen water from the gyre into the northen Benguela (Mohrholz et al., 2001). Upwelling of these waters onto the shelf has been identified as one of the main sources of oxygen–depleted water in

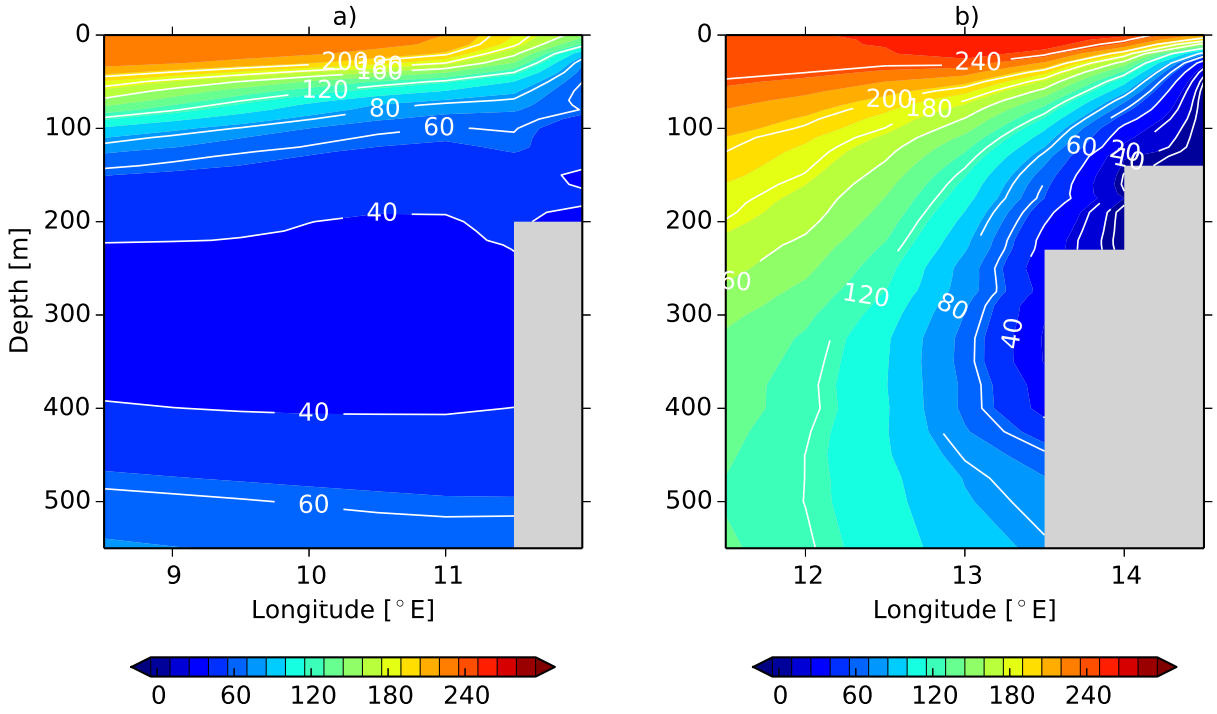

Figure 2.4: Vertical distribution of annual mean oxygen concentrations [mmol O_2 m^{-3}] off (a) Cape Frio and (b) Walvis Bay from CARS.

the northen Benguela (Monteiro and van der Plas, 2006). In addition to poleward flow of oxygen–depleted waters, hypoxic conditions on the shelf occur during consumption of organic matter by bacteria following upwelling events (Dittmar and Birkicht, 2001). These processes lead to the formation and maintenance of the OMZ in the northern Benguela. The formation of low oxygen water on the Namibian shelf is controlled by boundary conditions and interchanges between ESACW and SACW from the Lüderitz and Cape Frio upwelling centers, respectively (Monteiro and van der Plas, 2006). Local biogeochemical processes and increased respiration from higher temperatures also contribute to oxygen consumption in coastal waters (Carstensen et al., 2014). Low oxygen water formation in the southern Benguela is controlled by local physical and biogeochemical processes (Monteiro and van der Plas, 2006). Stratification, retention and phytoplankton new production drive the formation of low oxygen water in this region.

Hypoxic ($<$ 20 mmol O_2 m^{-3})conditions during late austral summer (February–April) in the Benguela lead to the production of hydrogen sulphide in bottom layers. Regular eruptions of methane and hydrogen sulphide occur and lead to persistent water column

hypoxia. Hydrogen sulphide production rarely occurs in the water column of the North Pacific and the Arabian Sea even though the water masses there are older and have lower oxygen content (Morrison et al., 1999). Hydrogen sulphide builds up in the OMZ sediments in these regions but it does not reach high levels as the sulphide is often oxidized with iron or exhausted by sulphide oxidizing bacteria (Gibson and Atkinson, 2003). This is an occurrence observed in EBUS including off Peru (Schunck et al., 2013). Sulfidic waters which support plumes of chemolithoautotrophic bacteria have also been reported in the Baltic and Black seas (Glaubitz et al., 2009, 2010). Episodic, vertical mixing events are responsible for the occasional release of the hydrogen sulphide into the surrounding atmosphere of OMZ waters off Walvis Bay (Weeks et al., 2002). The persistent water column hypoxia from sulphide eruptions causes displacement and mass mortalities of living marine resources (Shannon et al., 2006).

The shelf area off St Helena Bay (30–33°S), South Africa is the main generation zone of low oxygen water in the southern Benguela due to local retention. Oxygen data from 1950–2011 obtained during demersal and pelagic fisheries surveys, and the monthly monitoring line off St Helena bay show that the oxygen–depleted water are restricted to bottom depths (<150 m) (Jarre et al., 2015). Hypoxic events in this region occur during austral summer and autumn following upwelling that creates a persistent cyclonic circulation that limits oxygen exchange (Monteiro and Roychoudhury, 2005). Low oxygen events in the southern Benguela are episodic and not as intense as in the northern subsystem, hence this thesis is focusing on the OMZ off Namibia and Angola.

2.4 Biogeochemical implications of the OMZ in the Benguela

The loss of nitrogen in OMZs through anammox and denitrification could easily affect related cycles. This is possible since the nitrogen cycle is closely linked to the silica and phosphorus cycles through various feedback loops. For example, the consumption of organic matter by denitrifying bacteria regenerates inorganic nutrients including phosphate, carbon dioxide and ammonium. Silica is a key element required for the growth of diatoms, and it is therefore closely related to the other nutrient cycles through marine primary production and the export of carbon to the deep sea (Tréguer and De La Rocha, 2013). The feedback loops through which these nutrient cycles link are still being understood and could be further complicated by OMZs. The discovery of nitrogen fixing microbes and anammox in the nitrogen cycle (Dalsgaard et al., 2005; Kuypers et al., 2005; Hamersley et al., 2007; Ward et al., 2009; Zehr et al., 2001), and silica cycling (Honjo et al., 2008; Nelson et al., 2002;

Tréguer and De La Rocha, 2013) both pointed out large uncertainties in our understanding of these cycles. The recently revisited silica cycle notes that the recycling of silica occurs mostly at the sediment–water interface and not during the sinking of particles through deep waters as previously understood (Honjo et al., 2008; Nelson et al., 2002; Tréguer and De La Rocha, 2013). This implies that only a small fraction of the biogenic silica produced by siliceous organisms is directly recycled in the photic zone (Tréguer and De La Rocha, 2013). The dissolution of biogenic silica throughout the water column is mainly controlled by thermodynamics of solubility, sinking rates of particles, and bacterial degradation of organic matter (Bidle and Azam, 1999). Little is known how these factors, particularly degradation of organic matter, affect silica dissolution in OMZs. The phosphorus cycle, on the other hand, could be more susceptible to OMZs as most of its cycling and transformations occur predominantly in the upper water column (Paytan and McLaughlin, 2007).

From 1960 to 2006, regions of low oxygen ($O_2 < 70$ mmol m^{-3}) in the tropical Atlantic have reportedly thickened vertically from 370 to 690 m and spatially extended by 4.5 million km^2 (Stramma et al., 2008). Two long term trends that might result in an intensified seasonal hypoxia in the Benguela have also been documented (Monteiro et al., 2008). The trends include a warming at the Angola Benguela front and an increase in the lag between seasonal warming at Cape Frio and the following upwelling peak at the Luderitz cell. These trends are consistent with global warming and may lead to intensified hypoxia and a decline in ecosystem function (Ekau et al., 2010; Stramma et al., 2010). Oxygen–deficient waters in the Baltic Sea have been reported to have expanded from 5000 to over 60 000 km^2 over the last century with large decadal fluctuations observed (Carstensen et al., 2014). The oxygen content in the global ocean has reportedly decreased by 2% ($4.8 \pm 2.1 \times 10^{15}$ mol) from $227.4 \pm 1.1 \times 10^{15}$ mol since 1960 (Schmidtko et al., 2017). This decrease varies at depth in the different ocean basins and attributed to decreased solubility and biological consumption in the upper water column. The oxygen change in the south Atlantic is estimated to be -129±27 Tmol per decade (Schmidtko et al., 2017). With regions of low oxygen expanding in the ocean, it is becoming increasingly important to understand and incorporate revised processes into nutrient cycles. Because of the dynamic nature of the Benguela, it is predicted that the mid–depth OMZs alter biogeochemical cycles with feedback processes unique to the system.

3 | Numerical modeling of the Benguela upwelling system

Two coupled physical–biogeochemical models namely, ROMS–BioEBUS and NEMO–BFM are applied in the Benguela to understand biogeochemical interactions and their related feedback processes. Both models are formulated differently but achieve similar objectives with respect to the physics and biogeochemistry. The ROMS–BioEBUS model is designed to simulate nitrogen processes in OMZs. The suboxic, hypoxic and anoxic conditions in this study are defined as oxygen concentrations between 20–60, ≤ 20 and 0 mmol O_2 m^{-3} respectively. The BioEBUS model was adjusted to satisfactorily reproduce estimations of nitrogen species in the Namibian shelf (Gutknecht et al., 2013). A detailed validation of the model has been performed using available in situ and satellite data (Gutknecht et al., 2013). Sensitivity analyses of key BioEBUS parameters have also been performed and different nitrous oxide parameterizations tested to adjust the model. The reference simulation in the above–mentioned study has been found to compare well with the available data and it is used as the default model with ROMS. Therefore, it is proposed that this model provides an opportunity to understand nitrogen processes that have been a subject of debate in this region. In particular, the model could advance knowledge about nitrogen loss pathways and production of the greenhouse gas, nitrous oxide in the Benguela upwelling system. Previous studies have investigated denitrification and anammox as dominant nitrogen loss mechanisms in EBUS with conflicting results as discussed in Chapter 4. This study aims to use the BioEBUS model with available data and known literature to provide more knowledge on these processes in the Benguela.

Since only nitrogen and oxygen are considered in BioEBUS, an additional model is needed to understand implications of the nitrogen loss on related biogeochemical cycles. The NEMO 1D version coupled with BFM is used in this instance. The 1D model has been selected for its low computational costs and flexibility for addition of more code. The BFM includes the carbon, phosphorus, silicate and iron cycles and therefore provides more options for understanding interactions and feedback processes between biogeochemical cycles in the ocean. Production of hydrogen sulphide is known to occur in the Namibian shelf waters (Lavik et al., 2009; Weeks et al., 2002). The BFM model includes a variable termed "reduction equivalents" assumed to be similar to hydrogen sulphide production under suboxic and anoxic conditions (Vichi et al., 2015). Since hydrogen sulphide production

is coupled to denitrification, it can also be linked to phosphate release under low oxygen conditions. Most importantly the BFM provides an opportunity to understand nutrient stoichiometry and implications of the phosphorus cycle on nitrogen fixation in the Benguela. New variables are introduced in the BFM in this study to get the model to simulate nitrogen processes like BioEBUS. Nitrite is introduced and nitrification is implemented in two stages as described later. Nitrous oxide production under oxic and suboxic conditions is also introduced. The 1D model has unlimited potential and can be used in open ocean and coastal regions to estimate biogeochemical rates not measured during sampling. Measured physical and biogeochemical concentrations from long–term and anchor stations can be combined with atmospheric fluxes in the model to calculate rates and predict future scenarios. In this study, data from selected stations during the MSM 19/1b cruise is used to understand biogeochemical interactions. Since the data are limited, objectively analyzed climatology widely used in ocean models is used as a supplementary.

3.1 3D coupled physical–biogeochemical model

The hydrodynamic Regional Ocean Modeling System (ROMS) coupled with BioEBUS is used in a 3D realistic physical–biogeochemical configuration of the Benguela upwelling system. ROMS is an explicit free surface ocean model based on a sigma coordinate system for vertical discretization (Shchepetkin and McWilliams, 2005). Primitive equations in the model are solved in a rotating frame following the Boussinesq and hydrostatic assumptions. The equations are also solved using third–order precision advection schemes in space and time. Unresolved, vertical mixing processes in ROMS are parametized according to a non–local K–Profile Parameterization (KPP) boundary layer scheme (Large et al., 1994). The BioEBUS model is a nitrogen based model developed for simulating main processes in EBUS and associated OMZs (Gutknecht et al., 2013). Evolution of the biological tracer concentration (C_i) in the model is determined through the advective–diffusive equation:

$$\partial C_i \partial t = -\nabla \cdot (\boldsymbol{u} C_i) + K_h \nabla^2 C_i + \frac{\partial}{\partial z}(K_z \frac{\partial C_i}{\partial z}) + \mathrm{SMS}(C_i) \tag{3.1}$$

Advection in the equation is represented by the velocity vector ($\boldsymbol{u}$). Horizontal diffusion and vertical mixing are represented through the horizontal eddy (K_h) and turbulent (K_z) diffusion coefficients respectively. Biological activity of the biological tracer is represent through the "source–minus–sink" (SMS) term.

The BioEBUS model is mostly derived from the $N_2P_2Z_2D_2$ model by (Koné et al., 2005) which was tested in the southern Benguela. The model contains 12 state variables: phytoplankton (P_S and P_L) split into flagellates and diatoms, nitrate, nitrite, ammonium, zooplankton (Z_L and Z_S) as ciliates and copepods, large and small detritus (D_L and D_S), dissolved organic nitrogen (DON), dissolved oxygen and nitrous oxide. Dissolved inorganic nitrogen (DIN) pool in the model is represented by nitrite, nitrate and ammonium. The nitrite equation has been included in the model to give a detailed description of microbial nitrogen processes under oxic (ammonification and nitrification) and suboxic (anammox and denitrification) conditions (Gutknecht et al., 2013). The SMS terms for nitrogen tracers in BioEBUS are formulated as follows:

$$\mathrm{SMS(DON)} = \varepsilon_{\mathrm{P_S}} \cdot J_{\mathrm{P_S}}(\mathrm{PAR}, T, \mathrm{N}) \cdot [\mathrm{P_S}] + \varepsilon_{\mathrm{P_L}} \cdot J_{\mathrm{P_L}}(\mathrm{PAR}, T, \mathrm{N}) \cdot [\mathrm{P_L}] + f2_{\mathrm{Z_S}} \cdot \gamma_{\mathrm{Z_S}} \cdot [Z_S] + f2_{\mathrm{Z_L}} \cdot \gamma_{\mathrm{Z_L}} \cdot [\mathrm{Z_L}] + \mu_{\mathrm{D_S}} \cdot [\mathrm{D_S}] + \mu_{\mathrm{D_L}} \cdot [\mathrm{D_L}] - \mathrm{remDON} \tag{3.2}$$

$$\mathrm{SMS}(NO_3^-) = -[aJ_{\mathrm{P_S}}(\mathrm{PAR}, T) \cdot f'_{\mathrm{P_S}}(NO_3^-, NO_2^-, NH_4^+) \cdot [\mathrm{P_S}] + aJ_{\mathrm{P_L}}(\mathrm{PAR}, T) \cdot f'_{\mathrm{P_L}}(NO_3^-, NO_2^-, NH_4^+) \cdot [\mathrm{P_L}]] \cdot \frac{[NO_3^-]}{[NO_3^-]+[NO_2^-]} + \mathrm{Nitrif2} - \mathrm{Denitr1} \tag{3.3}$$

$$\mathrm{SMS}(NO_2^-) = -[aJ_{\mathrm{P_S}}(\mathrm{PAR}, T) \cdot f'_{\mathrm{P_S}}(NO_3^-, NO_2^-, NH_4^+) \cdot [\mathrm{P_S}] + aJ_{\mathrm{P_L}}(\mathrm{PAR}, T) \cdot f'_{\mathrm{P_L}}(NO_3^-, NO_2^-, NH_4^+) \cdot [\mathrm{P_L}]] \cdot \frac{[NO_2^-]}{[NO_3^-]+[NO_2^-]} + \mathrm{Nitrif1} - \mathrm{Nitrif2} + \mathrm{Denitr1} - \mathrm{Denitr2} - \mathrm{Anammox} \tag{3.4}$$

$$\mathrm{SMS}(NH_4^+) = -aJ_{\mathrm{P_S}}(\mathrm{PAR}, T) \cdot f''_{\mathrm{P_S}}(NH_4^+) \cdot [\mathrm{P_S}] - aJ_{\mathrm{P_L}}(\mathrm{PAR}, T) \cdot f''_{\mathrm{P_L}}(NH_4^+) \cdot [\mathrm{P_L}] + (1 - f2_{\mathrm{Z_S}}) \cdot \gamma_{\mathrm{Z_S}} \cdot [\mathrm{Z_S}] + (1 - f2_{\mathrm{Z_L}}) \cdot \gamma_{\mathrm{Z_L}} \cdot [\mathrm{Z_L}] - \mathrm{Nitirif1} + \mathrm{remD_S} + \mathrm{remD_L} + \mathrm{remDON} - \mathrm{Anammox} \tag{3.5}$$

Production of nitrous oxide in BioEBUS is formulated following (Suntharalingam et al.,

2000):

$$\mathrm{SMS}(N_2O) = \alpha \cdot (1.5 \cdot \mathrm{Nitrif1} + 0.5 \cdot \mathrm{Nitrif2}) + \beta \cdot (1.5 \cdot \mathrm{Nitrif2}) \cdot F_{O_2} \tag{3.6}$$

The equation allows for nitrous oxide production under oxygenated and low oxygen conditions below the euphotic zone. This is controlled through a non–dimensional regulating factor F_{O_2} where under oxygenated conditions:

$$F_{O_2} = [O_2]/O_{2_{\max}} \tag{3.7}$$

And under low oxygen conditions:

$$F_{O_2} = \exp[-K_{O_2}([O_2]) - O_{2_{\max}}/O_{2_{\max}}] \tag{3.8}$$

The β coefficient account for nitrous oxide production under suboxic and denitrification conditions as regulated with the F_{O_2} factor. Nitrous oxide loss through denitrification is represented below 5 mmol O_2 m^{-3} (Suntharalingam et al., 2012). The parametization of Nevison et al. (2003) and Suntharalingam et al. (2012) were tested in the Benguela using $\beta = 0.03$ mol N_2O mol N^{-1} (Gutknecht et al., 2013). The parametization of Suntharalingam et al. (2012) produces a significant nitrous oxide source when used in combination with the set of parameters in the default model. Nitrous oxide production through the Suntharalingam et al. (2012) also produce concentrations that are within range of in situ observations off the coast of Namibia hence it is used in the BioEBUS model (Gutknecht et al., 2013). Air–sea fluxes of nitrous oxide in BioEBUS are parameterized using the gas transfer velocity of Wanninkhof (1992).

The oxygen equation allows for nitrogen processes under oxic and suboxic conditions. Source and sink terms for oxygen in the model are photosynthesis, zooplankton respiration and bacterial remineralization. Sea–air oxygen fluxes at the ocean–atmosphere interface are represented through parameterization of Wanninkhof (1992) and the Schmidt number from Keeling et al. (1998).

$$\mathrm{SMS(O_2)} = R_{\mathrm{O_2}/N} \cdot (J_{\mathrm{P_S}}(\mathrm{PAR},\, T, \mathrm{N}) \cdot [\mathrm{P_S}] + J_{\mathrm{P_L}}(\mathrm{PAR},\, T, \mathrm{N}) \cdot [\mathrm{P_L}] - \mathrm{DcDON(O_2)} - \mathrm{DcD_S(O_2)} - \mathrm{DcD_L(O_2)} - (1 - f2_{\mathrm{Z_S}}) \cdot \gamma_{\mathrm{Z_S}} \cdot [\mathrm{Z_S}] - (1 - f2_{\mathrm{Z_L}}) \cdot \gamma_{\mathrm{Z_L}} \cdot [\mathrm{Z_L}]) - 1.5 \cdot \mathrm{Nitrif1} - 0.5 \cdot \mathrm{Nitrif2} + \mathrm{FluxOA(O_2)} \tag{3.9}$$

Phytoplankton growth rate $J_{\mathrm{P}_i}(\mathrm{PAR},\ T,\ \mathrm{N})$ is limited by light availability for photosynthesis (PAR), temperature (T) and nutrients (N) (Gutknecht et al., 2013). The term J represents phytoplankton light-saturation growth rate. It is assumed that phytoplankton growth rate is not limited by other macronutrients (phosphate and silicate) or micronutrients (e.g. iron) (Gutknecht et al., 2013). Decomposition (Dc) of detritus ($\mathrm{D_L}$ and $\mathrm{D_S}$) and dissolved organic matter (DON) under oxic conditions represents ammonification. Nitrification is considered through two stages with no light inhibition according to Yakushev et al. (2007) as:

$$\mathrm{Nitrif1} = \frac{K_{\mathrm{N42}} \cdot [\mathrm{O_2}]}{[\mathrm{O_2}] + \mathrm{O_2nf}} \cdot [\mathrm{NH_4^+}] \tag{3.10}$$

$$\mathrm{Nitrif2} = \frac{K_{\mathrm{N23}} \cdot [\mathrm{O_2}]}{[\mathrm{O_2}] + \mathrm{O_2nf}} \cdot [\mathrm{NO_2^-}] \tag{3.11}$$

Suboxic decomposition of particulate and dissolved organic matter through denitrification is also in two stages (Yakushev et al., 2007):

$$\mathrm{DcDet(NO_3)} = 0.5 \cdot \mathrm{Denitr1(Det)} + 0.75 \cdot \mathrm{Denitr2(Det)} \tag{3.12}$$

$$\mathrm{Denitr1(Det)} = K_{\mathrm{N32}} \cdot \mathrm{Fdnox} \cdot \mathrm{FdnNO_3} \cdot [\mathrm{Det}] \tag{3.13}$$

$$\mathrm{Denitr2(Det)} = K_{\mathrm{N24}} \cdot \mathrm{Fdnox} \cdot \mathrm{FdnNO_2} \cdot [\mathrm{Det}]$$

(3.14)

Where if $[O_2] > O_2dn$, then Fdnox = 0, and if $[O_2] \leq O_2dn$, then Fdnox = 1–$[O_2]/(O_2dn\cdot(O_2dn+1–[O_2]))$. If $[NO_3^-] \leq NO_3mi$, then $FdnNO_3 = 0$ and if $[NO_3^-] > NO_3mi$, then $FdnNO_3 = ([NO_3^-]–NO_3mi)/([NO_3^-]–NO_3mi+1)$. If $[NO_2^-] \leq NO_2mi$, then $FdnNO_2 = 0$ and if $[NO_2^-] > NO_2mi$ then $FdnNO_2 = ([NO_2^-]–NO_2min)/([NO_2^-]–NO_2mi+1)$. As such the two denitrification stages are written as:

$$\text{Denitr1} = \text{Denitr1(DON)} + \text{Denitr1}(\text{D}_\text{S}) + \text{Denitr1}(\text{D}_\text{L}) \tag{3.15}$$

$$\text{Denitr2} = \text{Denitr2(DON)} + \text{Denitr2}(\text{D}_\text{S}) + \text{Denitr2}(\text{D}_\text{L}) \tag{3.16}$$

The anammox process is formulated according to Yakushev et al. (2007) as:

$$\text{Anammox} = K_{\text{anammox}} \cdot [NO_2^-] \cdot [NH_4^+] \cdot K_{\text{convert}} \tag{3.17}$$

The K_{anammox} and K_{convert} parameters represent the anammox and conversion constants respectively. The equation also include the oxygen parameter (O_2dn = 25 mmol m^{-3}) for anammox inhibition.

3.1.1 The SAfE nested configuration

A 2–way ROMS–AGRIF nested configuration of the Southern African region from the Southern African Experiment (SAfE) developed and validated by Penven et al. (2006) and Veitch et al. (2009) is used in this study. The SAfE "parent" domain consists of a 1/4° coarse grid covering the Indian and Atlantic Ocean regions around South Africa. The parent domain extends from 2.5°W to 54.75°E and from 4.8°S to 46.75°S (Figure 3.1). Within the coarse parent grid, a 1/12° high resolution child domain is included. The high resolution child grid extends from 3.9°E to 19.8°E and from 12.1°S to 35.6°S covering

the northern and southern Benguela upwelling system (Figure 3.1). The Benguela high resolution "child grid" was built on a Mercator grid with a horizontal resolution of 1/12° (∼ 9 km). The 32 sigma levels in the model were stretched out to increase near surface resolution. Model bathymetry was derived from the 1′ gridded General Bathymetric Chart of the Oceans dataset (GEBCO: www.gebco.net). Initial and open boundary conditions of the configuration were obtained from the 10th year of the SAfE high resolution output (Veitch et al., 2009). At the surface the model was forced with a 1/2° resolution QuickSCAT monthly (from 2000 to 2007) climatological wind stress data (Liu et al., 1998). The COADS–derived monthly 1/2° resolution climatological data was used for surface heat and freshwater fluxes (Da Silva et al., 1994). Additionally, an air–sea parameterization term was added to the surface heat flux using the 9 km SST pathfinder climatology to avoid model SST drift (Casey and Cornillon, 1999). Biogeochemical (nitrate and oxygen) initial and open boundary conditions were provided by monthly climatology of the CSIRO Atlas of Regional Seas (CARS, 2009). The simulation was ran for 16 years. A stable five year output (from year 12–16) is used in this study.

3.1.2 Model diagnostics

Additionally, a 13 years diagnostics run of the high resolution domain (at a 1/11° resolution) was performed to obtain fluxes which were not included with the initial run. The diagnostic run was forced with similar datasets with the exception of model bathymetry. The ETOPO 2 topography provided with ROMSTOOLS was used. Output files from the diagnostics run were saved every 3 days and a stable output (averaged from year 5-13) is used in this study.

3.1.3 Data used

Available datasets were used to evaluate the model and to determine biases from the simulation. For nitrate, annual mean fields from the CSIRO Atlas of Regional Seas (CARS) 2009 climatology were used. The CARS 2009 climatology fields are covered on a 1/2° spatial resolution grid. The CARS atlas consists of 2 major datasets interpolated onto 79 depth levels: World Ocean Atlas 1998 and CSIRO archive of Australian hydrography data. Up to 494 stations have been used to construct the CARS climatology in the Benguela region from 10–7°E and 20–30°S. The Scatterometer Climatology of Ocean Winds (SCOW) data (http://cioss.coas.oregonstate.edu/scow/) are derived from high resolution (0.25°) remotely

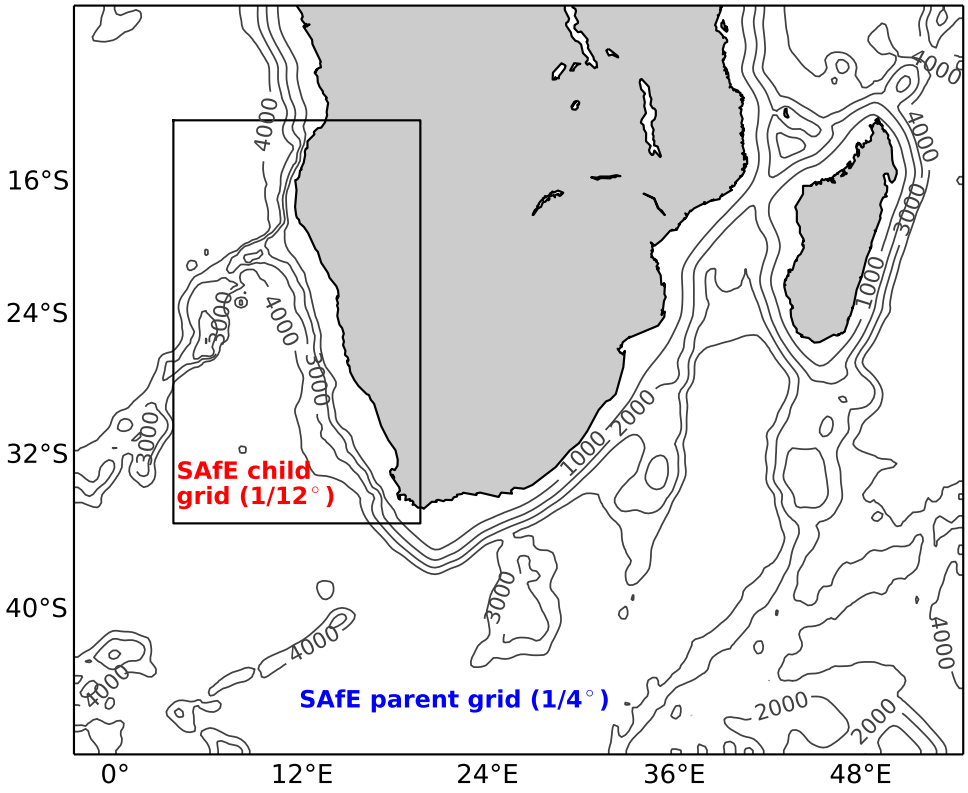

Figure 3.1: Domain of the SAfE configuration showing the parent and child grid. Contours show model bathymetry [m].

sensed wind stress data for the period of September 1999 to October 2009 (Risien and Chelton, 2008).

3.1.4 3D Model comparison with data

Simulated oxygen, nitrate and nitrite fields are compared to the CARS climatology and available in–situ data. With respect to oxygen, the model and CARS climatology fields at depth and minimum oxygen concentrations along the coast are compared. A section of annual mean oxygen concentrations off Walvis Bay from the model and CARS climatology is presented in Figure 3.2a–b. The model is able to capture the OMZ which is located on the shallow continental shelf slope (Figure 3.2a). The OMZ is also more pronounced on the continental shelf and extends offshore (beyond 13°E) at a depth of 60–500 m.

The model overestimates oxygen concentrations (beyond 14°S) between the surface and 60 m as compared to CARS. Gridded objectively analyzed datasets have been reported to overestimate oxygen concentrations in the range of 2–10 mmol O_2 m^{-3} resulting in an underestimation of OMZs extent (Bianchi et al., 2012). To rectify this overestimation, an empirical correction has been suggested for the WOA climatology based on World Ocean Circulation Experiment (WOCE) data (Bianchi et al., 2012). The south Atlantic has not been included in the above–mentioned analysis and the empirical correction has not been applied. In this study, the model is able to capture the very low oxygen concentration (5–10 mmol O_2 m^{-3}) on the shallow continental slope which are also present in the CARS climatology.

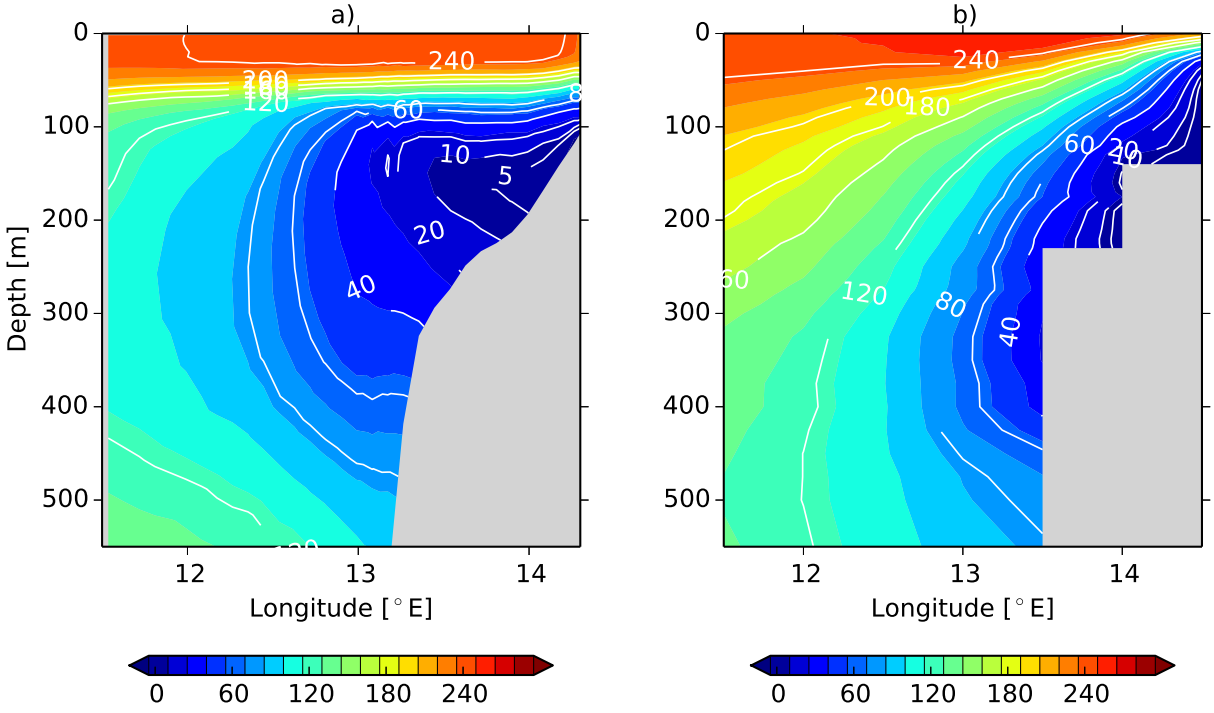

Figure 3.2: Vertical distribution of annual mean oxygen concentrations [mmol O_2 m^{-3}] off Walvis Bay for (a) BioEBUS and (b) CARS.

Pronounced minimum oxygen concentrations are observed in the model as compared to the CARS climatology (Figure 3.3a–b). The OMZ in both model and CARS climatology data does not extend beyond 27°S poleward. In a previous simulation, the OMZ has been found to extend to 26°S poleward (Gutknecht et al., 2013). The simulated OMZ is more

pronounced between 18–26°S on the continental shelf along the Namibian coast. The model has been reported to overestimate oxygen concentrations on the continental shelf due to oxygen–depleting processes not included in the model (Gutknecht et al., 2013). This was attributed to sulphate reduction processes under oxygen–depleted conditions not included. These events have been observed to occur in continental shelf sediments off Namibia leading to hydrogen sulphide production and emission (Lavik et al., 2009; Weeks et al., 2002). Despite oxygen overestimation in shallow coastal waters, the spatial distribution of the OMZ is fairly well–represented.

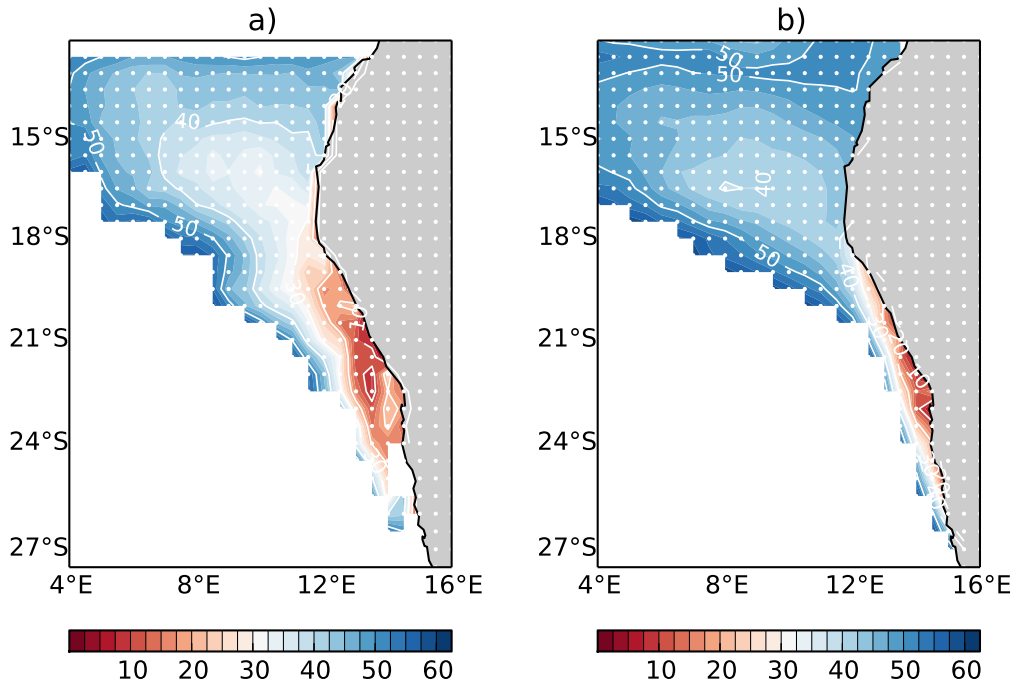

Figure 3.3: Minimum oxygen concentrations [mmol O_2 m^{-3}] from (a) BioEBUS and (b) CARS. The white markers represent the latitude and longitude position of the CARS climatology. White contours indicate oxygen concentrations.

Annual mean nitrate distribution from BioEBUS is compared with the CARS climatology data (Figure 3.4). Nitrate concentrations in both simulated and CARS data are depleted in surface waters (< 50 m) due to phytoplankton assimilation. At 50–120 m, low nitrate concentrations are observed in the region between 14 and 14.5°E from the CARS climatology. Nitrate concentrations between the surface and 100 m between 13–14°E were well simulated. Nitrate concentrations from both simulated and CARS climatology peak to 30 mmol N m^{-3}

below 400 m. These maximum nitrate (25–30 μM) concentrations have been observed in mid waters of the Namibian shelf by Chapman and Shannon (1985) and Kuypers et al. (2005). Overall, the model was able to capture the spatial variability of nitrate off Walvis Bay. A previous study revealed spatial variability in the distribution of inorganic nitrogen in the Benguela attributed to the diverse nature of the system (Chapman and Shannon, 1985).

Table 3.1: Estimated nitrite concentrations [mmol N $^{-3}$] from BioEBUS and the MSM 19/1b cruise. BioEBUS simulated concentrations are averaged at 22–24°S between 11.5–14.5°E. Additional, estimated nitrite concentrations are obtained from published literature.

Reference	Estimation	Region	Date
BioEBUS	0.0056-0.3340	22-24.0°S	
MSM–19/1b	0.0082-0.2759	23.0°S	October 2011
Füssel et al. (2012)	0-4.00	19.1-22.5°S	May/June 2008
Kuypers et al. (2005)	0-2.00	23.0°S	March/April 2003
Dittmar and Birkicht (2001)	0-0.40	19.5°S	July 1999

Annual mean nitrite concentrations within the range of observations were simulated by the BioEBUS model. These concentrations range from 0.0056–0.3340 mmol N m^{-3} off Walvis Bay on the Namibian shelf. The simulated nitrite concentrations exhibit a subsurface maxima similar to those observed during the MSM 19/1b cruise (Figure 4.1). Gutknecht et al. (2013) also observed similar subsurface nitrite maxima around the 50 m depth in a previous simulation. As compared to limited available data and previous studies in the Benguela, simulated nitrite concentrations are also well within range (Table 3.1). The distribution of nitrite in the Benguela in comparison to other studies is explained in detail in section 4.3. Any reported biases do not present a major setback as this chapter aims to understand the physical and biological processes that drive intermediary nitrogen processes on the continental shelf rather than quantifying them.

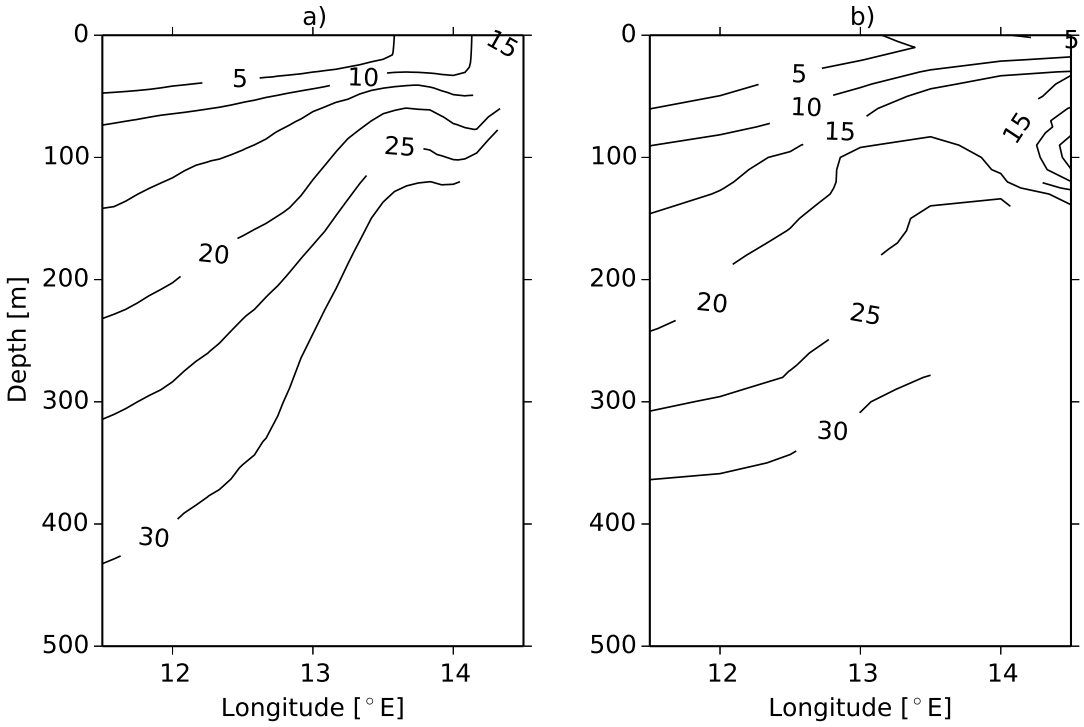

Figure 3.4: Vertical distribution of annual mean nitrate concentrations [mmol N m^{-3}] off Walvis Bay for (a) BioEBUS and (b) CARS.

3.2 1D coupled physical–biogeochemical model

The 1D version of the general circulation model of the ocean (NEMO, Nucleus for the European Modeling of the Ocean, http://nemo-ocean.eu) allows for independent simulation of a water column at a selected position in a grid. The 1D model is a powerful tool that can be used to study physical and numerical vertical mixing processes, to investigate unresolved turbulence processes, to compare vertical mixing schemes and perform sensitivity studies with low computational costs (Madec, 2012). The 1D configuration is based on the zoom functionality over a 3×3 domain centered around the selected position. The horizontal derivatives in the 1D model are set to zero and the velocity components (u and v) are moved on a T–point. Horizontal derivatives depend on the time step and forcings, making them entirely Ekman and inertial. The vertical velocity (w) linked to Ekman pumping is introduced into the model as a constant in this study. The equations of motion are balanced by momentum acceleration, vertical diffusion and the Coriolis force. The equations of motion in NEMO are based on the 3D primitive equations resulting from Reynolds averaging of the Navier–Stokes equations. The equations also include transport equations for temperature and salinity. After simplification of horizontal gradients, the equations in the 1D model as described in Reffray et al. (2015) are reduced to:

$$\frac{\partial u_i}{\partial t} = -\frac{\partial}{\partial z} \upsilon_t \frac{\partial u_i}{\partial z} + f_i \tag{3.18}$$

$$\frac{\partial T}{\partial t} = \frac{1}{\rho_0 C_p} \frac{\partial I(F_{sol}, z)}{\partial z} - \frac{\partial}{\partial z} K_t \frac{\partial T}{\partial z} \tag{3.19}$$

$$\frac{\partial S}{\partial t} = -\frac{\partial}{\partial z} K_t \frac{\partial S}{\partial z} + E_f - P_f \tag{3.20}$$

Where u_i, T and S represent the horizontal components of the velocity, temperature and salinity respectively. The temporal dimension is denoted by t, z is the vertical coordinate, f_i the Coriolis term and P is pressure. The downward irradiance is represented by I, F_{sol} is the penetrative part of the surface heat flux, the reference density is denoted by ρ_0 and

C_p is the specific heat capacity. Evaporation and precipitation fluxes are represented by E_f and P respectively. υ_t and K_t are the vertical turbulent viscosity and diffusivity.

The NEMO 1D model is based on the generic length scale (GLS) turbulent closure scheme. The GLS scheme is based on two prognostic equations for turbulent kinetic energy (k) and the generic length scale (Ψ). The turbulent kinetic energy is computed based on a transport equation as:

$$\frac{\partial k}{\partial t} = D_k + P + G - \varepsilon \tag{3.21}$$

Where the viscous and turbulent transport term is represented by D_k which is expressed as:

$$D_k = \frac{\partial}{\partial z}\frac{\upsilon_t}{\sigma_k}\frac{\partial k}{\partial z} \tag{3.22}$$

The term σ_k in the equation is a constant Schmidt–number. P relates to the production of turbulent kinetic energy by shear:

$$P = \upsilon_t M^2 \tag{3.23}$$

The term G relates to the production of turbulent kinetic energy by buoyancy:

$$G = K_t N^2 \tag{3.24}$$

Only in unstable conditions is G a term for production of turbulent kinetic energy. This term reflects the destruction of the turbulence due to stratification under stable conditions. The ε in the turbulent kinetic energy equation is the rate of dissipation:

$$\varepsilon = \left(C_\mu^0\right)^3 \frac{k^{3/2}}{l}$$

(3.25)

Where C_μ^0 is the model constant (Table 3.2). l is the mixing length. The $k-\varepsilon$ model is implemented in this study. The turbulent quantity ε can be expressed using a generic length scale as:

$$\Psi = \left(C_\mu^0\right)^p k^m l^n \tag{3.26}$$

Where p, m, and n are predefined parameters (Table 3.2) and the transport equation for Ψ is formulated as:

$$\frac{\partial \psi}{\partial t} = D_\psi + \frac{\psi}{k}(C_{\psi 1}P + C_{\psi 3}G - C_{\psi 2^\varepsilon}) \tag{3.27}$$

With $C_{\Psi 1}$, $C_{\Psi 2}$ and $C_{\Psi 3}$ as defined constants for the $k-\varepsilon$ model. The turbulent and viscous terms of Ψ are represented by D_Ψ and formulated as:

$$D_\psi = \frac{\partial}{\partial z}\frac{\upsilon_t}{\sigma_\psi}\frac{\partial \Psi}{\partial z} \tag{3.28}$$

The σ_Ψ is a constant number for the $k-\varepsilon$ model.

The GLS turbulence closure in the 1D model has been tested in the PAPA station located west of Canada in the Pacific Ocean (50°N, 145°W) (Reffray et al., 2015). The GLS closures show some dependence on numerical conditions (time step and vertical discretization). The dependence is minimal in the $k-\varepsilon$ as compared to the $k-kl$ and $k-\omega$ closures (Reffray et al., 2015). GLS closures have also been found to give satisfactory results despite excessive summer stratification, with the $k-\varepsilon$ showing less sensitivity than the $k-\omega$ and $k-l$ closures. The $k-\varepsilon$ closure correctly reproduces mixing and salinity in the halocline than other models. The study concluded that the $k-\varepsilon$ model is good in conserving the halocline

Table 3.2: Predefined turbulence models and parameters for the GLS scheme.

Parameters	$k-kl$	$k-\varepsilon$	$k-\omega$	Generic
(p,n,m)	$(0,1,1)$	$(3,1.5,-1)$	$(-1,0.5,-1)$	$(0,1,-0.67)$
$\left(C_\mu^0\right)^3$	$\left(0.5268\right)^3$	$(0.5268)^3$	$(0.5268)^3$	$(0.5268)^3$
$C_{\Psi 1}$	0.9	1.44	0.555	1
$C_{\Psi 2}$	$0.5\,F_{\text{wall}}$	1.92	0.833	1.22
$C_{\Psi 3}$(stable)	2.62	-0.629	-0.64	0.05
$C_{\Psi 3}$(unstable)	1	1	1	1
σ_k	1.96	1	2	0.8
σ_Ψ	1.96	1.2	2	1.07

with weaker salinity biases. As such, the $k-\varepsilon$ is set as the standard turbulent model for NEMO 1D and considered in this study for coupling with a biogeochemical model.

The biogeochemical model of the pelagic system (BFM, Biogeochemical Flux Model, http://bfm-community.eu) is coupled with the NEMO 1D model. The BFM model has been derived from the European Regional Seas Ecosystems Model (ERSEM) and designed to solve biogeochemical cycles (carbon, oxygen, nitrogen (nitrate and ammonium), phosphorus and silica) in the lower trophic levels of the marine environment (Vichi et al., 2015). The carbonate system and iron cycle in BFM can also be included through user–controlled flags. The BFM model consists of differential equations that are independent of vertical or horizontal processes. The equations in BFM are written following a rate of change and explicit function formulation. Environmental parameters that affect biological rates in BFM are provided by a physical model, NEMO 1D in this case. The dependencies of the pelagic plankton model from the physical environment are described. Coupling between the two models is achieved through surface irradiance and temperature (Vichi et al., 2015). The temperature provided by the physical model regulates physiological processes in the BFM model. The temperature effect (f^T) is parametized in a non–dimensional form as:

$$f^T = Q_{10}^{\frac{T-10}{10}} \tag{3.29}$$

Where the Q_{10} coefficient differs with the functional process considered. Solar radiation at the sea surface as provided by the physical model acts as the energy source for photosynthesis. The PAR is the only portion of the irradiance used for growth and it is computed as a function of the attenuation coefficient of sea water and determined by concentrations of suspended and dissolved particles (Vichi et al., 2015). The PAR attenuation due to chlorophyll in BFM is included through user–controlled flags as a broadband mean and a 3–band attenuation coefficients. The latter attenuation coefficient as proposed by Sakshaug et al. (1997) is considered in this study. The 3–band coefficient is computed in BFM as a differential attenuation of light divided into red, green and blue (RGB) coefficients. These coefficients are functions of the chlorophyll concentrations with the visible portion divided into 3 equal bands and formulated as:

$$E_{PAR}(z) = \frac{\varepsilon_{PAR}}{3} Q_S \left(e^{\int_z^0 \lambda_R(Chl,z')dz'} + e^{\int_z^0 \lambda_G(Chl,z')dz'} + e^{\int_z^0 \lambda_B(Chl,z')dz'} \right) \tag{3.30}$$

The λ coefficients in the model depend on the local total chlorophyll concentration of phytoplankton (P):

$$Chl = \sum_{j=1}^{4} P_l^{(j)} \tag{3.31}$$

Short–wave irradiance flux (Q_S) at the surface is obtained from the physical model as mentioned earlier. Instantaneous irradiance from forcings explained in section 3.2.1 is considered for the light averaging period. The discretized irradiance (E_{PAR}^k) in BFM is located at the top of each layer (k) with three different options available for the light location flag. For this study, light integration over the level depth according to Vichi et al. (2007) is preferred:

$$E_{PAR} = \frac{E_{PAR}^k}{\lambda^k \Delta z^k} \left(1 - \exp\left(- \lambda^k \Delta z^k \right) \right) \tag{3.32}$$

Phytoplankton as primary producers in BFM are divided into four groups according to their equivalent spherical diameter (ESD), namely diatoms (20–200 μ), nanoflagellates (2–20 μ), picophytoplankton (0.2–2 μ) and large phytoplankton (>100 μ) (Vichi et al., 2015). The phytoplankton groups are formulated according to the same primitive equations but differentiated by values of the physiological parameters. Photosynthesis in BFM is controlled through a non–dimensional light regulation factor by Jassby and Platt (1976). Since instantaneous light is used, the equation for the light regulation factor is formulated as:

$$f_P^E = 1 - \exp\left(- \frac{\alpha_{chl}^0 E_{PAR} P_l}{r_P^0 P_c} \right) \tag{3.33}$$

Where α_{chl}^0 is the maximum light utilization coefficient and r_{0_P} is the the maximum specific photosynthetic rate. The final gross primary production (gpp) depends on the daylight availability option. For instantaneous irradiance it is formulated as:

$$\left.\frac{dP_c}{dt}\right|_{O^{(3)}}^{gpp} = f_P^T f_P^E f_P^{PP} r_P^0 P_C \tag{3.34}$$

The BFM model allows multiple nutrient limitations for phytoplankton growth and photosynthesis. Nutrient limiting factors can be internal or external based on an internal nutrient quota or dissolved inorganic concentrations respectively. Regulating factors for internal nutrient limitation are implemented for nitrogen, phosphate, iron and silicate. The factors are controlled by optimal and minimum values for the existence of structural components in the cell (Vichi et al., 2015). Luxury uptake is not possible for silicate since it is not stored in the cell but formulated as a direct proportion of the net carbon growth. As such, external limitation for silicate is preferred for diatoms. The threshold combination approach for co–limitation in all other nutrients is selected:

$$f_P^{nut} = min(f_P^{n,p}, f_P^f, f_P^S) \tag{3.35}$$

The BFM approach to nutrient uptake is mostly derived from Baretta-Bekker et al. (1997)

and formulated according to the Monod and Droop equations with a threshold control. The Droop and Monod equations are based on the intracellular quota and external concentrations approach respectively. Nitrite is introduced in BFM as in BioEBUS to complete the nitrogen cycle. Therefore, the dissolved inorganic nitrogen (DIN) uptake in BFM becomes the sum uptake of nitrite, nitrate and ammonium which is the minimum between a diffusion–dependent rate, and a balanced growth and luxury uptake based rate:

$$\sum_{j=2,3,4} \left.\frac{dP_n}{dt}\right|_{N^{(j)}}^{upt} = \min\left(\left(a_P^n \frac{h_P^n}{h_P^n + N^{(4)}}(N^{(2)}+N^{(3)}) + a_P^n N^{(4)}\right)P_c, n_P^{opt} G_P + v_P\left(n_P^{\max} - \frac{P_n}{P_c}\right)P_c\right) \tag{3.36}$$

Where h_P is the half saturation constant for ammonium uptake preference. Nitrite and nitrate are combined during uptake. Ammonium preference is parametized through a saturation function that modulates the affinity constant (a_P^n) for dissolved nitrate. Optimal and maximum nitrogen uptake is denoted by (n_P) and balanced uptake is a function of the net primary production (Gp). The relaxation rate towards the optimal light intensity is represented by v_P.

Modeling phosphate uptake in BFM is simpler than other nutrients as a single species (orthophosphate) is considered (Vichi et al., 2015). The phosphate uptake equation in BFM is formulated as:

$$\left.\frac{dP_p}{dt}\right|_{N^{(1)}}^{upt} = \min\left(a_p^{(1)} N^{(1)} P_c, p_p^{opt} G_p + v_p\left(p_p^{\max} - \frac{P_p}{P_c}\right)P_c\right) \tag{3.37}$$

Phytoplankton intracellular minimum, optimal and maximum phosphate quota in the equation are represented by P_p^{min}, P_p^{opt} and P_p^{max} respectively. In BFM, silicate is not stored in the cell and it is formulated as a direct proportion to the net carbon growth:

$$\left.\frac{dP_s}{dt}\right|_{N^s}^{upt} = s_P^{opt} G_p \tag{3.38}$$

Dissolution of silicate frustules in BFM is formulated as:

$$\left.\frac{dR_s^{(6)}}{dt}\right|_{N^{(5)}}^{rmn} = \Lambda_s^{rmn} f_{R^{(6)}}^{T} R_s^{(6)} \tag{3.39}$$

Where Λ_s^{rmn} represents the constant specific dissolution rate and ${}^{T}_{R^{(6)}}$ is the temperature regulating factor responsible for enhancing bacterial activity at higher temperatures.
Dissolved oxygen and carbon dioxide are important for completion of global biogeochemical cycles. Gaseous exchange at the air–sea interface is not described in BFM as it is assumed to be a physical process (Vichi et al., 2015). Denitrification and sulfur cycling depend on the oxygen dynamics in oceanic regions where bacteria are the major drivers of these processes. In BFM, all reduced chemical species as a result of bacterial anoxic respiration are computed as one state variable, "reduction equivalents". This variable is assumed to be chemically equivalent to the sulphide ion (HS^-) and partly used for the parameterization of denitrification and sulphide production.

Net oxygen production in the pelagic system is derived from the sum of gross primary production and respiration rates from phytoplankton, zooplankton and bacterial communities minus losses due to chemical reactions and formulated as:

$$\begin{aligned}\left.\frac{dO^{(2)}}{dt}\right|_{bio} = \Omega_c^O \sum_{j=1}^{3} \left(\left.\frac{dP_c^{(j)}}{dt}\right|_{O^{(3)}}^{gpp} - \left.\frac{dP_c^{(j)}}{dt}\right|_{O^{(3)}}^{rsp} \right) + \\ -\Omega_c^O f_B^O \left.\frac{dB_c}{dt}\right|_{O^{(3)}}^{rsp} + \\ -\Omega_c^O \sum_{j=4}^{6} \left.\frac{dZ_c^{(j)}}{dt}\right|_{O^{(3)}}^{rsp} + \\ -\Omega_n^O \left.\frac{dN^{(4)}}{dt}\right|_{N^{(3)}}^{nit} - \frac{1}{\Omega_o^r} \left.\frac{dN^{(6)}}{dt}\right|_{sink_r}^{reox}\end{aligned} \tag{3.40}$$

Constant stoichiometric coefficients (Ω^O) are used to convert the rates to oxygen units. Bacterial oxygen demand is partitioned into consumption and reduction equivalent

production demand by a regulating factor (f_B^O).

Nitrification in BFM is parametized with a dependence on ammonium and oxygen concentrations as:

$$\left.\frac{dN^{(4)}}{dt}\right|_{N^{(3)}}^{nit} = \Lambda_{N^{(4)}}^{nit} f_n^T \frac{O^{(2)}}{O^{(2)} + h_o} N^{(4)} \tag{3.41}$$

Where the constant specific nitrification rate is $\Lambda_{N^{(4)}}^{nit}$ and f_n^T is the temperature regulating factor. To obtain similar results from both models the equation is modified and implemented in two stages to include nitrite, as in BioEBUS, with no temperature dependence according to Yakushev et al. (2007):

$$\left.\frac{dN^{(4)}}{dt}\right|_{N^{(2)}}^{nit} = \Lambda_{N^{(4)}}^{nit} \frac{O^{(2)}}{O^{(2)} + h_o} N^{(4)} \tag{3.42}$$

$$\left.\frac{dN^{(2)}}{dt}\right|_{N^{(3)}}^{nit} = \Lambda_{N^{(2)}}^{nit} \frac{O^{(2)}}{O^{(2)} + h_o} N^{(2)} \tag{3.43}$$

Nitrous oxide production is introduced in BFM and parametized according to Suntharalingam et al. (2000) as implemented in BioEBUS. Oxygen consumption is used as the input rate for the source on nitrous oxide and the equation is written as:

$$\left.\frac{dO^{(5)}}{dt}\right|_{bio} = (\alpha + \beta f_{O^{(5)}}^o) \left.\frac{dO^{(2)}}{dt}\right|_{bio} \tag{3.44}$$

Where α is a scalar multiplier determined from observations of linear correlations between nitrous oxide and Apparent Oxygen Utilization (AOU). The β in the equation is a constant and enhanced nitrous oxide production under low oxygen conditions is regulated with a non–dimensional regulating factor ($f_{O^{(5)}}$) as implemented in BioEBUS. The β coefficient also accounts for nitrous oxide production under denitrification conditions and regulated with the F_{O_2} factor as indicated earlier.

Reduction equivalents formation is parametized by conversion of the bacterial oxygen demand into sulphide under low oxygen conditions:

$$\left.\frac{dN^{(6)}}{dt}\right|_{bio} = \Omega_o^r \Omega_c^O (1 - f_{B1}) \left.\frac{dB_c}{dt}\right|_{O^{(3)}}^{rsp} + \\ -\Omega_o^r \tilde{\Omega}_n^O \left.\frac{dN^{(3)}}{dt}\right|_{sink_n}^{denit} - \left.\frac{dN^{(6)}}{dt}\right|_{sink_r}^{reox} \tag{3.45}$$

The metabolic formation of reduction equivalents occurs below a threshold level of oxygen (30 mmol O_2 m^{-3}) and $f_B^o < 1$. The sulphate reduction favors denitrification as part of the oxygen demand is redirected towards the process. The redox conditions from the formation of reduction equivalents enhances denitrification as follows:

$$\left.\frac{dN^{(3)}}{dt}\right|^{denit} = \Lambda_{N^{(3)}}^{denit} f_n^T \left[\frac{1}{\mathscr{M}_o^*} \Omega_c^O (1 - f_B^O) \left.\frac{dB_c}{dt}\right|_{O^{(3)}}^{rsp}\right] N^{(3)} \tag{3.46}$$

Where $\Lambda_{N^{(3)}}^{denit}$ represents specific denitrification rate at the reference anoxic mineralization ($\mathscr{M}_o^*$). Production of reduction equivalents is converted to nitrate consumption if nitrate is still present under anoxic conditions leading to production of gaseous nitrogen. some oxygen is not completely depleted where

$$\frac{dN^{(6)}}{dt} = \Lambda_{N^{(6)}}^{reox} \frac{O^{(2)}}{O^{(2)} + h_o} N^{(6)} \tag{3.47}$$

The denitrification and reduction equivalent parameterization described in BFM are key in understanding suboxic and anoxic processes in the Benguela. Nitrogen loss and hydrogen sulphide production occur in the OMZ as previously mentioned. With the equations and formulation discussed here, the 1D model is implemented in the Benguela to understand biogeochemical interactions.

3.2.1 Station selection and initial conditions

The NEMO 1D configuration was built on a 3×3 grid centered around the selected station positions as already stated. The longitude and latitude in the grid are spaced by a distance of 0.1°. The stations selected for model simulations were obtained from locations sampled during the MSM 19/1b cruise (Figure 3.5).

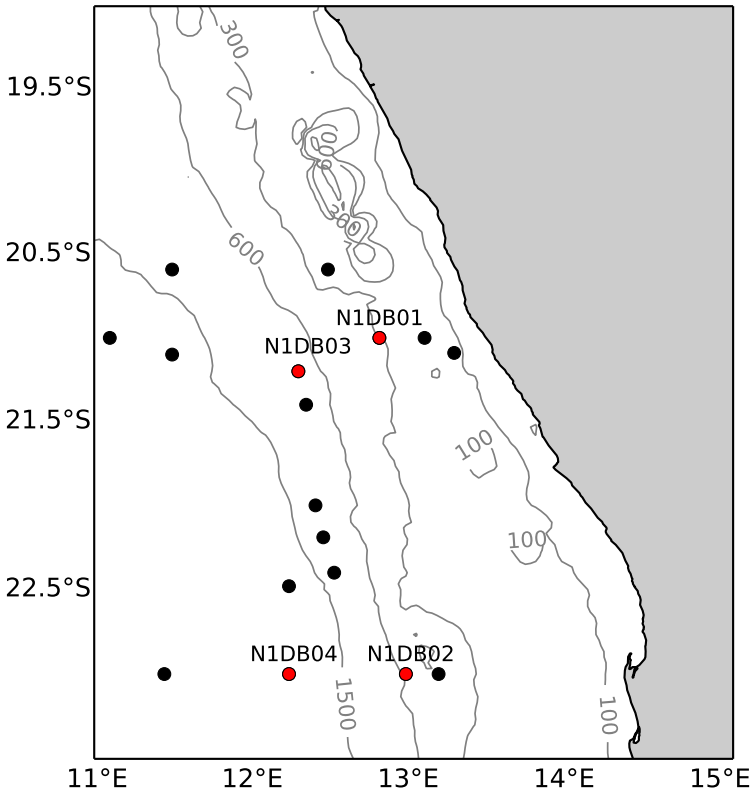

Figure 3.5: Map of the Namibian shelf showing location of the stations sampled during the MSM 19/1b cruise. The stations selected for the 1D model are shown in red. Contours represent water depths [m] derived from the ETOPO 2 dataset.

The domains of the selected stations are presented in Table 3.3. Four stations, one on the shallow shelf (N1DB01), two on the mid–shelf (N1DB02 and N1DB03) and one offshore (N1DB04) were selected to test model capability in representative shallow, mid– and deep water columns. The domains consist of different vertical levels selected after interpolation of input files onto the NEMO 1D mesh grid. Vertical resolution in the model varies, with

minimal spacing (1.0–11.0 m) in the surface (100 m) and increased spacing (11–26 m) in bottom waters. Bathymetry values of the domains are the bottom depths of the geographic points from the ETOPO dataset after interpolation.

Table 3.3: Domains of the stations selected for the coupled NEMO–BFM 1D simulations.

ID	Latitude [°S]	Longitude [°E]	Vertical levels	Bottom depth [m]	Date
N1DB01	21.00	12.83	34	271.35	2011.10.05
N1DB02	23.00	13.00	40	508.64	2011.10.09
N1DB03	21.20	12.31	40	508.64	2011.10.07
N1DB04	23.00	12.25	53	1795.67	2011.10.08

The 6 hourly atmospheric forcing were extracted from the NCEP/NCAR reanalysis 1 data (http://www.esrl.noaa.gov/psd/data/gridded/data.ncep.reanalysis.surfaceflux.html). The NCEP/NCAR reanalysis dataset is a joint product from the National Centers for Environmental Prediction (NCEP) and the National Center for Atmospheric Research (NCAR). The dataset consists of historical and constantly updated data (from 1948–present) that represents the current atmospheric state on a global grid. The atmospheric forcing includes: air temperature (K), humidity (kg kg^{-1}), precipitation (kg m^2 s^{-1}), zonal and meridional wind (m s^{-1}) and long and shortwave radiation (W m^2). Radiation fluxes and the precipitation rate used are referenced at the surface. Air temperature and humidity were obtained at 2 m and wind stress at 10 m. Climatology of the forcings were extracted from the dates of the selected cruise stations that were sampled.

Options for surface and bottom boundary conditions are available for BFM through coupling with NEMO. The CORE bulk formulation for surface boundary conditions is used in this study with external forcing for wind stress and heat fluxes as explained in the previous paragraph. Sea surface temperature and salinity in the model is restored to observed climatology from the CARS database. Geothermal heating at the bottom of the ocean is not applied to active tracers and the geothermal flux is set to zero. Therefore it is assumed that there is no exchange of heat or salt through the ocean bottom. River runoffs and surface freshwater fluxes are not activated and the mean sea

level state is allowed to drift freely. River input and other additional boundary fluxes such as dilution and atmospheric deposition are turned off in NEMO as they are not taken into account by the standard BFM model. The simulated water column extends from the surface to the bottom according to the vertical levels. The pelagic variables in BFM have the spatial dimensions of the number of vertical levels. Currently a benthic model is not included with the standard BFM model. In the case where a benthic model is available in BFM, direct mass exchange is not allowed between pelagic and benthic variables.

Temperature and salinity from the CARS 2009 climatology are used in the simulations due to the restoration required in the model (Section 3.2.2). The coupled biogeochemical model is initialized with nutrient data from CARS and World Ocean Atlas (WOA). Dissolved inorganic carbon (DIC) and total alkalinity data is obtained from the WOA climatology. Initial values for nitrite are obtained from the MSM 19/1b data. Iron initial value is set to 0.05 μmol Fe m^{-3}. Nitrous oxide initial concentrations are computed as a function of oxygen using the parameterization of Suntharalingam et al. (2000) as described in equation 3.44. Initial concentrations for other state variables are set to a default of 0.01 mg C m^{-3} (Table 6.1). The stations selected in this study are simulated for 2 years from the sampling dates (Table 3.3) with the second year considered as a spin–off. The model reaches stability after 50 days of simulation and results from the second year are used in validation and analysis of results.

3.2.2 Sampling and biogeochemical analysis

Sampling was performed along transects on the Namibian shelf during the second leg of the Maria S. Merian in October 2011. The cruise covered 29 stations, nutrient measurements were collected for 20 stations and 17 were measured for nitrite. Water samples were taken at selected CTD depths with a Rosette sampler. Nitrite concentrations at the stations were measured using the method of Strickland and Parsons (1972). A sulfinilamide solution was added to the blanks, nitrite and nitrate standards and samples. The solutions were then mixed and allowed to react for 2–8 minutes. A N-(1-naphthyl)-ethylenediamine dihydrochloride (NEDI) solution was added after the reaction time. Absorbances of the solutions were read on the spectrophotometer at a wavelength of 543 nm. Nitrite concentrations were calculated from the corrected sample and standard absorbances.

The oxygen sensor was calibrated by manual Winkler titration of water samples collected

Table 3.4: List of stations sampled for nitrite during the MSM 19/1b cruise

Station no.	ID	Date	Latitude [°S]	Longitude [°E]	Bottom depth [m]
4	1028	10.04.11	21.09	13.31	30.90
5	1029	10.05.11	21.00	13.12	111.35
6	1030	10.05.11	21.00	12.83	291.38
7	1031	10.05.11	20.59	12.50	504.50
8	1032	10.05.11	20.59	11.50	1012.24
9	1033	10.06.11	21.00	11.10	1014.90
10	1034	10.06.11	21.10	11.50	1002.00
11	1035	10.07.11	21.20	12.31	505.80
12	1036	10.07.11	21.40	12.36	550.54
13	1037	10.07.11	22.00	12.42	439.76
14	1038	10.07.11	22.19	12.47	418.02
15	1039	10.07.11	22.40	12.54	353.71
16	1040	10.08.11	22.48	12.25	1895.40
17	1041	10.08.11	23.00	11.45	2592.81
18	1042	10.08.11	23.00	12.25	1832.24
19	1043	10.09.11	23.00	13.00	490.32
20	1044	10.09.11	23.00	13.21	330.73

at selected depths throughout the water column at each station. Biological oxygen demand (BOD) bottles of known volumes were filled with water samples from the Rosette sampler for oxygen determination using the method of Strickland and Parsons (1972). The dissolved oxygen in the bottles was fixed by addition of manganous chloride and alkaline iodide. The bottles were then shaken vigorously to ensure thorough mixing. The precipitates were allowed to settle for not more than 12 hours in the dark and at room temperature. The precipitates were then dissolved by the addition of sulfuric acid and vigorous shaking. The samples were then titrated against sodium thiosulphate and the volumes of the titre were recorded. The contents of the BOD bottles were titrated in a 25–ml graduated measuring cylinder. A small magnetic stirring bar was placed into the bottle with the microburette positioned in the middle. A starch solution was used to detect the end point. Dissolved oxygen concentrations were determined from the volume of the titre, standardization factor and the volume of the BOD bottles.

Phosphate concentrations during the MSM 19/1b cruise were determined using the colorimetric method of Murphy and Riley (1962). Seawater samples from the Rossette sampler were acclimatised to room temperature (15–30°C). Then the samples were reacted with a composite reagent containing ammonium molybdate, sulfuric acid, ascorbic acid and potassium antimonyl–tartrate. Absorbances of the resulting phosphor–MB complex from the samples were read on the spectrophotometer at 885 nm. After correction of the standard and sample absorbances, concentrations of phosphate in the samples were calculated.

Silicate concentrations at the stations were determined using the method of Strickland and Parsons (1972). A mixed reagent consisting of sulfuric acid and acid molybdate was first prepared. The mixed reagent was then added to the standard solutions and samples and left for 10–15 and 10–20 minutes respectively. Oxalic acid followed immediately by ascorbic acid were added to the sample and standard solutions. The solutions were left for 30–60 minutes and the absorbances were read at 810 nm. Silicate concentrations in the samples were determined from the corrected sample and standard absorbances. The standardization factor (F) for determination of silicate is a function of salinity of the samples. As such, the concentrations were multiplied by 1.15 to rectify the salt error factor.

3.2.3 Temperature and salinity restoration

Results from the initial model run show a drift in temperature and salinity since some stations are located in a coastal region with high variability. Consequently, low temperatures during winter and upwelling months are not well–represented. No distinct seasonal trend in the depth of the thermocline is identified. With no seasonal trend in temperature and no freshwater inputs, the model drifts towards a warmer and saltier state. Similarly, no distinct seasonal trend in the halocline is observed. Atmospheric inputs only drive vertical processeses within the upper water column associated with upwelling source waters in the region. It is important to simulate the correct seasonal trend of these environmental parameters as they drive physiological processes in the BFM model.

A Newtonian damping term is introduced in the model to rectify temperature and salinity seasonality. The damping term is introduced in a simulation to specify boundary conditions in a limited domain (Madec, 2012). In this study, the term was also introduced to account for upwelling introduced through a constant vertical velocity. The damping term is introduced into the salinity and temperature equations as:

$$\frac{\partial T}{\partial t} = \cdots - \gamma(T - T_0)$$

$$\frac{\partial S}{\partial s} = \cdots - \gamma(S - S_0) \tag{3.48}$$

The γ term in the equations is the inverse of the time scale. Temperature and salinity for restoration are provided as climatology derived from CARS 2009 datasets. The restoring coefficient is a 3D array which is read in the model during the tracer damping initialization routine. The netcdf file used to generate the restoration was created from the model mesh grid with the NEMO damping tools provided (Madec, 2012). To allow for a less restricted model run, temperature and salinity damping were set to relaxation timescales of 10 and 15 days in the surface and bottom waters respectively. The transition depth from the upper ocean to the deep ocean is set at 600 m since the 1D configurations include shallow stations. A more reliable and stable seasonal trend in temperature and salinity is achieved with the Newtonian damping term (Figure 3.6).

The temperature and salinity profile at all stations is characterized by warm, saltier surface waters in the upper 200 m. The thermocline and halocline are defined by the 12°C and 35.1 isolines respectively. There is a strong correlation between the thermocline and the halociline at station N1DB01, N1DB03 and N1DB04. This correlation is decoupled at station N1DB02. This station is located on the continental slope off Walvis Bay with high variability. This high variability can be attributed to interchanges between the SACW and the ESACW, upwelling and strong mixing on the slope. However, the temperature profile at station N1DB02 is similar to the other stations. Strong upwelling occurs during late winter and spring; as observed at the station on the shallow coast (N1DB01). The other stations show weak upwelling since they are located at a distance from the coast. The model is able to capture the physical processes in the region with the addition of the restoration term and vertical velocity. The minimized model bias results are presented in the next subsection.

3.2.4 1D Model validation

Temperature and salinity model biases after introduction of the damping term are presented in Figure 3.7. A warm temperature bias is observed in surface waters of all the stations (Figure 3.7 a–d). This warm temperature bias ($\geq$ 1.5°C) creates a salinity bias ($\leq$ 0.068) at 0–50 m (Figure 3.7 e–f). Seasonal temperature and salinity biases are exhibited at 50–400 m during spring and winter. The biases are characterized by underestimation and overestimation of these properties during spring and winter respectively. A distinct latitudinal bias in these properties is observed between the stations.

The surface temperature and salinity bias is from atmospheric forcing. The NCEP reanalysis data has poor resolution and to some extent, representation in this region. Winter and spring temperature and salinity bias is from horizontal processes not reproduced by the model. Interchanges between the warm, saltier SACW and colder, less saline ESACW in the region create these differences. The influence of these waters is stronger at 21°S (N1DB01 and N1DB03). The bias is minimized at station N1DB02 and N1DB04 because of regular intrusion of ESACW and less SACW. Upwelling contributes less to the bias since the vertical velocity has been included.

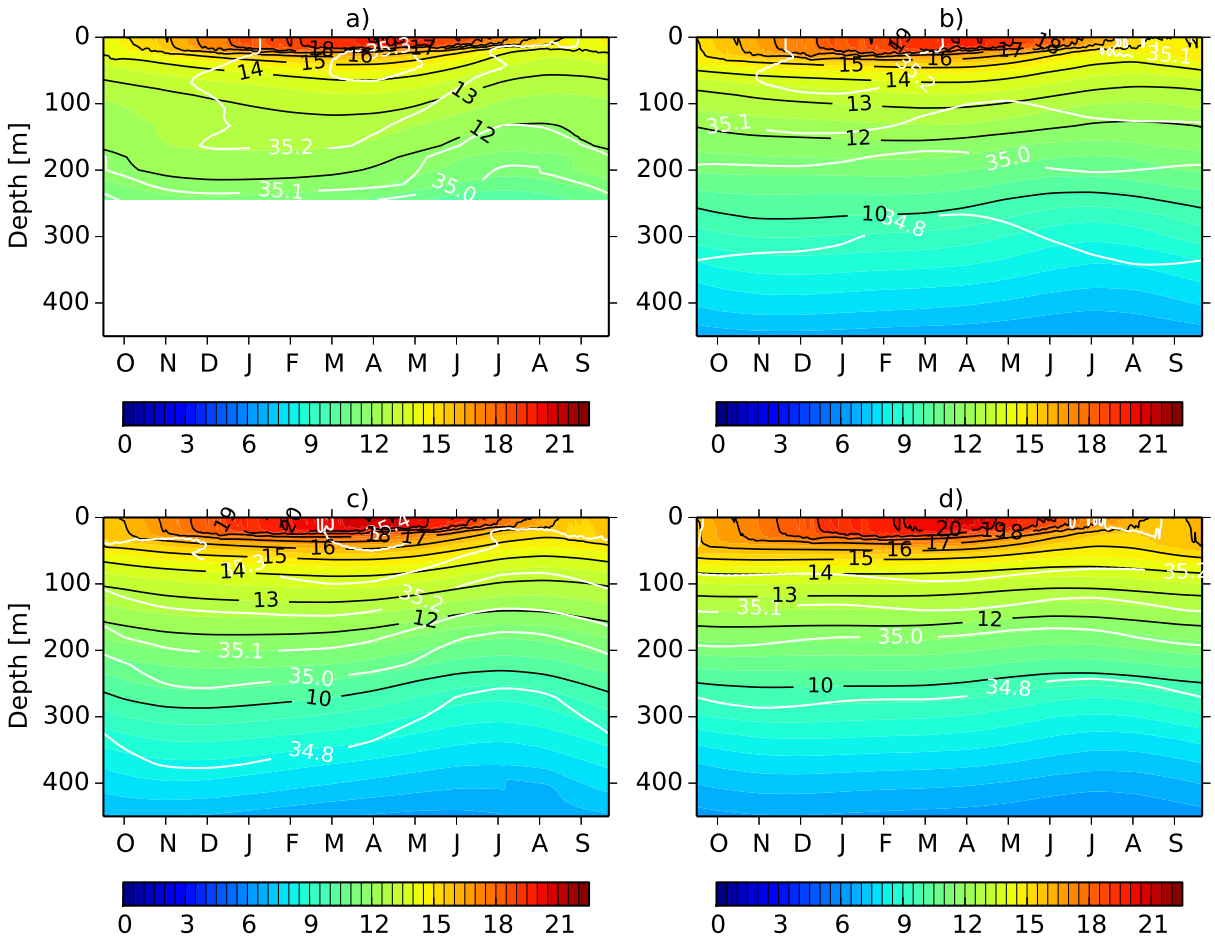

Figure 3.6: Simulated temperature (°C) after introduction of the damping term for station (a) N1DB01, (b) N1DB02, (c) N1DB03 and (d) N1DB04. Black and white contours show temperature and salinity concentrations respectively.

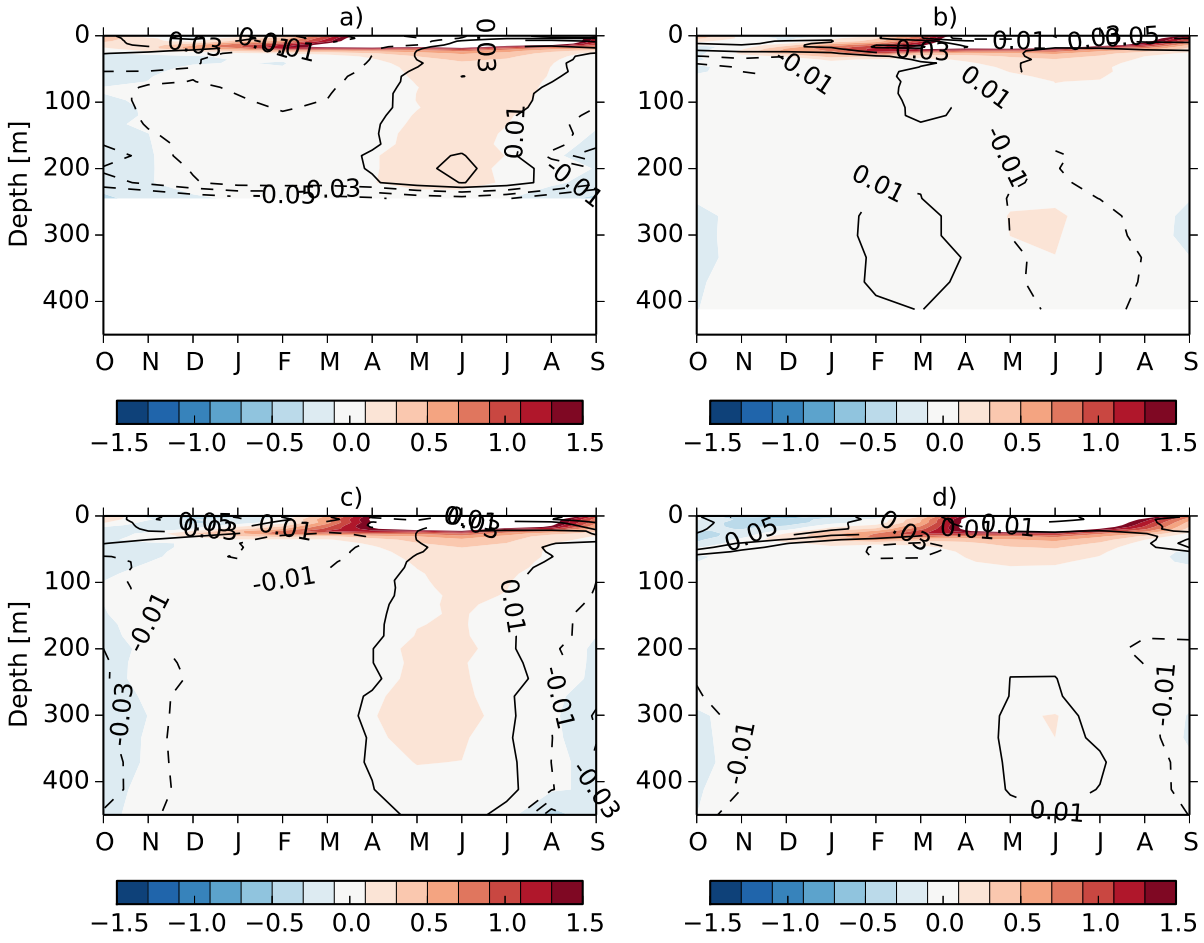

Figure 3.7: Temperature (°C) bias (model−CARS) for station (a) N1DB01, (b) N1DB02, (c) N1DB03 and (d) N1DB04. Contours represent salinity bias.

Simulated nutrient concentrations for the sampled dates are compared to the MSM 19/1b cruise and CARS October data (Figure 3.8). The simulated nutrient profiles are compared to MSM 19/1b cruise data at similar dates to evaluate the strength of the model in reproducing concentrations due to local processes. The simulated profiles are generally in agreement with observed data with slight differences at depth. Oxygen concentrations in both the model and cruise data range between 0–260 mmol O_2 m^{-3} (Figure 3.8a). The model shows a slightly higher oxygen consumption at station N1DB02, N1DB03 and N1DB04. With regard to station N1DB01, oxygen concentrations between 60–130 mmol O_2 m^{-3} are slightly offset between 50–75 m. However, the oxygen concentrations above and below (OMZ) this depth are correctly simulated. Simulated and measured phosphate concentrations at the stations range between 0.5–2.5 mmol P m^{-3}. Higher phosphate concentrations are shown below 50 m due to phosphate release under low oxygen conditions both in the model and MSM 19/1b data (Figure 3.8b). Silicate concentrations at station N1DB01 follow a similar profile to the MSM 19/1b data. Silicate concentrations in the MSM19/1b and model data range between 0–20 mmol Si m^{-3} in the upper 400 m. Higher silicate concentrations in the model are shown below 100 m at station N1DB02 and N1DB03 (Figure 3.8c). These concentrations can be attributed to increased sinking particles in the model. High silicate concentrations are shown at the shallow station (N1DB01) due to increased primary production. Nitrate concentrations from the model mostly compare well with the CARS climatology data at depth (Figure 3.8d). A slight decrease in nitrate concentrations is observed between 100–150 m at station N1DB01. This can be attributed to increased denitrification under low oxygen concentrations. Nitrous oxide concentrations from the model also compare well with concentrations calculated from the MSM19/1b data (Figure 3.8e). Increased nitrous oxide production up to 0.10 mmol N m^{-3} occurs at station N1DB01. Slightly higher nitrous oxide concentrations are shown at station N1DB03 due to the accelerated production under low oxygen concentrations observed at 200–300 m in the MSM 19/1b data. The biogeochemical processes introduced in the model and their implications locally are discussed in detail in Chapter 5 and 6.

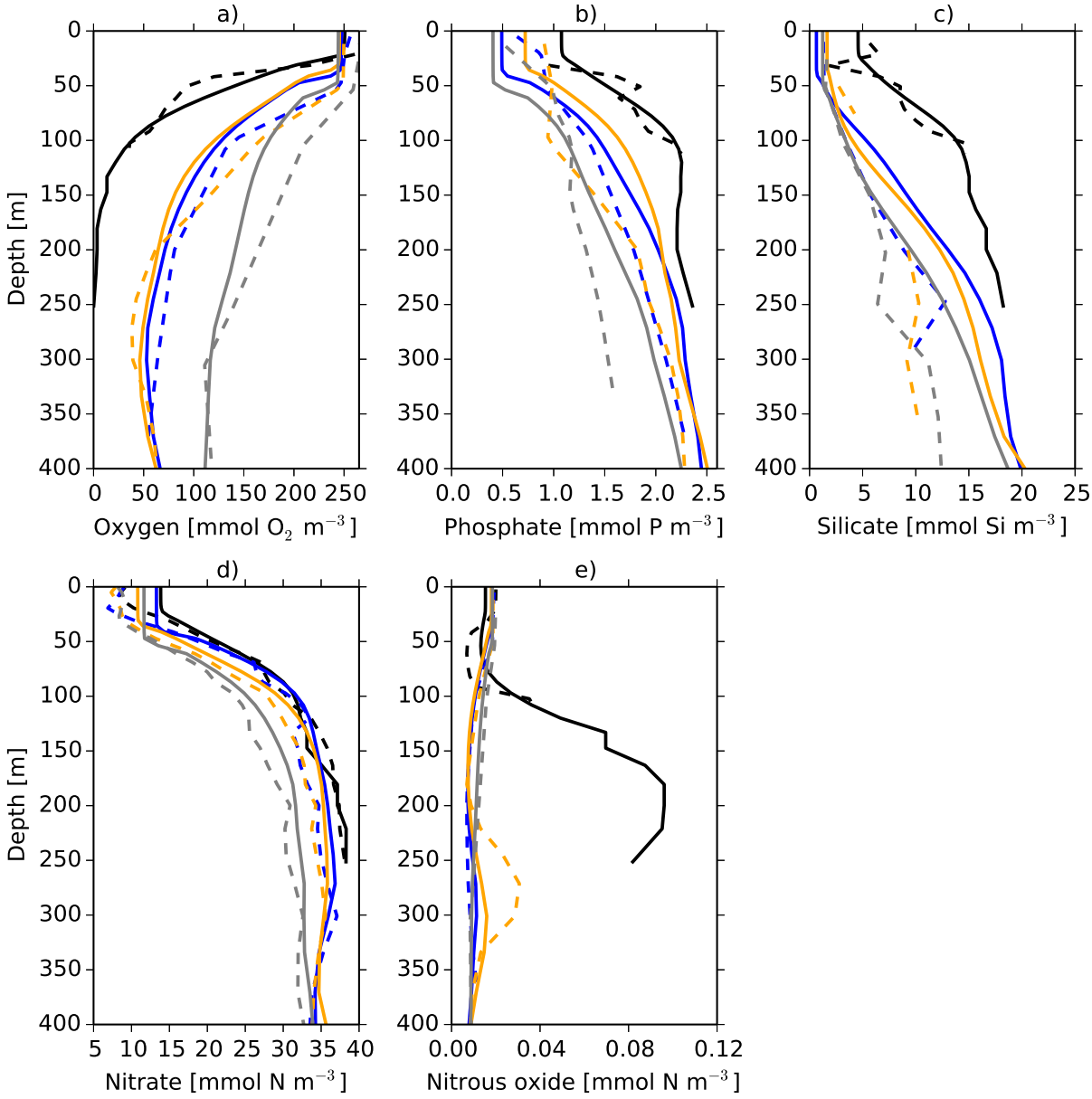

Figure 3.8: Vertical profiles of (a) oxygen, (b) phosphate (c) silicate, (d) nitrate and (e) nitrous oxide for station N1DB01 (black) , N1DB02 (blue), N1DB03 (orange) and N1DB04 (grey) after one year of simulation. Solid and dashed lines represent model and observed data respectively. Oxygen, phosphate, silicate and nitrous oxide (calculated as a function of oxygen) are obtained from the MSM19/1b cruise. Nitrate concentrations are from the CARS climatology for the month of October.

Simulated nutrient concentrations are also compared to the CARS climatology to evaluate the strength of the model in reproducing seasonality and non–local processes. The standard deviation (σ), root mean square error (RMSE) and the correlation coefficient (R) between model and CARS data are presented with Taylor diagrams (Taylor, 2001). For statistical comparisons, CARS and model data are interpolated onto similar station depths. Model performance as compared to CARS is measured by $R \geq 0.9$, $0.6 \leq \sigma^* \leq 1.4$ and RMSE* ≤ 0.4 (* normalized) (Gutknecht et al., 2013). The correlation coefficients for oxygen, nitrate, phosphate and silicate in all the stations are above 0.84, with RSMEs* below 0.7 and standard deviations of 0.60–1.50 (Figure 3.9). The normalized standard deviations for oxygen at all stations are within the reference range, indicating the concentrations are well–simulated.

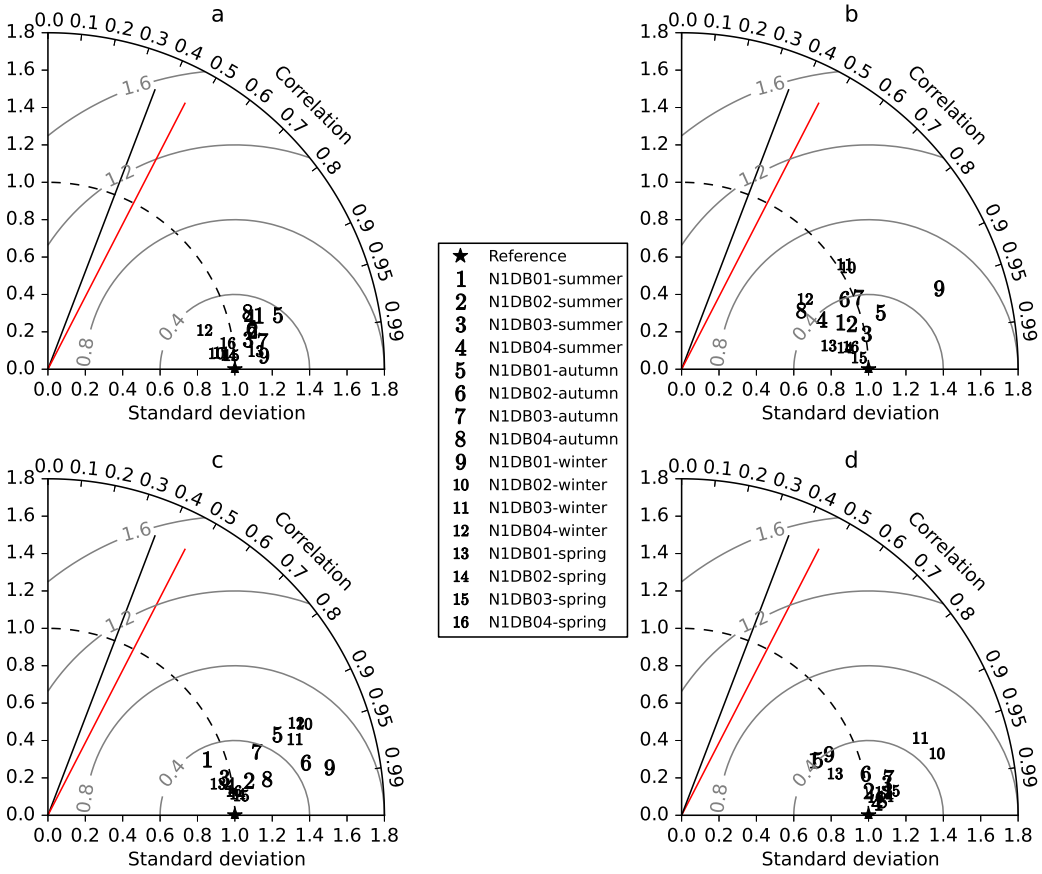

Figure 3.9: Taylor diagrams for (a) oxygen, (b) nitrate, (c) phosphate and (d) silicate. The diagrams show the normalized standard deviation, RMSE and correlation for CARS and model across the stations. The star and dashed contour indicate the reference point and standard deviation respectively. Gray contours measure the distance from reference and the RMSEs. The lines represent the 95th (black) and 99th (red) significance levels.

Winter nitrate concentrations at station N1DB01 are slightly overestimated ($\sigma^* = 1.59$, RMSE* = 0.8 and $R = 0.94$). The nitrate overestimation in this station is due to nitrate depletion below 100 m from non–local processes during winter not captured by the model. Station N1DB02 and N1DB03 nitrate concentrations during winter are well–simulated but characterized by high RMSEs*. Station N1DB04 nitrate underestimation is due to a deeper (below 400 m), offshore nitrate sink from non–local processes during autumn and winter. Seasonal phosphate concentrations at most stations were generally well–simulated. Phosphate concentrations at station N1DB01 during autumn are overestimated around the 200 m depth. Stations N1DB02 show that phosphate is also overestimated at 300–500 m during autumn. These two stations are located inshore suggesting that phosphate concentrations are lower in these locations during autumn. During winter, phosphate concentrations at all stations are overestimated.

Silicate underestimation ($\sigma^* = 0.77$, RMSE* = 0.5 and $R = 0.95$) at station N1DB01 is due to high concentrations observed at bottom depths during winter in the CARS climatology and not captured by the model. At station N1DB02 and N1DB03, silicate bias is due to model overestimation during winter. The reported biases are predominantly from horizontal, non–local processes during winter. As described in the general introduction, the Benguela shelf region is dominated by the well–oxygenated, low–nutrient ESACW which flushes the system during winter. Despite the small biases from non–local processes during winter, the 1D model performed fairly–well since most of the nutrient estimates fall within the reference range.

4 | Intermediary nitrogen species and associated feedback processes in the Benguela

Abstract

Understanding nitrite dynamics in OMZs is a challenge as it represents an intermediary nitrogen species with a short turnover time. Nitrite is also reduced to dinitrogen in OMZs, reducing its accumulation. This creates difficulties in detecting nitrite with colorimetric methods as concentrations may occur below detection limits in some regions. Nitrite concentrations are key to understanding intermediate nitrogen processes and their implication for nitrogen loss in OMZs. A coupled physical–biogeochemical model is applied in the Benguela OMZ to study nitrite dynamics and its associated feedback processes. Simulated results show the occurrence of primary and secondary nitrite maxima in the Benguela shelf waters. The primary nitrite maxima in the Benguela are attributed to nitrification and nitrate assimilation as they occur in association with the nitracline. Secondary nitrite maxima accumulate in the ABF OMZ and are attributed to denitrification. The secondary nitrite maxima are consumed by anammox off Walvis Bay. Nitrite maxima are restricted to the shelf off Walvis Bay and advected offshore in the ABF region. Interchanges between the poleward SACW and the equatorward, well–oxygenated ESACW, drive the seasonality of nitrogen processes in the Benguela. Subsequent nitrite reduction in the Benguela OMZ leads to nitrous oxide production, with high concentrations occurring in the ABF region as a result of nitrification and accelerated production under suboxic conditions. Off Walvis Bay, nitrous oxide production is low since nitrite is consumed by anammox. Nitrous oxide production occurs in thermocline, intermediate and deeper water masses in the ABF region. High N fluxes in the Benguela are attributed to nitrification as compared to anammox and denitrification. Results from this study demonstrate the role of intermediate nitrogen species in nitrogen feedback processes in the Benguela and can be applied in other regions.

4.1 Introduction

Nitrogen in the ocean plays a significant role in the cycling of related biogeochemical cycles. Degradation of organic matter by denitrifying bacteria regenerate inorganic nutrients, *inter alia*, carbon dioxide, ammonium and phosphate. These nutrients are necessary to sustain primary production in the ocean. In addition, nitrogen cycling plays an important role in carbon dioxide sequestration which is linked by different feedback loops (Arrigo, 2005; Gruber, 2004). The global fixed nitrogen inventory is considered by some to be out of balance due to increased oceanic losses gradually exceeding inputs (Codispoti et al., 2001). These findings have directed research into investigating inputs from nitrogen fixation and losses through denitrification and anaerobic ammonium oxidation (anammox) (Ward et al., 2009). Subsequent discoveries of previously unknown nitrogen fixing microbes and anammox both pointed out large uncertainties in the understanding of the global ocean nitrogen cycle (Dalsgaard et al., 2005; Kuypers et al., 2005; Hamersley et al., 2009; Ward et al., 2009; Zehr et al., 2001). Anammox along with conventional denitrification is assumed to be responsible for a considerable amount of the total nitrogen loss from the ocean (Codispoti et al., 2001; Dalsgaard et al., 2003; Gruber and Sarmiento, 1997; Kuypers et al., 2003, 2005). Most of the nitrogen loss is associated with oxygen deficient systems, particularly in OMZs. Although OMZ waters constitute about 0.1% of the ocean, 20% to 40% of the total oceanic nitrogen loss is estimated to occur in these zones (Codispoti et al., 2001; Gruber and Sarmiento, 1997; Gruber, 2004). Strong losses of fixed nitrogen have been observed in OMZs on the shelf along the seafloor or in mid water at or just above the oxycline (Deutsch et al., 2001; Gruber and Sarmiento, 1997; Lam et al., 2009). These losses correspond with lower nitrite, higher ammonium concentrations, highest measured anammox rates and very low oxygen levels (≤ 10 μM, or 0.25 ml/l) (Hamersley et al., 2007; Lam et al., 2009).

Under suboxic and anoxic conditions denitrifying bacteria respire nitrate sequentially to nitrite, nitric and nitrous oxide and finally to nitrogen during heterotrophic denitrification. Heterotrophic denitrification was considered the common mechanism of nitrogen loss in OMZs until the discovery of anammox in waste water bio–reactors (Mulder et al., 1995; Van de Graaf et al., 1995). Before the discovery of anammox, Richards (1966) suggested a similar reaction in anoxic basins of the Framvaren Fjord and the Black Sea. Bender et al. (1989) also proposed the reduction of nitrate/nitrite by ammonium before the experimental evidence of anammox. Since its discovery, there has been ongoing argument that anammox is solely responsible for fixed nitrogen loss in OMZs (Kuypers et al., 2005;

Lam et al., 2009). Several studies used ^{15}N incubations to point out anammox as the key process responsible for nitrogen loss in the OMZs off northern Chile, Peru and in the shelf waters off Namibia (Hamersley et al., 2007; Kuypers et al., 2005; Thamdrup et al., 2006). Heterotrophic denitrification was generally not detected in these studies suggesting that anammox contribute significantly (up to 50%) to nitrogen loss (Devol, 2003). Similar studies carried out in the OMZ regions of the Eastern Tropical South Pacific (ETSP) and the Arabian Sea show different results (Ward et al., 2009). Denitrification rather than anammox has been found to dominate the nitrogen loss in the Arabian Sea. The above study found denitrification in the Arabian Sea to be responsible for 87–99% of the total nitrogen production in seven of eight experiments carried out (Ward et al., 2009). Similar to other OMZs, anammox has been found to dominate in the ETSP. Additionally, abundance of denitrifying bacteria exceeded that of anammox by 7 and 19 fold in the ETSP and Arabian Sea respectively. The high abundance of denitrifying bacteria as compared to anammox suggests that dynamic assemblages of denitrifiers persist in both OMZs (Ward et al., 2009)

In nature anammox bacterial assemblages are less diverse than denitrifying bacteria (Ward et al., 2009). Anammox bacteria are represented by only one or two phylotypes (Jayakumar et al., 2004; Schmid et al., 2007; Woebken et al., 2008). Anammox bacteria are autotrophs that form biomass by fixing carbon and consuming ammonium and nitrite in respiration (Ward et al., 2009). Therefore, it appears anammox is dependent on nutrient regeneration by other processes for supply of required inorganic nutrients and reductants. Denitrification by heterotrophic bacteria is suggested as the supply process for both ammonium and nitrite, which are found in low concentrations in the ocean. This suggestion cause difficulties in understanding how anammox can occur with exclusion of denitrification in some OMZs (Lam et al., 2009). Thus, dissimilatory nitrate reduction has been suggested as a potential source of the ammonium in the ETSP OMZ and that there are other processes that can supply nitrite (Lam et al., 2009). It is was also suggested that in the absence of detectable denitrification, ammonium for anammox would still be remineralized from organic matter through other processes in the ETSP. This study suggested that dissimilatory nitrate reduction occurs as a heterotrophic process and releases ammonium. Studies of dissimilatory nitrate reduction have been restricted to fully anoxic, sulfide rich environments until its detection in the Namibian inner shelf bottom waters (Kartal et al., 2007).

Based on stable isotopes pairing experiments, anammox has been found to obtain 67% or more of nitrite from nitrate reduction (Lam et al., 2009). This process was detected throughout the Peruvian OMZ and has been found to be sufficient enough to supply ammonium requirements of anammox. About 33% or less of the nitrite supply has been attributed to aerobic ammonia oxidation (Lam et al., 2009). The detection of nitrate reduction without denitrification in the Peruvian OMZ is not unusual as nitrate reduction is the first essential step in denitrification and more organisms have been found to be capable of nitrate reduction than complete denitrification (Zumft, 1997). Following these discoveries, a revised nitrogen cycle in OMZs, in which denitrification is deemed unnecessary and nitrite supply is from either aerobic nitrifying or anaerobic nitrate reducing microbes has been suggested (Lam et al., 2009). The ammonium in the revised nitrogen cycle is from dissimilatory nitrate reduction to ammonium. Highest anammox rates are generally detected near the upper edge of the OMZ, and this has been observed in the ETSP (Hamersley et al., 2007). This suggests that there is a close coupling between anammox and aerobic denitrification, which may be able to sustain additional nitrite supply required for anammox (Ward et al., 2009). Direct coupling between anammox and aerobic ammonia oxidation has been reported for the Black Sea even in oxygen concentrations below detection limits (Lam et al., 2007). The discovery of denitrification as the dominant flux for nitrogen in the worlds largest OMZ, in the Arabian Sea, which is responsible for half of the fixed nitrogen loss in the pelagic zone suggests denitrification as the major responsible process (Devol et al., 2006; Ward et al., 2009).

In the Peruvian OMZ, rough estimates of depth–integrated nitrite and ammonium fluxes suggest that 52% to 64% of nitrogen loss originates from upwelled deep sea nitrate and the rest is derived from remineralized nitrogen (Lam et al., 2009). The total nitrogen loss requires a counterbalancing source to maintain fixed nitrogen at roughly constant levels through time (Gruber, 2008).This implies that remineralized ammonium may play a more important role in nitrogen loss than previously estimated. Remineralization of about 3.5 to 7 times the amount of Redfield organic matter (C:N:P = 106:16:1) would be required based on denitrification stoichiometry to counter fixed nitrogen loss (Redfield et al., 1963). Because of disturbances by other closely related elemental cycles, such an increase in remineralization would be unrealistic (Gruber, 2004). As such, alternative remineralized ammonium might come from preferential degradation of organic nitrogen over

carbon in suboxic environments (Van Mooy et al., 2002). More of the ammonium might come from the remineralization of nitrogen enriched organic matter from the spatially coupled nitrogen fixation from above the OMZ (Capone and Knapp, 2007; Deutsch et al., 2007). From these suggestions, calculations of nitrogen loss based on nitrate deficit would be underestimates (Lam et al., 2009). This possibly explains the inconsistencies between nitrogen loss estimates based on nitrate deficit and excess fixed nitrogen (Codispoti et al., 2001).

The roles of denitrification and anammox in the Namibian shelf waters have been investigated by combining microbial and biogeochemical techniques (Kuypers et al., 2005). Maximum nitrate (25–30 μM) concentrations are observed in mid–waters of the shelf and are lower in surface waters because of uptake during phytoplankton growth (Chapman and Shannon, 1985). Vertical distributions of fixed inorganic nitrogen differ significantly between sites, revealing the diverse nature of the Benguela (Chapman and Shannon, 1985). Concentrations of nitrate have been found to drop below 10 μM at the base of the oxic layer (Kuypers et al., 2005), this has been attributed to nitrate conversion to fixed nitrogen by denitrifying bacteria (Tyrrell and Lucas, 2002). Nitrite maxima on the shelf have been observed and associated with the decrease in nitrate concentrations at sites investigated (Kuypers et al., 2005). The N:P ratios in dissolved organic matter have been found to be below Redfield values indicating extensive loss of fixed nitrogen from oxygen deficient waters of sites investigated. Low ammonium concentrations in the Namibian shelf suggest nitrogen loss is due to anammox rather than heterotrophic denitrification (Kuypers et al., 2005). It is suggested that ammonium would accumulate if nitrogen loss was due to heterotrophic denitrification (Richards, 1966). Thus, the low ammonium concentrations in the Benguela OMZ suggest that anammox bacteria play an important role in the removal of nitrogen as concentrations have been found to occur below detection limits in the suboxic zone of some regions investigated for presence of anammox bacteria (Kuypers et al., 2005).

Codispoti and Christensen (1985) documented a correlation between nitrite and ammonium concentrations which often break down below the euphotic zone. Ammonium concentrations diminish and secondary nitrite maxima are frequently observed below the euphotic zone and this is the case particularly in OMZs (Gruber, 2008). The secondary nitrite maxima have been observed in the Arabian Sea (at 100 m and 500 m) and the Eastern Tropical North Pacific (ETNP) (at 250 m and 500 m) and are attributed to denitrification as it

occurs in association with a well–developed anoxic region in mid waters (Gruber, 2008). However, maximum nitrite concentrations have been known to occur outside the region of strongest hypoxia (Codispoti and Christensen, 1985; Codispoti et al., 1986). A correlation between nitrite and ammonium in the Arabian Sea and ETNP has been reported but does not match anammox conditions. As already stated, nitrite and ammonium are used by anammox bacteria during respiration; therefore, these nutrients are expected to be depleted in OMZs where nitrogen loss is predominantly through anammox.

Anammox consumes ammonium and without detectable denitrification in OMZs, dissimilatory nitrate reduction is suggested as a source to sustain ammonium requirements as previously stated (Lam et al., 2009). For nitrite, anaerobic nitrate reduction and aerobic ammonium oxidation have been suggested as alternative sources of nitrite for anammox in the absence of denitrification (Lipschultz et al., 1990). Secondary nitrite maxima unaccounted for are frequently observed in offshore OMZs. It is suggested that the nitrite maxima observed in the offshore eastern tropical south Pacific OMZ are a result of shelf production and horizontal advection (Lam et al., 2009). The correlation between ammonium and nitrite as well as secondary nitrite maxima in the Benguela shelf waters is not well documented. Low ammonium levels have been reported on the Namibian shelf waters and it was suggested that anammox, rather than denitrification is responsible for the nitrogen loss (Kuypers et al., 2005). Ammonium is also consumed during nitrification. Nitrite in the ocean is produced during nitrate assimilation, nitrification and denitrification (Gruber, 2008). Nitrite is short lived and its turnover time has been estimated to be 3–7 days (Lipschultz et al., 1996).

The colorimetric method used to measure nitrite usually involves the reduction of nitrate but in some instances the samples contain concentrations below the detection limit (Gruber, 2008). The method is not very accurate at low concentrations; as such additional low level methods are required to measure nitrite (Dore and Karl, 1996; Lipschultz et al., 1996). In addition, nitrite in OMZs is reduced to dinitrogen gas during denitrification:

$$NO_3^- \rightarrow NO_2^- \rightarrow NO \rightarrow N_2O \rightarrow N_2$$

This process reduces the accumulation of nitrite leading to concentrations below the detection limit in some regions.

As previously stated, the stepwise reduction of nitrite during denitrification results in the production of nitrous oxide and subsequent loss of nitrogen. Nitrous oxide is a greenhouse gas considered to have a global warming potential about 265–310 times higher than that of carbon dioxide, on a 100 years timescale (EPA, 2015). Nitrous oxide production by denitrification in suboxic waters has been found to exceed production from nitrification (Bange, 2008). Production from nitrification has also been found to increase significantly under suboxic conditions (Goreau et al., 1980). Previous studies reveal subsurface nitrous oxide maxima in the Atlantic, Pacific and Indian oceans which occur at minimum dissolved oxygen and maximum nitrate concentrations (Butler et al., 1989; Cohen and Gordon, 1978; Oudot et al., 2002). These maxima are attributed to nitrification as they correlate with water age distribution (Bange and Andreae, 1999). Nitrous oxide maxima in suboxic zones have been observed to show a two–peak structure at the upper and lower boundaries of the OMZ (Bange, 2008). This suggests that OMZs contribute significantly to nitrous oxide production. Upwelling systems as sites of nitrous oxide production have been receiving attention. It is important to study processes that control nitrous oxide production on the shelf to aid in understanding its biogeochemical relevance in the context of climate predictions.

In this chapter, the BioEBUS model is applied in the Benguela to study intermediary nitrogen processes and associated nitrogen loss mechanisms. The seasonal distribution of nitrite both in and outside the OMZ is investigated. The evolution of nitrite formed on the continental shelf is also investigated and the physical processes involved are explored. The nitrite equation included in the model allows for nitrification under oxic conditions and denitrification/anammox under suboxic conditions (Gutknecht et al., 2013). Since these processes are oxygen dependent, the oxygen equation allows for oxic/suboxic processes with source and sink terms being photosynthesis, zooplankton respiration, bacterial remineralization as well as sea–air oxygen fluxes. Anammox, denitrification and nitrification rates in the Benguela are also investigated through the diagnostic run. Through the simulated rates, the dominant process responsible for nitrogen loss in the Benguela OMZ is determined. Nitrous oxide production in the Angola–Benguela front and off Walvis Bay and the dominant production and consuming processes are also investigated.

4.2 Nitrite distribution in the Benguela OMZ

The BioEBUS model simulation is used to study nitrite dynamics in the Benguela and its associated OMZ. The distribution of nitrite in the Benguela shelf waters of the ABF and Walvis Bay is investigated in this section. Seasonal distribution of nitrite in the OMZ, the evolution of both maxima (primary and secondary) and the biogeochemical processes involved are also investigated. The greenhouse gas (nitrous oxide) which is formed during the stepwise reduction of nitrite and its implication for nitrogen loss in the Benguela is also investigated.

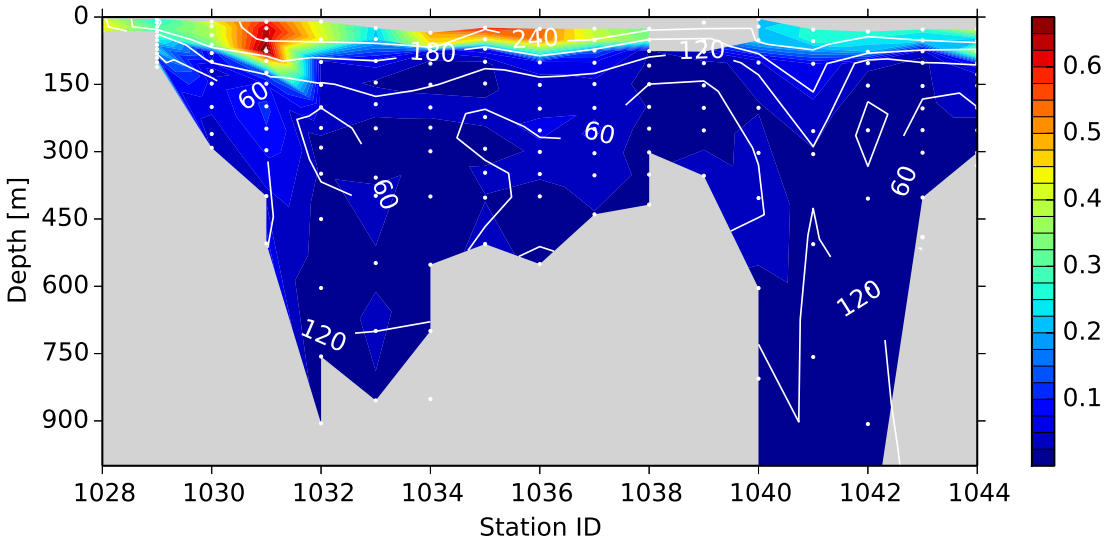

Figure 4.1: Section of nitrite concentrations [mmol N m^{-3}] off Namibia. The dots white lines denote where nitrite measurements were taken during the MSM 19/1b cruise. The horizontal axis indicates sequence of the sampled stations during the cruise.

The vertical distribution of nitrite in the ABF and off Walvis Bay from the simulation is shown in (Figure 4.2). Simulated nitrite concentrations in both regions follow a two peak profile with high concentrations in the euphotic zone (0–50 m – primary maxima) and at depth (below 100 m – secondary maxima). The primary nitrite maxima in both regions occur in well–oxygenated waters (> 60 mmol O_2 m^{-3}). The primary nitrite maxima peak in association with the nitracline (peak gradient in nitrate concentrations in the water column)

occur around the 50 m depth. Due to high primary production rates in the euphotic zone, the primary nitrite maxima are associated with nitrification and release by phytoplankton (Ward et al., 1982; Lomas and Lipschultz, 2006). The peak in nitrite concentrations in the nitracline is attributed to nitrate assimilation (Dore and Karl, 1996; Herbland and Voituriez, 1979). Winter (July 1999) cross–shelf transects of nitrite at 19°S in the Benguela exhibited a similar two peak profile with high concentrations in the euphotic zone (30–50 m) and at depth ($\sim$ 100 m) (Dittmar and Birkicht, 2001). A similar nitrite profile has been observed in the nearshore stations (1028–1033) during the spring MSM 19/1b cruise, with the secondary maximum located at 100–200 m (Figure 4.1). Simulated nitrite concentrations reach up to 0.33 mmol N m^{-3} which is within range of the MSM 19/1b data. Within the OMZ the nitrite concentrations are below 0.1 mmol N m^{-3} in both simulated and MSM 19/1b data off Walvis Bay (station 1040–1044). Discrepancies are observed with surface concentrations and these are due to differences from cruise sampling dates and annual mean concentrations in the model. The differences between nitrite concentrations in the model and data can also be attributed to the short turnover rate as nitrite is rapidly converted to nitrate by nitrification. In validation of the BioEBUS model it was found that nitrite concentrations were also low but within the range of observed data (Gutknecht et al., 2013). Nitrite concentrations above 1–4 mmol N m^{-3} were associated with low oxygen ($\leq$ 4.5 mmol O_2 m^{-3}) not captured by the model (Gutknecht et al., 2013). In comparison to previous studies, maximum nitrite concentrations in the Benguela vary significantly (Table 3.1). Due to the short turnover rate of nitrite, it is difficult to draw conclusions and more data is required.

Simulated secondary nitrite maxima accumulate in the ABF OMZ at 100–200 m. These maxima occur within the pronounced OMZ on the continental shelf between 11–11.5°S ($\sim$ 50 km from the coast). There is no clear depth of transition between primary and secondary nitrite maxima in this region. The simulated secondary maxima off Walvis are depleted and located on the shallow shelf slope (120–200 m). A distinct transition zone marked by low nitrite concentrations, is observed between the primary and secondary maxima at $\sim$ 75–100 m in the nearshore region. The low secondary nitrite concentrations off Walvis Bay are thought to indicate consumption through anammox (as discussed in section 4.3). Anammox bacteria fix carbon and consume nitrite in respiration as previously stated (Strous et al., 1997). The strong secondary nitrite maxima in the ABF are attributed to denitrification because of the strong association with the pronounced OMZ. Similar secondary nitrite maxima from denitrification have been observed in the ETNP and the Arabian Sea OMZs

(Gruber, 2008). The secondary nitrite maxima in both regions were low when compared with primary maxima. These low secondary maxima and their location in the OMZ are thought to result from nitrite formation by nitrification as the dominant process rather than denitrification (Yakushev and Neretin, 1997). The secondary nitrite maxima in the ETSP have been linked to nitrate reduction in the OMZ due to undetectable denitrification (Lam et al., 2009). Depletion and accumulation of nitrite in the Benguela OMZ is more complicated and it is not limited to anammox and denitrification. Therefore, interpretations of the seasonality and interactions between nitrification, anammox and denitrification in the Benguela OMZ are investigated.

Simulated seasonal distribution of nitrite in the Benguela OMZ is shown in (Figure 4.2a–d). The nitrite layer in the OMZ is observed on the shallow continental shelf at $\sim$ 80–600 m. Nitrite accumulates in the OMZ north of 18°S and the ABF region throughout the annual cycle. Maximum nitrite concentrations are observed in the ABF region during autumn and spread southward to 21°S on the Namibian shelf (Figure 4.2b). The maximum nitrite concentrations on the Namibian shelf occur in the region between 18 and 21°S during autumn. Off Walvis Bay ($\sim$ 23°S), nitrite concentrations are generally depleted at $\sim$ 100–300 m throughout the seasonal cycle. A similar distribution pattern of nitrite has been observed from Dittmar and Birkicht (2001) at 100 m in the ABF and off Namibia during winter. Nitrite concentrations in Dittmar and Birkicht (2001) also increased exponentially from offshore to onshore corresponding with this study and were attributed to bacterial degradation of organic matter. During spring and summer, nitrite concentrations are depleted in the Namibian shelf waters. Low nitrite concentrations are observed in the ABF region during summer but are not below the typical detection limit (< 0.01 mmol N m^{-3}). These results suggest that there are different processes that drive the seasonal distribution of nitrite in the OMZ of the ABF region and the Namibian shelf.

The evolution of simulated nitrite formed on the continental shelf is presented through Hovmöller diagrams (Figure 4.4a–b). The Hovmöller diagrams represent the ABF zone and the Namibian shelf region off Walvis Bay. Depth–integrated nitrite concentrations in the ABF and Walvis Bay occur throughout the annual cycle. Maximum nitrite concentrations develop on the continental shelf area between 11–11.5 and 13–14.5°S during summer and

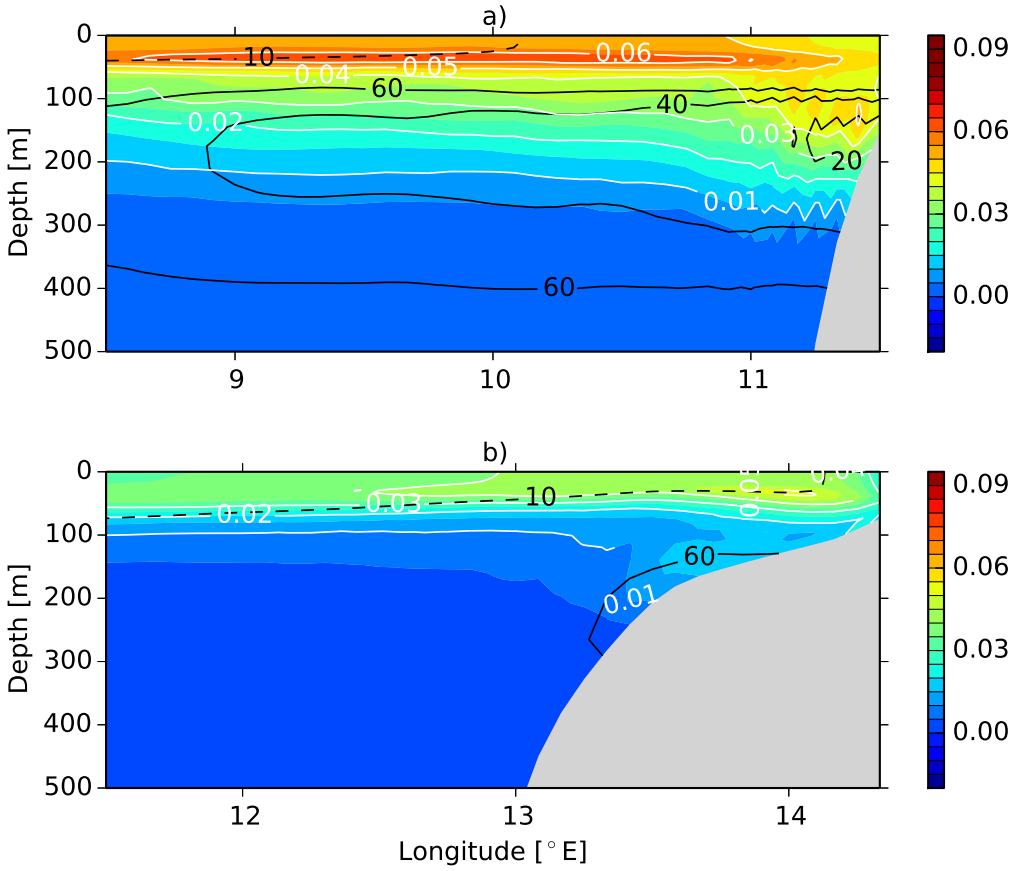

Figure 4.2: Simulated nitrite distribution in shelf waters of the (a) ABF and (b) off Walvis Bay. Black and white contours represent oxygen [mmol O_2 m^{-3}] and nitrite [mmol N m^{-3}] respectively. The nitracline [mmol N m^{-3}] is shown by the dashed lines. Cross–shelf sections were extracted and averaged between 16–18°S and 22–24°S for the ABF and off Walvis Bay respectively.

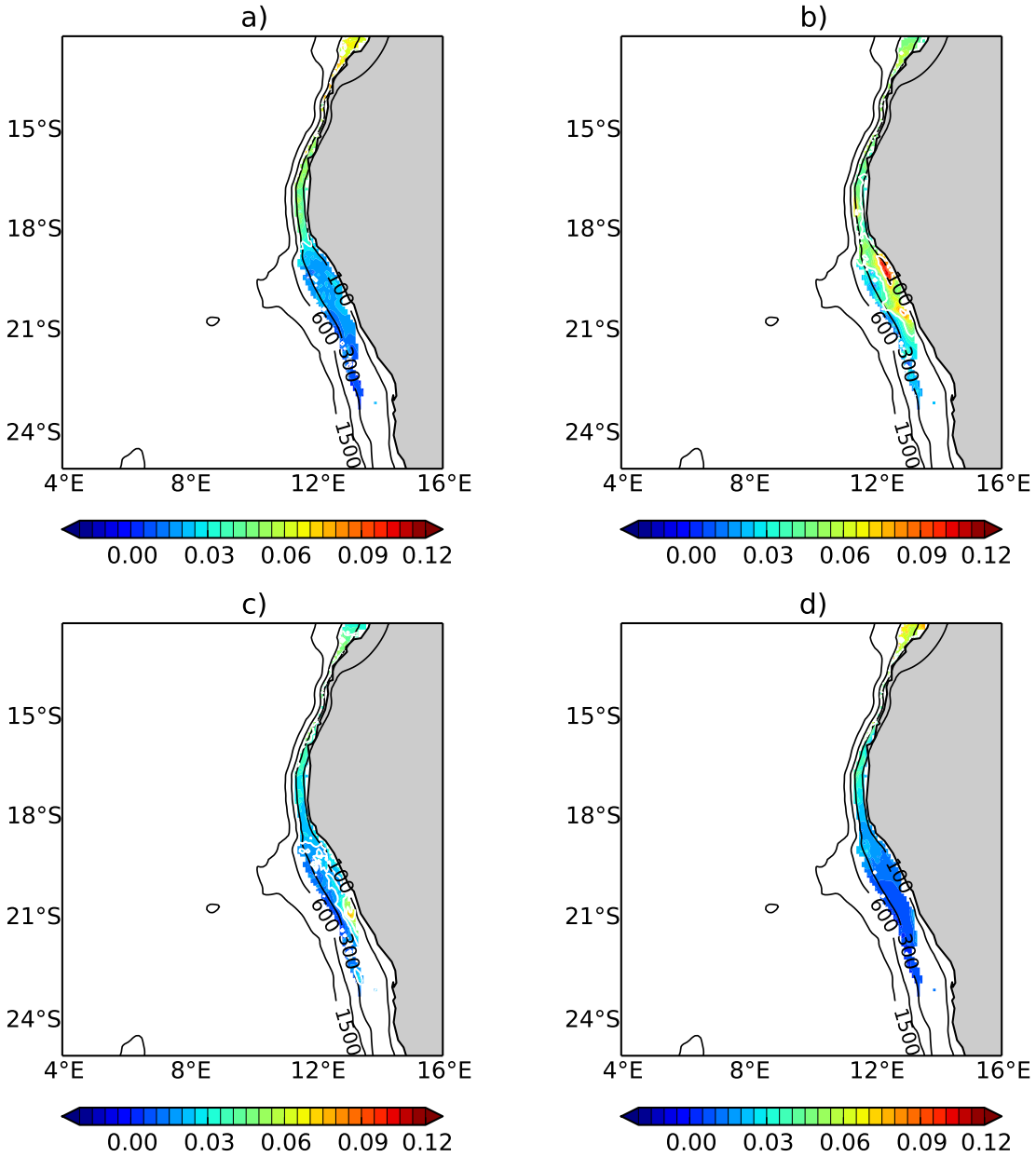

Figure 4.3: Isoslice of simulated nitrite concentrations [mmol N m^{-3}] in the Benguela OMZ during (a) summer, (b) autumn, (c) winter and (d) spring. Black contours represent water depths at 100, 300, 600 and 1500 m.

autumn. The nitrite in the ABF is advected offshore throughout the annual cycle with the strongest advection observed during late autumn (May). Advection of nitrite in this region coincides with the increased wind stress conditions during autumn which result in a strong Ekman offshore transport (Mohrholz et al., 2001). The nitrite peak also occurs during the autumn upwelling season in the northern Benguela. Off Walvis Bay, the nitrite maxima are restricted to the shelf. Both nitrite peaks in these regions occur during summer when the poleward moving SACW dominates the Benguela (Mohrholz et al., 2008).

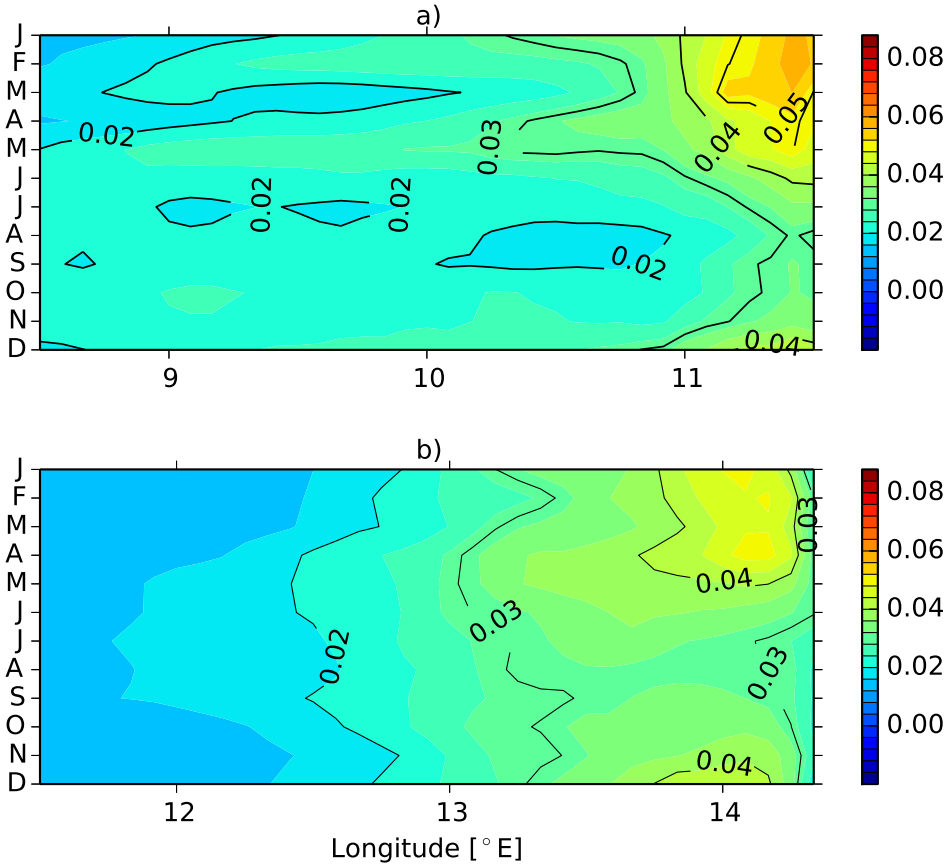

Figure 4.4: Hovmöller diagrams of simulated nitrite [mmol N m^{-2}] in the (a) ABF and (b) off Walvis Bay. Sections were extracted and averaged between 16–18°S and 22–24°S for ABF and off Walvis Bay respectively. The nitrite concentrations were integrated at depth.

4.3 Nitrification, anammox and denitrification in the Benguela

Consideration is now given to the biogeochemical processes that drive the seasonality of intermediary nitrogen processes in the Benguela. Normalized time–series and correlation graphs of oxygen against nitrate, nitrite and ammonium in the ABF OMZ and off Walvis Bay are shown in (Figure 4.5) . The model time–series exhibit distinct seasonal cycles and interactions between these nutrients. It has been stated that nitrite concentrations in the ABF peak during summer following the spring upwelling season (Figure 4.5b). These nitrite concentrations peak in suboxic conditions since the OMZ in this region is permanent. A strong negative correlation between oxygen and nitrite in the ABF is evident (Figure 4.5e). This strong correlation and depletion of nitrate during summer indicate that the nitrite maxima are formed predominantly through nitrification and denitrification (Table 4.1). Similarly, the nitrite concentrations off Walvis Bay peak steadily during summer. A negative correlation between oxygen and nitrite is observed during early (December) and late summer (February). This suggests that the nitrite maxima are formed during nitrification and denitrification as in the ABF (Table 4.1). The weak negative correlation between oxygen and nitrate during this period indicates that there are other processes involved, the main candidate being anammox. Nitrite concentrations in the ABF decline steadily with increasing oxygen throughout the autumn season. The weak negative correlation between oxygen and nitrite during early autumn shows a decrease in nitrification and denitrification rates. This is supported by a positive linear correlation between oxygen and nitrate during autumn. These results do not suggest that conditions in the ABF switch from suboxic to oxic during autumn since the OMZ is permanent. Increased upwelling intensity and weakened poleward flow of the SACW drive are thought to drive these conditions. The warm, oxygen–depleted SACW in this region is replaced by cold upwelled water resulting in improved oxygen concentrations (Mohrholz et al., 2001). In contrast, the nitrite concentrations off Walvis Bay are maximal during autumn. The weak positive correlation between oxygen and nitrite and the peak in nitrate concentrations point to a shift in conditions. The sudden decline in ammonium concentrations suggests that nitrification dominates the shelf as the poleward SACW weakens and oxygen conditions improve.

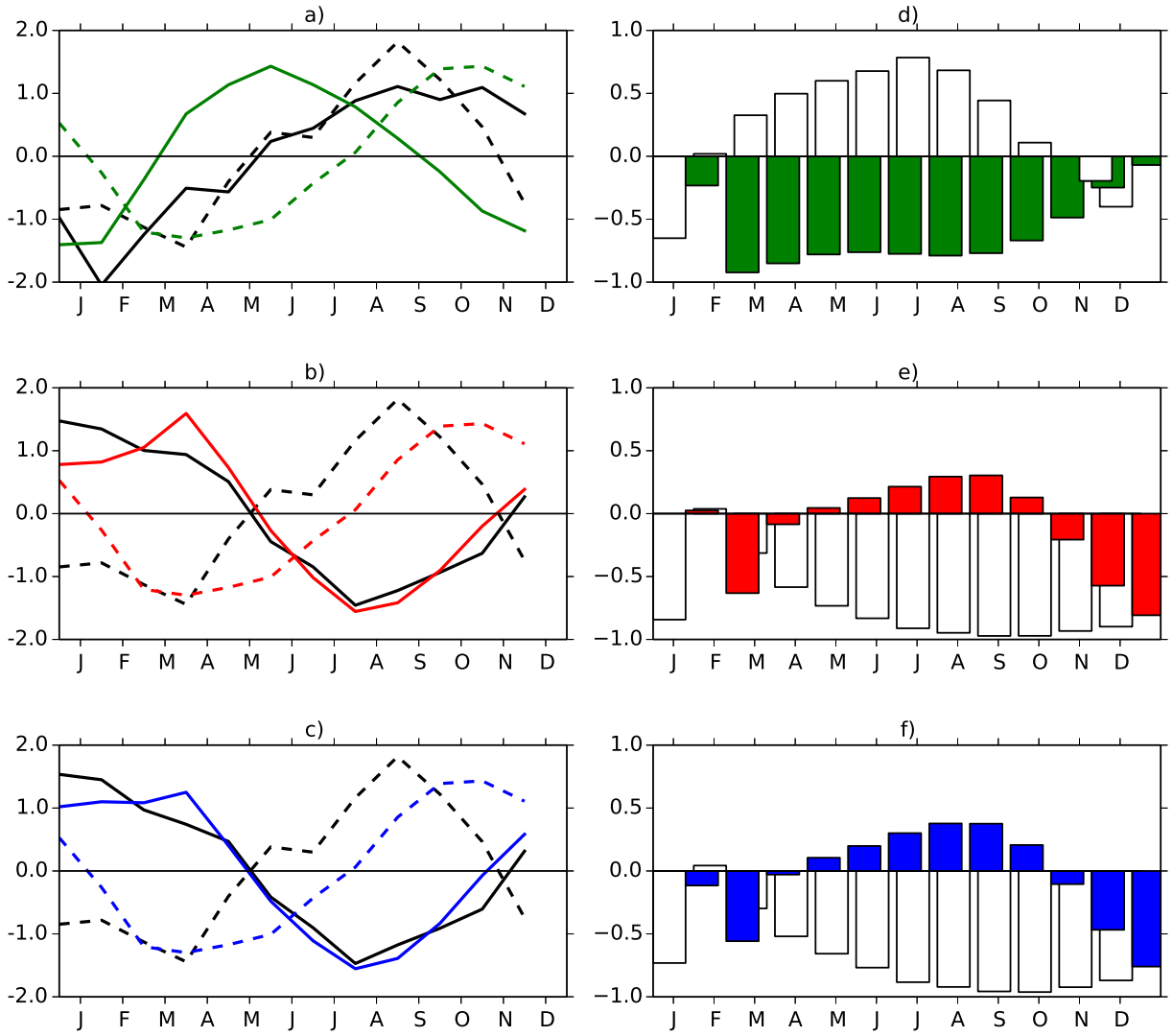

Figure 4.5: Normalized time–series of simulated oxygen against (a) nitrate, (b) nitrite and (c) ammonium in the ABF (black) and off Walvis Bay (grb). Solid lines represent nitrate, nitrite and ammonium. Dashed lines represent oxygen in the ABF (black) and Walvis Bay (grb). Correlation bar graphs of oxygen versus (d) nitrate, (e) nitrite and (f) ammonium in the OMZ of the ABF (white) and off Walvis Bay (grb). Sections were extracted and averaged between 16–18°S, 8.5–11.5°E and 22–24°S, 11.5–14.5°E for ABF and off Walvis Bay respectively.

Simulated nitrite and ammonium concentrations off Walvis Bay are both depleted during winter reaching minimum concentrations in late winter (August), indicative of consumption by anammox. Since anammox bacteria are autotrophs that form biomass by consuming ammonium and nitrite, they require a supply of these nutrients from other processes including denitrification (Ward et al., 2009). However, anammox has been observed to occur without denitrification in the Namibian shelf waters, therefore causing difficulties in understanding the supply process for anammox (Kuypers et al., 2005). The anammox experimental results in the cited study were performed at specific sites on the shallow continental shelf (< 200 m) during autumn (March and April). It has been suggested that without detectable denitrification, ammonium for anammox could still be remineralized from organic matter through other processes (Lam et al., 2009). Dissimilatory nitrate reduction has been suggested as a potential source of ammonium and it has been detected in the Benguela OMZ (Kartal et al., 2007). No conclusive results can be made on dissimilatory nitrate reduction as the process is not included in the BioEBUS model. In the case of nitrite, supply for anammox can be obtained predominantly from nitrate reduction (Lam et al., 2009). Simulated results from this study show that denitrification off Walvis Bay is detectable on a larger scale throughout the annual cycle (Table 4.1), therefore, these nutrients are available for anammox consumption. In mid–autumn (April), simulated denitrification rates decline as nitrite concentrations peak with declining ammonium and increasing nitrate. To further sustain additional nitrite requirements for anammox, it has been suggested that there is a coupling between anammox and aerobic ammonia oxidation (Lam et al., 2007). Anammox rates on the Namibian shelf have been found to be at a maximum between 100–115 m (Kuypers et al., 2005). Simulated ammonium and nitrite maxima from nitrification occur just above the upper depth of the OMZ off Walvis Bay. Model results from this study also suggest that nitrification dominates the shallow shelf region (Figure 4.8). Since there is nitrification and a possible link between primary and secondary nitrite maxima in the transition depth of the OMZ, there may be a coupling between anammox and aerobic processes. Interaction between annamox and aerobic processes may be occurring at the oxic–suboxic interface ($O_2 = 60$ mmol O_2 m^{-3}).

The depleted nitrite concentrations in the ABF during winter are attributed to nitrification and denitrification. Nitrite during this period is reduced to nitrous oxide and the pool is exhausted since consumption exceeds production. Nitrous oxide production in the Benguela OMZ is explained further in the subsequent section. Nitrite concentrations in both regions

peak steadily with declining oxygen during spring and this is attributed to denitrification (Table 4.1). There is a strong correlation between nitrite and ammonium in the Benguela OMZ. This correlation between ammonium and nitrite in OMZs has been observed to break down below the euphotic zone (Gruber, 2008). A secondary nitrite peak has been observed (reported in this study) whilst ammonium concentrations declined. This trend is also observed during autumn in the ABF OMZ indicating a strong presence of denitrifying bacteria. The correlation between ammonium and nitrite off Walvis Bay is strong and follows a similar trend throughout the seasonal cycle.

Table 4.1: Simulated seasonal rates [10^{-2} mmol N m^{-3} d^{-1}] of nitrification, anammox and denitrification.

Process	Season	ABF	Walvis Bay
Nitrification	Summer	0.0−43	0.0−55
Anammox		0.0−2.8	0.0−21
Denitrification (Detritus)		0.0−8.6	0.0−18
Denitrification (DON)		0.0−3.9	0.0−2.9
Nitrification	Autumn	0.0−34	0.0−57
Anammox		0.0−2.9	0.0−20
Denitrification (Detritus)		0.0−5.3	0.0−18
Denitrification (DON)		0.0−1.5	0.0−3.4
Nitrification	Winter	0.0−28	0.0−36
Anammox		0.0−3.1	0.0−12
Denitrification (Detritus)		0.0−6.2	0.0−9.3
Denitrification (DON)		0.0−2.9	0.0−2.8
Nitrification	Spring	0.0−34	0.0−45
Anammox		0.0−2.4	0.0−7.9
Denitrification (Detritus)		0.0−8.7	0.0−12
Denitrification (DON)		0.0−3.4	0.0−3.4

The different physical and biogeochemical processes that drive nitrite concentrations in the ABF and off Walvis Bay highlight the diverse nature of the Benguela. Nitrite dynamics in the

ABF are predominantly controlled by the advected nutrient rich, oxygen–depleted SACW from the Angola gyre. These waters, combined with upwelling events, create favorable conditions for denitrification in the ABF OMZ. Increased offshore Ekman transport results in the offshore advection of nitrite formed on the shelf in the ABF OMZ. Nitrite maxima off Walvis Bay appear to develop but are restricted to the shelf. Denitrification off Walvis Bay plays a smaller role in the formation and consumption of nitrite than nitrification and anammox respectively (Table 4.1). The depleted nitrite concentrations and high rates (Table 4.1) off Walvis Bay suggest that anammox contributes significantly as reported in the literature e.g. (Kuypers et al., 2005). Coupling between anammox and aerobic processes appears to exist but complex processes are at work and it is beyond the scope of this study to make firm conclusions. Equatorward flow and intrusion onto the Namibian shelf by well–oxygenated ESACW favor nitrification during autumn to winter. Since the OMZ only covers the shallow slope of the continental shelf, the contribution of nitrification off Walvis Bay cannot be overlooked. The same applies for the ABF region since nitrification has been established as a dominant nitrite formation process (Yakushev and Neretin, 1997). The role played by the processes that control nitrite dynamics in the formation of nitrous oxide are explored.

4.4 Water–column nitrous oxide production processes

Simulated time–series results of nitrous oxide production in the ABF and Walvis Bay are presented in figures 4.6a–b. Nitrous oxide production occurs throughout the annual cycle in the ABF. The nitrous oxide production in this region occurs within the OMZ between 50–200 m and deeper (Figure 4.6b). Maximum nitrous oxide production occurs during autumn to winter and reaches a minimum during spring. Additionally, maximum nitrous oxide production in the ABF occurs at suboxic conditions. Since there is no distinct depth of transition between primary and secondary nitrite maxima in the ABF, nitrous oxide production in this region is linked to both nitrification and accelerated production under suboxic conditions. However, the increased nitrous oxide concentrations in the core of the OMZ (20–40 mmol O_2 m^{-2}) indicate both accelerated production under suboxic conditions increased denitrification rates. Nitrous oxide cycling and distribution in the ocean are highly depended on organic carbon and oxygen concentrations (Babbin et al., 2015). Therefore, nitrous oxide production is accelerated in suboxic conditions and rapid cycling is expected with expansion of suboxic waters (Babbin et al., 2015). The nitrous oxide profile in the ABF follows a similar two peak structure exhibited by nitrite. Similar nitrous oxide profiles have

been observed in suboxic zones of the Arabian Sea and ETNP (Bange, 2008). The maximum nitrous oxide concentrations in the ABF OMZ core contrast with results from the Arabian Sea (Bange et al., 2001), where depleted nitrous oxide concentrations are known to occur in the OMZ core. Nitrous oxide production off Walvis Bay is low and depleted concentrations occur throughout the annual cycle when compared to the ABF. In contrast, nitrous oxide concentrations off Walvis Bay peak during autumn in well–oxygenated waters (<60 mmol O_2 m^{-2}). These concentrations off Walvis Bay are attributed to high nitrification rates and reduced production in oxygenated conditions (Table 4.2).

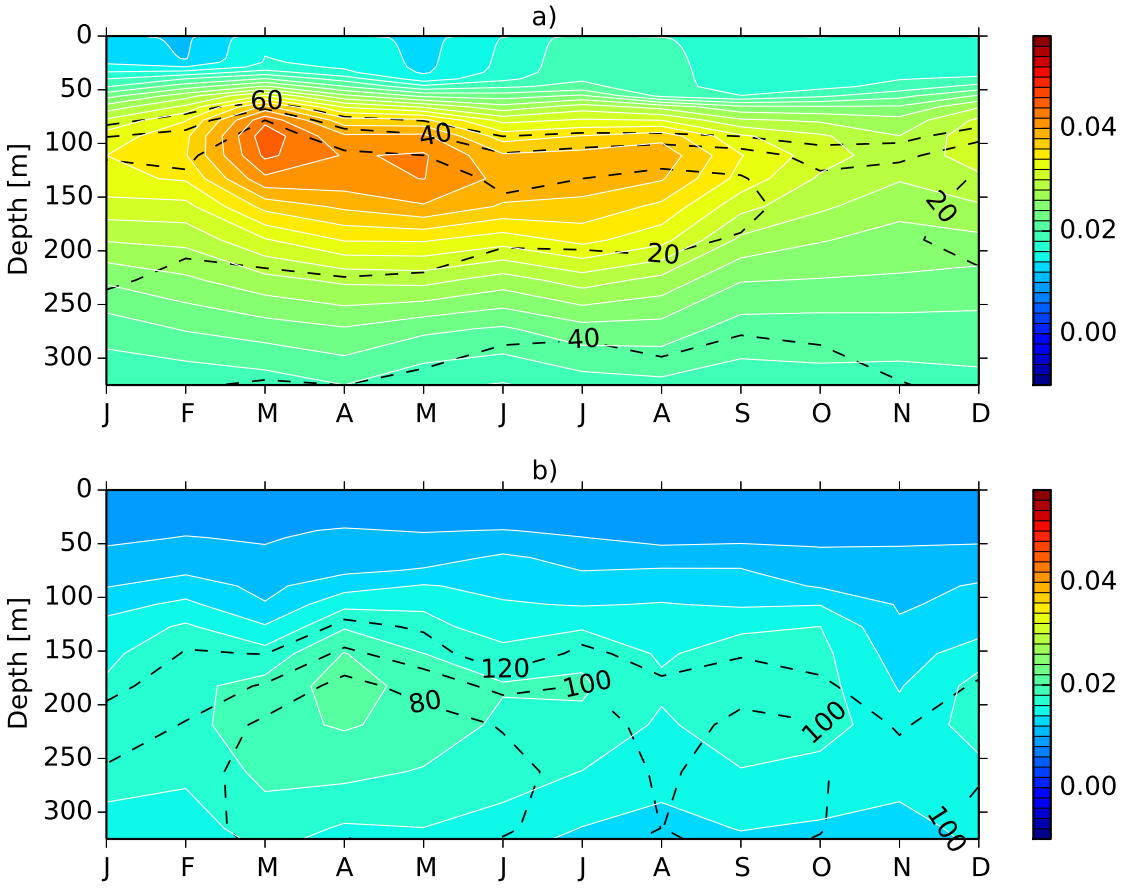

Figure 4.6: Time–series of nitrous oxide concentrations [mmol N m^{-3}] in the (a) ABF and off (b) Walvis Bay. Black contours represent oxygen concentrations [mmol O2 m^{-3}]. Sections were extracted and averaged between 16–18°S, 8.5–11.5°E and 22–24°S, 11.5–14.5°E for ABF and off Walvis Bay respectively.

Scatter plots of nitrous oxide vs apparent oxygen utilization (AOU) are presented in figures 4.7a–d. The scatter plots reveal three distinct water masses associated with AOU and nitrous oxide production in the ABF region. In contrast, only two water masses are identified off Walvis Bay. The different water masses associated with the nitrous production in both regions are observed throughout the seasonal cycle. Second degree polynomial curves of nitrous oxide in the ABF zone show non–linearity and do not fit most points. This may be a result of the three different nitrous oxide production sources. The polynomial curves off Walvis Bay are also non–linear but fit through most of the points. A distinct, positive linear relationship between nitrous oxide and AOU is observed within the 0–100 m depth in the ABF region throughout the seasonal cycle. At 100–500 m depths, nitrous oxide production appears to be constant but reaches high rates. A similar trend is observed with deeper water masses at 500–1000 m. An increasing, positive non–linear relationship between AOU and nitrous oxide off Walvis Bay in the upper water column (0–100 m) is evident. The nitrous oxide and AOU at intermediate depths (100–500m) also appear to have a positive non–linear relationship. Nitrous oxide production in the ABF peaks during autumn and winter. As stated previously, low nitrous oxide production in this region occurs during spring. Nitrous oxide production off Walvis Bay appears to be relatively constant through spring to autumn and increases during winter when the shelf is well–oxygenated.

Table 4.2: Simulated annual mean rates [mmol N m^{-2} d^{-1}] of nitrification, anammox and denitrification at i (0–100 m), ii (100–500 m) and iii (500–1000 m).

Depth [m]	Nitrification	Anammox	Denitrification (Detritus)	Denitrification (DON)
Walvis Bay				
i	0.217	0.002	0.003	0.001
ii	0.042	0.019	0.018	0.002
iii	0.001	0.000	0.000	0.000
Angola–Benguela Front				
i	0.201	0.000	0.002	0.001
ii	0.028	0.000	0.004	0.001
iii	0.001	0.000	0.000	0.000

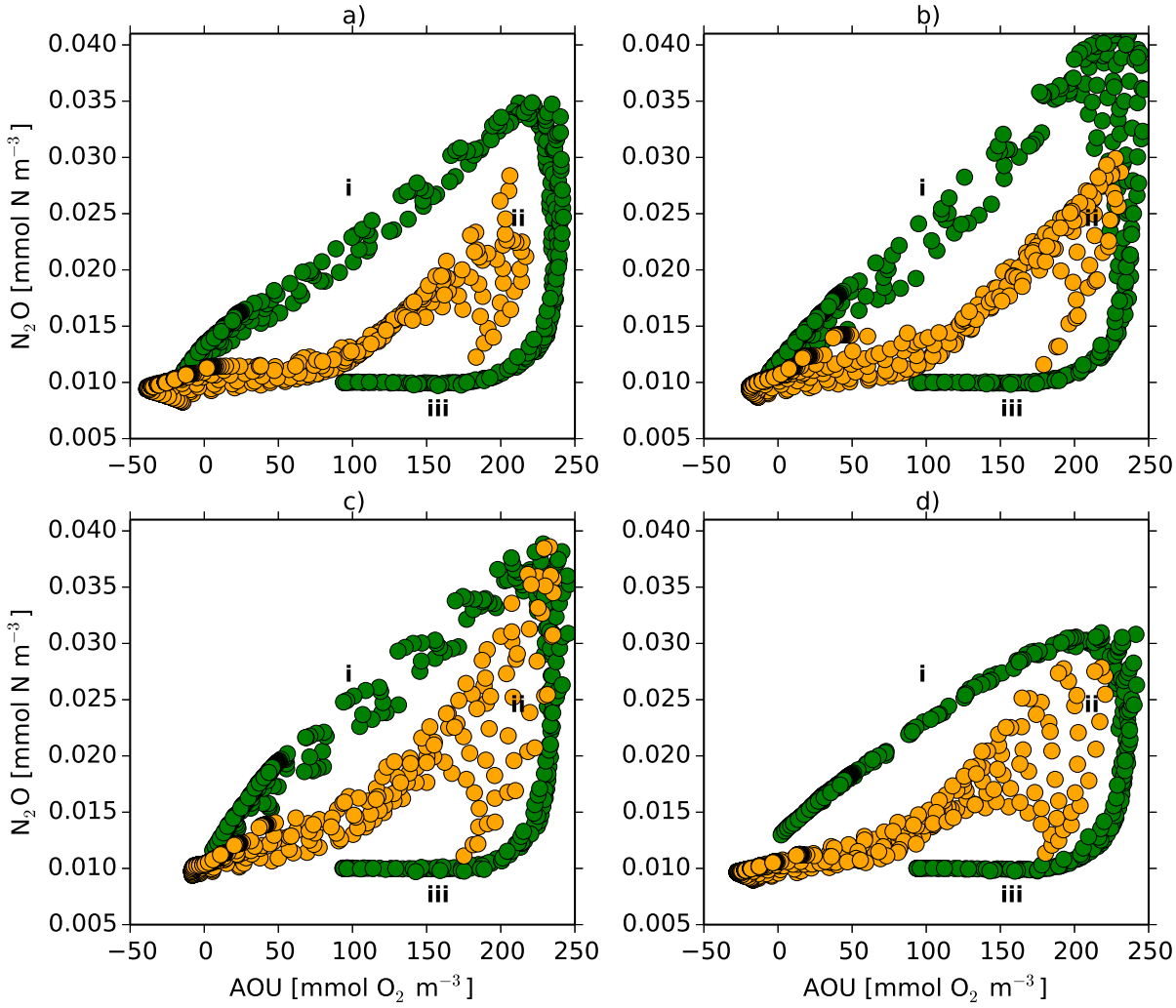

Figure 4.7: Scatter plots of simulated AOU [mmol N m^{-3}] versus nitrous oxide [mmol N m^{-3}] in the ABF (green) and off Walvis Bay (orange) during (a) summer, (b) autumn, (c) winter and (d) spring. Water depth of the water masses is denoted by (i-thermocline) 0–100 m, (ii-intermediate) 100–500 m and (iii-deeper) 500–1000 m. Sections were extracted between 16–18°S, 8.5–11.5°E and 22–24°S, 11.5–14.5°E for ABF and off Walvis Bay respectively.

Previous studies reported slopes of the linear relationship between nitrous oxide and AOU that varied between $3\times\ 10^{-5}$ and $3\times\ 10^{-4}$ (Bange, 2008; Nevison et al., 2003). The slopes of the non–linear relationship between nitrous oxide and AOU range between $2.26\ \times 10^{-5}$ – $4.59\times\ 10^{-5}$ off Walvis Bay. The range of the non–linear relationship slopes off Walvis Bay are in agreement with these studies. The linear relationships between nitrous oxide and AOU in these studies were attributed to nitrification, as it is suggested off Walvis Bay. A weak signal of accelerated nitrous oxide production under low oxygen conditions is also exhibited in intermediate waters off Walvis Bay. Nitrous oxide formation in the ABF is more complex, hence the non–linear relationship slope is outside the typical range. The presence and formation of nitrous oxide in deeper water masses and pronounced OMZ in the ABF contribute to this difference. High nitrous oxide production in the ABF peaks at the transition zones between oxic and suboxic waters ($\sim$ 100–200 m). Since the transition zone is not clearly defined, it is suggested that a coupling between nitrification and denitrification may exist. This coupling has been identified in suboxic waters (ETNP and Arabian Sea) with a non–linear AOU and nitrous oxide relationship (Bange, 2008).

The coupling between nitrification and denitrification in the Arabian Sea has been identified at $\sim$ 100 m as suggested this study. In contrast to the Arabian Sea, nitrous oxide in the ABF OMZ core is not depleted suggesting that advected SACW from the Angola gyre contributes significantly to its net production. Isotopic nitrous oxide measurements revealed that its production can occur by nitrification through hydroxylamine or nitric oxide and by nitrification–denitrification through nitrite reduction (Ostrom et al., 2000). Nitrification can be detected at most depths unlike the nitrification–denitrification pathway which occurs at particular depths as suggested in this study. The nitrification–denitrification coupling can occur through nitric oxide formation during nitrification followed by reduction to nitrous oxide during denitrification (Naqvi et al., 1998).

Production of nitrous oxide associated with deeper water masses (iii) in the ABF occurs in higher nitrification rates than denitrification (Table 4.2). The clear continuous trend between intermediate and deeper waters suggests a transition from denitrification to nitrification and a possible coupling. A deeper nitrous oxide peak attributed to nitrification has been observed at 400–800 m in the Arabian Sea which corresponds with the one observed in this study (Bange et al., 2001). The nitrification–denitrification coupling detected at 350–500 m in the Arabian Sea by Ostrom et al. (2000) is suggested at 500–600 m in the ABF. Ji et al.

(2015) reported increased nitrous oxide production from nitrification and denitrification at the oxic–anoxic interface in the ETSP OMZ suggesting a coupling between the two processes. About 50% inhibition of nitrous oxide production through denitrification has been reported in oxygen levels below 0.297 μM (Dalsgaard et al., 2014). Oxygen concentrations in this study do not reach such low levels. A previous isotopic study was able to distinguish between nitrous oxide formed during oxidation and reduction but was unable to isolate specific production pathways (Sutka et al., 2006). Therefore, determining the dominant nitrous oxide production pathway at the oxic–suboxic interface in particular is difficult to resolve. The results reported in the present study suggest that nitrous oxide is predominantly formed during nitrification off Walvis Bay as opposed to accelerated production under low oxygen concentrations and denitrification. Nitrous oxide formation is more complex in the ABF with a strong nitrification–denitrification coupling suggested between oxic and suboxic waters.

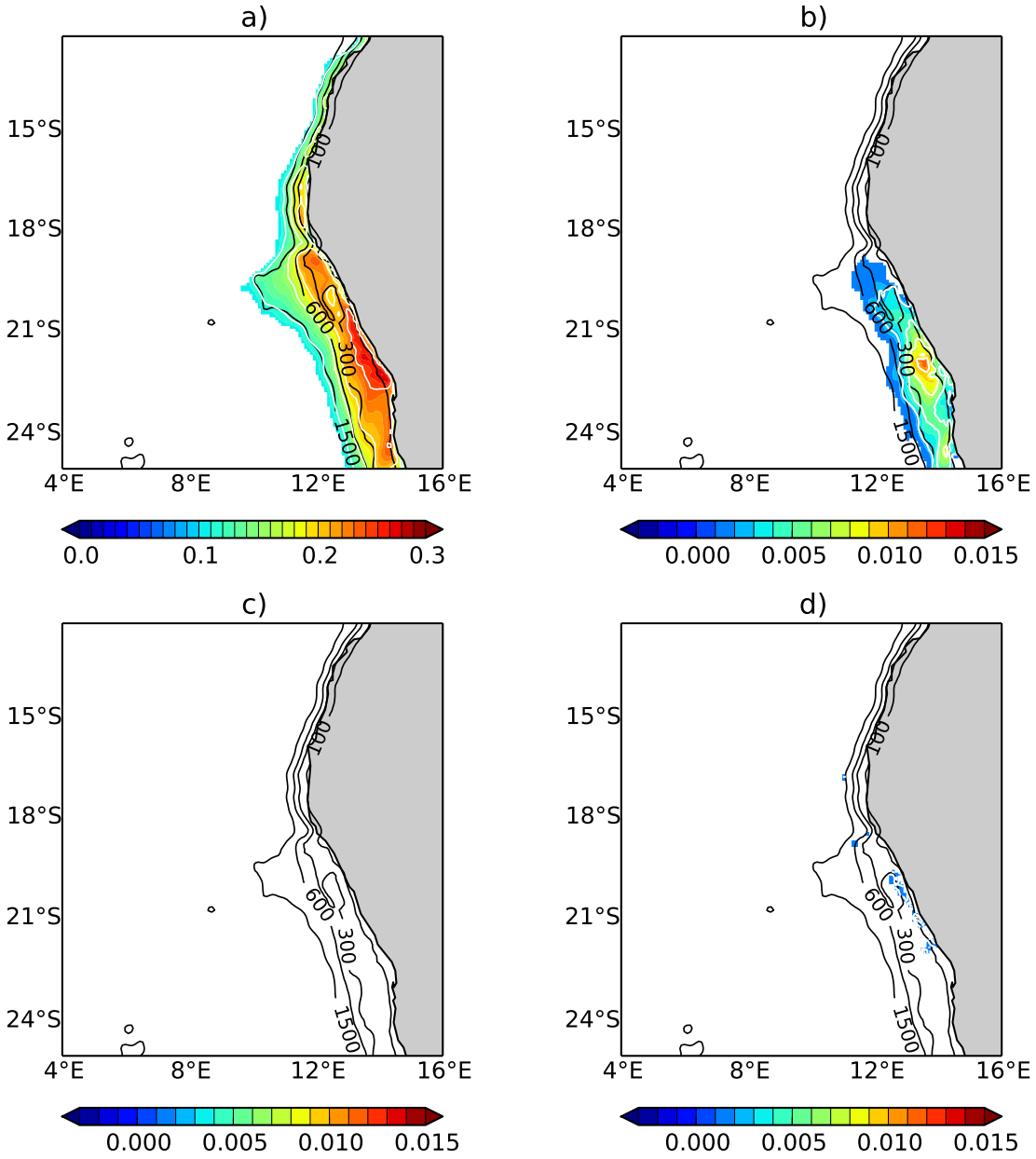

Figure 4.8: Depth–integrated N flux concentrations [mmol N m^{-2} d^{-1}] in the Benguela due to (a) nitrification (b) anammox (c) denitrification (detritus) and (d) denitrification (DON). Black contours represent water depths at 100, 300, 600 and 1500 m.

Subsequent reduction of nitrous oxide to dinitrogen gas results in nitrogen loss from the Benguela. Nitrous oxide emissions from the diagnostic run reach up to 2.5×10^{-2} mmol N m^{-2} d^{-1}. Gutknecht et al. (2013) reported similar estimates which compared well with in–situ data and cited literature. In general, simulated N fluxes in the Benguela show that nitrification dominates the shelf region. Annual mean depth–integrated N fluxes due to nitrification reach up 27×10^{-2} mmol N m^{-2} d^{-1} on the shallow continental shelf region (Figure 10a). In the OMZ, N fluxes due to denitrification reach up to 1.5×10^{-2} mmol N m^{-2} d^{-1} (Figure 4.8b). Anammox fluxes in the OMZ reach up to 0.9×10^{-2} mmol N m^{-2} d^{-1} (Figure 4.8c), corresponding with results from Gutknecht et al. (2013). High nitrogen fluxes due to degradation of sinking detritus dominate the Namibian shelf between 18–25°S and south. Nitrogen fluxes from anammox occur in the region from $\sim$ 21–25°S and south. These results indicate that denitrification is the major nitrogen loss pathway in the Benguela OMZ.

4.5 Conclusions

The coupled ROMS–BioEBUS model has been applied in the Benguela upwelling system to understand nitrite dynamics and associated feedback processes. Two regions, one in the ABF region and off Walvis Bay were used to investigate nitrite dynamics in the Benguela. The nitrite maxima develop in the Benguela shelf region and are driven by advection and local physical and biogeochemical processes. Primary nitrite maxima in the ABF and off Walvis Bay are attributed to nitrate assimilation and nitrification. The secondary nitrite maxima occur in the OMZ of the ABF region and are depleted off Walvis Bay. Wind stress conditions in the ABF region result in offshore advection of nitrite maxima formed on the shelf. Nitrite concentrations in the Benguela are also controlled by interplay between nitrification, denitrification and anammox both in and outside the OMZ. Nitrification and denitrification are nitrite sources in the Benguela shelf waters while anammox results in depletion. Coupling between anammox and aerobic processes for nitrite supply appears to exist but no conclusions can be made as some processes are not included in the model.

Nitrous oxide production in the ABF is high when compared to off Walvis Bay. Nitrification is suggested as the dominant nitrous oxide production pathway off Walvis Bay as opposed to accelerated production in suboxic waters. A weak signal of nitrous oxide production through denitrification is suggested in this region. In the ABF, nitrous oxide is driven by nitrification and partly attributed to denitrification under suboxic waters. Nitrous oxide production through a coupling between nitrification and denitrification is also suggested.

Three distinct water masses associated with nitrous oxide have been identified in the ABF region. The nitrous oxide produced from nitrification in deeper water masses is missing off Walvis Bay because of the shallow coastal region. Weak nitrous oxide production in the OMZ off Walvis Bay is attributed to nitrite consumption by anammox.

Interchanges between the nutrient rich, oxygen–depleted SACW and well–oxygenated ESACW in the Benguela shelf waters create unique biogeochemical conditions on the shelf. The interchanges between these currents drive the seasonality of nitrification, anammox and denitrification in the Benguela. The nitrogen feedback processes reported in this study lead to nitrogen loss through different pathways. Nitrification on the shelf results in high N fluxes as compared to anammox and denitrification. There is a need for future studies to incorporate other nutrient cycles to improve understanding on interactions and aid in predicting feedback processes.

5 | Interaction between nitrogen and phosphate, N:P stoichiometry and estimated nitrogen fixation in the Benguela

Abstract

Simulated nitrogen and phosphate uptake rates, N:P stoichiometry and transformation of these cycles under oxic and suboxic conditions are used to understand estimated nitrogen fixation patterns in the Benguela. The coupled NEMO–BFM 1D model is applied in this chapter to understand these processes. Depth–integrated net annual mean nitrogen and phosphate uptake rates are higher at the stations at 21°S than off walvis Bay. Station N1DB01 on the shallow coast shows high nitrogen (0.018 mmol N m^{-2} d^{-1}) but lower phosphate (1.60×10^{-3} mmol P m^{-2} d^{-1}) uptake rates than off Walvis Bay. The nitrogen uptake rates in this study decrease with increasing distance from the coast both at 21°S and off Walvis Bay. In contrast, phosphate uptake rates increase with distance from the coast. The increase in phosphate uptake rates at offshore stations is attributed to an assemblage succession to picophytoplankton. Integrated N:P ratios of 17:1 and 16:1 are shown at stations N1DB01 and N1DB03 at 21°S respectively. Off Walvis Bay low integrated N:P ratios of 13:1 and 12:1 occur at station N1DB02 and N1DB04 respectively. However, both high and low N:P stoichiometry is observed at various depths at 21°S and off Walvis Bay and it is attributed to domination of the nutrient–rich SACW and low nitrate concentrations respectively. Low N* concentrations in surface and subsurface waters are shown at 21°S than off Walvis Bay. The positive N* anomalies off Walvis Bay are attributed to organic matter mineralization in deeper, offshore stations. In contrast, high P* concentrations are exhibited in surface and subsurface waters at 21°S than off Walvis Bay. The increased P* is regenerated in subsurface waters and released in bottom suboxic waters. Phosphate release in suboxic bottom waters is coupled to nitrogen loss and production of hydrogen sulphide. Nitrogen fixation rates estimated from nitrogen and phosphate uptake rates are low at both 21°S and off Walvis Bay. Stations N1DB02 (2.10×10^{-2} mmol N m^{-2} d^{-1}) and N1DB04 (2.62×10^{-2} mmol N m^{-2} d^{-1}) off Walvis Bay. Station N1DB04 show slightly higher depth–integrated nitrogen fixation rates than stations N1DB01 (2.34×10^{-2} mmol N m^{-2} d^{-1}) and N1DB03 (2.50×10^{-3} mmol N m^{-2} d^{-1}) at 21°S. The estimated nitrogen fixation rates in this study are mostly determined by N:P ratios at the stations.

5.1 Introduction

Phosphorus is an essential element in living organisms since it is a macromolecule essential for cellular structure, metabolic and energetic activities. The phosphorus cycle is linked to the carbon and nitrogen cycles through various pathways. Therefore, phosphate availability in the ocean may strongly influence primary productivity and atmospheric carbon dioxide sequestration. Since phosphorus cannot be fixed from the atmosphere, it is often considered to be the limiting macronutrient that controls global marine's primary productivity in the long–term (Tyrrell, 1999). Phosphorus limitation in the ocean has been recognized as more prevalent than previously estimated (Paytan and McLaughlin, 2007). It has been suggested that transitions from nitrogen to phosphorus limitation in the North Pacific subtropical gyre have taken place over the past decades (Karl and Bjorkman, 2001). This transition is linked with the observed succession of prokaryotic picophytoplankton (*Prochlorococcus* and *Synechochocus*) in oligotrophic waters. Residence time of phosphorus in the ocean is longer than that of nitrogen resulting in reduced phosphorus supply rates relative to nitrogen (Paytan and McLaughlin, 2007). North Atlantic deep waters flow through the deep ocean basins to the North Pacific, taking about 1500 years to get there (Benitez-Nelson, 2000; Broecker et al., 1982). Given the longer phosphorus residence time, the older and deep Pacific waters have higher dissolved inorganic phosphorus than the Atlantic (Benitez-Nelson, 2000; Broecker et al., 1982). In the short–term, phosphorus is not considered a limiting nutrient. This is because nitrate is usually depleted faster than phosphate under low nutrient conditions in surface waters (Tyrrell, 1999). Also, it is widely known that the addition of phosphate in oligotrophic waters does not stimulate phytoplankton growth as compared to nitrate (Codispoti, 1989; Ryther and Dunstan, 1971). Although, note that phosphate is considered to be the ultimate limiting nutrient because its rate of supply regulates total ocean productivity, whereas nitrate is considered the proximate limiting nutrient of instantaneous growth (Tyrrell, 1999).

Phosphorus occurs in both particulate and dissolved forms throughout the water column in the ocean (Paytan and McLaughlin, 2007). The dissolved fraction consists of inorganic and organic phosphorus, as well as macromolecular colloidal phosphorus. The particulate phosphorus fraction includes plankton, mineral precipitates, phosphorus adsorbed to particulates and amorphous phosphorus phases. The dissolved inorganic phosphorus, usually in the form of orthophosphate is assimilated by phytoplankton and converted to organic phosphorus (Cotner and Wetzel, 1992). The phytoplankton is eventually ingested

by zooplankton or detritivores and the organic phosphorus excreted as dissolved inorganic and organic phosphorus (Cotner and Biddanda, 2002). Cellular dissolved inorganic and organic phosphorus are also released into seawater through phytoplankton cell lysis (Anderson and Zeutschel, 1970). The inorganic phosphorus is rapidly assimilated by phytoplankton, continuing the cycle. Through enzymes synthesized by bacteria some of the organic phosphorus can be hydrolyzed and subsequently assimilated by phytoplankton (Cotner and Biddanda, 2002). Dissolved inorganic and organic phosphorus also alternate between the dissolved and particulate fractions as they are absorbed and desorbed from sinking particulate matter in the water column (Delaney, 1998; Faul et al., 2005). These transformations and cycling predominantly occur in the upper water column (Paytan and McLaughlin, 2007). However, all of these processes also occur at depth, throughout the water column, with the exception of phytoplankton assimilation (Faul et al., 2005).

Dissolved organic phosphorus hydrolysis and conversion back to dissolved inorganic form is mostly performed by heterotrophic bacteria. However, in cases where phosphorus demand is not fulfilled by inorganic orthophosphate, phytoplankton and autotrophic bacteria also have the ability to hydrolyze organic phosphorus to match the demand (Cotner and Biddanda, 2002; Paytan and McLaughlin, 2007; Cotner and Wetzel, 1992). Most of the dissolved inorganic phosphorus uptake is in the euphotic zone where marine photosynthesis takes place. However, conversion of organic phosphorus by hydrolysis to dissolved inorganic phosphorus occurs throughout the water column. An increase in dissolved inorganic phosphorus is also observed within deep waters as a result of water aging due to continuous sinking particulate matter accumulation and its regeneration (Paytan and McLaughlin, 2007). For example, the deep Pacific waters are older and have higher dissolved inorganic phosphorus than the Atlantic (Benitez-Nelson, 2000; Broecker et al., 1982).

In contrast, the dissolved organic phosphate depth distribution in the ocean follows a different trend. High concentrations of organic phosphorus are observed in the ocean surface where there is an abundance of marine life which synthesizes these organic compounds (Aminot and Kérouel, 2004; Clark et al., 1999; Karl and Bjorkman, 2001). The concentration of dissolved organic phosphorus in the ocean is typically lower at depth because much of it is hydrolyzed into dissolved inorganic phosphorus within the surface layer, resulting in transfer of only a small fraction to the deep ocean (Paytan and McLaughlin, 2007). Depth dissolved organic phosphorus concentrations are similar in all oceanic basins, suggesting

long residence time for the majority of the dissolved organic phosphorus pool (Kolowith et al., 2001). The phosphorus in dissolved organic matter is usually depleted in the upper water column comparative to Redfield ratios of C:N:P = 106:16:1 (Paytan and McLaughlin, 2007; Redfield et al., 1963). But an increase in C:P and N:P ratios with depth is observed, indicating that phosphorus is preferentially regenerated from dissolved organic matter.

This literature review highlights the different phosphate forms and their transformation within the water column. A single phosphate species, orthophosphate is considered in the BFM. Therefore, this chapter focuses on the transformation of orthophosphate under oxic and suboxic conditions. The implications of nitrogen loss on phosphorus cycling is also investigated. The biological uptake and remineralization of phosphate and nitrate in the ocean is assumed to occur at a constant Redfield ratio of 16:1. In the presence of nitrogen fixation, the Redfield ratios is violated because nitrogen fixers preferentially consume phosphate over nitrate (Deutsch et al., 2004). This causes phosphate depletion in surface waters drawing nutrient concentrations to below the Redfield ratio. The ratio of sinking particulate organic N:P is also less than the ratio of dissolved N:P as a result of denitrification. Therefore, the BFM model is applied in this chapter to understand local interactions between the phosphorus and nitrogen cycle and N:P stoichiometry in the Benguela. The uptake rates from BFM and N:P ratios are then used to estimate nitrogen fixation in the Benguela.

5.2 Materials and methods

The simulated nitrogen and phosphate concentrations, uptake rates, N:P stoichiometry and phytoplankton concentrations from BFM are discussed in this chapter. The simulated concentrations are combined with biogeochemical methods to understand implications of N* and P* deviations in nitrogen fixation. Data from the CARS climatology is also used to validate the N:P stoichiometry and evaluate implications of the biases reported earlier.
Nitrogen deviations from the Redfield ratio are calculated using a N* tracer, defined as a linear combination of nitrate and phosphate (Gruber and Sarmiento, 1997). The N* tracer is important in investigating the distribution of nitrogen fixation and denitrification in the ocean. N* concentrations to the left and right of the Redfield ratio indicate negative and positive anomalies respectively. The N* tracer is calculated using the method of Deutsch et al. (2007) as:

$$\mathrm{N^*} = (\mathrm{NO_3^-} - 16 \cdot \mathrm{PO_4^{3-}} + 2.9) \cdot 0.87 \tag{5.1}$$

Simulated nitrate and phosphate concentrations from this study are used in the equation. The constant (-2.9 mmol N m^{-3}) drives the global mean of N* to zero. The depletion of phosphate relative to nitrate requirement is calculated using a P* tracer (Deutsch et al., 2007). P* is an important measure of phosphate in relation to the standard nitrogen quota and can be used to determine nitrogen fixation. Nitrogen fixing organisms consume phosphate while conserving nitrogen resulting in lower P* compared to N* in the water column. P* is calculated as:

$$\mathrm{P^*} = [\mathrm{PO_4^{3-}}] - [\mathrm{NO_3^-}]/16 \tag{5.2}$$

The simulated nitrogen and phosphate uptake rates, N:P ratios, P* concentrations and nutrient concentrations can be used to estimate nitrogen fixation rates and patterns in the Benguela. Nitrogen fixation is estimated from nitrogen and phosphate uptake rates following the assumption of Deutsch et al. (2007):

$$J_{\mathrm{fix}}(\mathrm{N}) = r_{\mathrm{f}}(J_{\mathrm{up}}(\mathrm{P}) - \frac{J_{\mathrm{up}}(\mathrm{N})}{r_{\mathrm{n}}}) \tag{5.3}$$

Where r_{n} is the Redfield ratio and r_{f} is the ratio of nitrogen fixers assumed to be N:P$= 50 : 1$.

5.3 Results and discussion

Phosphate concentrations were generally depleted in surface waters and accumulated at depth during the MSM 19/1b cruise (Figure 5.1). In shallow, inshore stations phosphate concentrations ranged between 2–2.25 mmol P m^{-3} at 200–600 m depths. Station 1031 exhibited particularly high phosphate concentrations around 100 m. Offshore, deeper stations exhibited low phosphate concentrations (<1.5 mmol P m^{-3}) at 0–200 m. High

phosphate concentrations occurred between 200–1000 m at these stations. Phosphate at station 1029 (N1DB01) ranged from 1.62–1.95 mmol P m^{-3} corresponding with simulated concentrations (1.08–2.38 mmol P m^{-3}). Station 1035 (N1DB03) observed (0.90–2.43 mmol P $^{-3}$) and simulated (0.71–2.57 mmol P m^{-3}) phosphate concentrations were also within the same range. Off Walvis Bay, station 1042 (N1DB04) and 1043 (N1DB02) exhibited low phosphate concentrations when compared to the northern stations. Observed phosphate at station 1042 (0.69–2.10 mmol P m^{-3}) and 1043 (0.72–2.06 mmol P m^{-3}) also corresponded with simulated concentrations of 0.38–2.52 and 0.39–2.56 m mol P m^{-3} respectively. Vertical distribution of phosphate in the model corresponds with the MSM 19/1b data as described in Section 3.3.2. High phosphate concentrations occur under low oxygen concentrations and accumulate on the shallow shelf both in the model and MSM 19/1b data. Off Walvis Bay, station N1DB02 and N1DB04 in the model also exhibit low phosphate concentrations at depth than other stations. This is in correspondence with the MSM 19/1b data at station 1039–1044 off Walvis Bay. High phosphate concentrations off walvis Bay accumulate on the continental shelf slope.

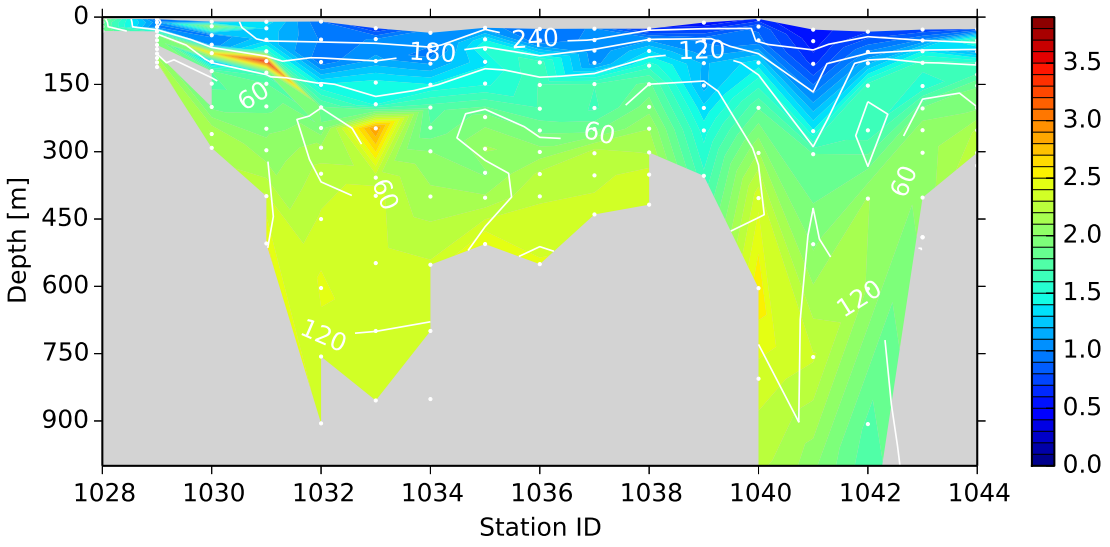

Figure 5.1: Section of phosphate concentrations [mmol P m^{-3}] off Namibia. The vertical dotted white lines define the CTD casts where phosphate samples for measurements were taken during the MSM 19/1b cruise. White contours indicate oxygen concentrations [mmol O_2 m^{-3}].

5.3.1 Nitrogen and phosphate uptake rates

Simulated net nitrogen uptake rates are presented in figure 5.2a–d. The nitrogen uptake rates followed a similar profile and seasonal trend at depth in all stations. The spikes in the figure are daily fluctuations of nitrogen uptake at depth at the stations. Two distinct regions of increased nitrogen uptake were observed in surface (0–20 m) and subsurface (20–80 m) waters. Increased nitrogen uptake occurs during spring and early summer in both surface and subsurface waters. The high uptake rates occur in surface waters from September to December in all stations. In subsurface waters, nitrogen uptake increases during October and reaches a peak in November. Throughout summer and autumn, the uptake rates in subsurface waters remain nearly constant. The stations exhibit low nitrogen uptake rates during winter. The shallow station (N1DB01) shows higher nitrogen uptake rates than other stations. Off Walvis Bay, station N1DB04 shows high nitrogen uptake rates in surface waters during spring. Nitrogen uptake at the stations decreases below 100 m.

Maximum nitrogen uptake rates at the stations ranged from 0.033 to 0.049 mmol N m^{-3} d^{-1}. The maximum nitrogen uptake rates (0.049 mmol N m^{-3} d^{-1}) occurred in surface waters of station N1DB04 off Walvis Bay. Annual mean nitrogen uptake rates are 0.018 and 0.017 mmol N m^{-2} d^{-1} for station N1DB01 and N1DB03 respectively. Off Walvis Bay, the annual mean uptake rates were 0.015 and 0.017 mmol N m^{-2} d^{-1} for station N1DB02 and N1DB04 respectively. These results indicate that higher nitrogen uptake rates occur at the stations located at 21°S than off Walvis Bay. Size–fractionated biomass–specific nitrate uptake rates off Costa Rica, in the Humboldt current and Peru upwelling system were averaged at 0.42, 0.18 and 0.30 mmol ρNO_3^- m^{-3} d^{-1} respectively. Off California, nitrate uptake rates have been reported to range between 1.15–3.40 mmol ρNO_3^- m^{-3} d^{-1} in the Monterey Bay (Franck et al., 2005). Simulated nitrogen uptake rates in this study appear to have been underestimated compared to these studies. The simulated nitrogen uptake rates decrease with distance from the coast both at 21°S and off Walvis Bay. This is attributed to luxury uptake of nitrogen in nutrient–rich coastal stations than offshore. The nutrient–rich SACW also dominate at 21°S hence nitrogen uptake rates in this region are higher than off Walvis Bay.

Simulated net phosphate uptake rates at the stations followed a similar profile to nitrogen

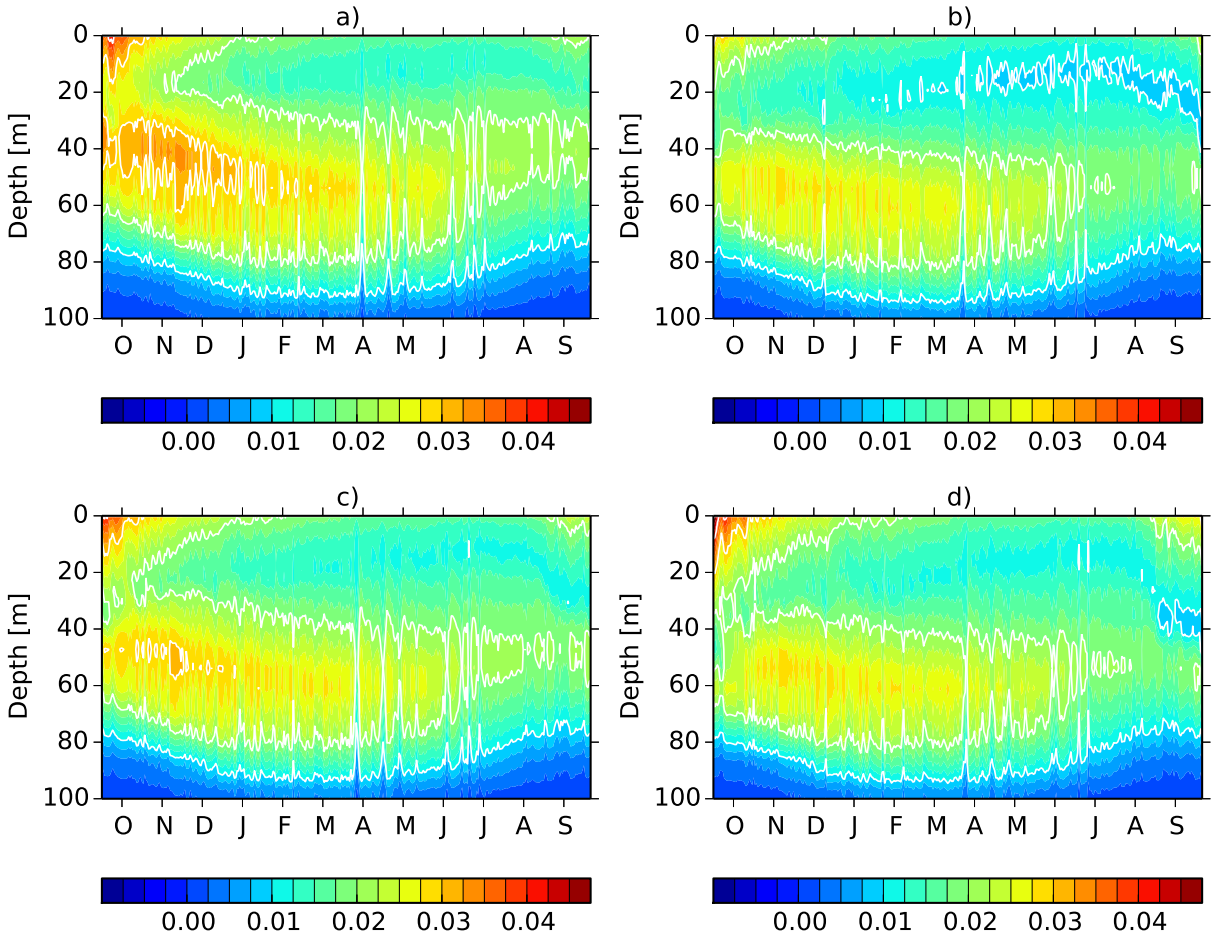

Figure 5.2: Simulated net nitrogen uptake rates [mmol N m^{-3} d^{-1}] for station (a) N1DB01, (b) N1DB02, (c) N1DB03 and (d) N1DB04.

(Figure 5.3a–d). A similar seasonal trend to nitrogen is also shown with phosphate uptake rates. However, the depth of increased phosphate uptake in subsurface waters is shallower. Phosphate uptake rates in subsurface waters also remain nearly constant throughout spring to autumn and decrease during winter. In contrast to nitrogen, simulated phosphate uptake rates at the stations appear to be lower. The uptake rates at the stations do not exceed 6×10^{-3} mmol P m^{-3} d^{-1}. Below 100 m, phosphate uptake also decreases significantly. Station N1DB04 showed high phosphate uptake rates in surface waters during spring to early summer.

Simulated net phosphate uptake rates increase with distance from the coast at station N1DB02–4. Maximum phosphate uptake rates at the stations range between 3.63–

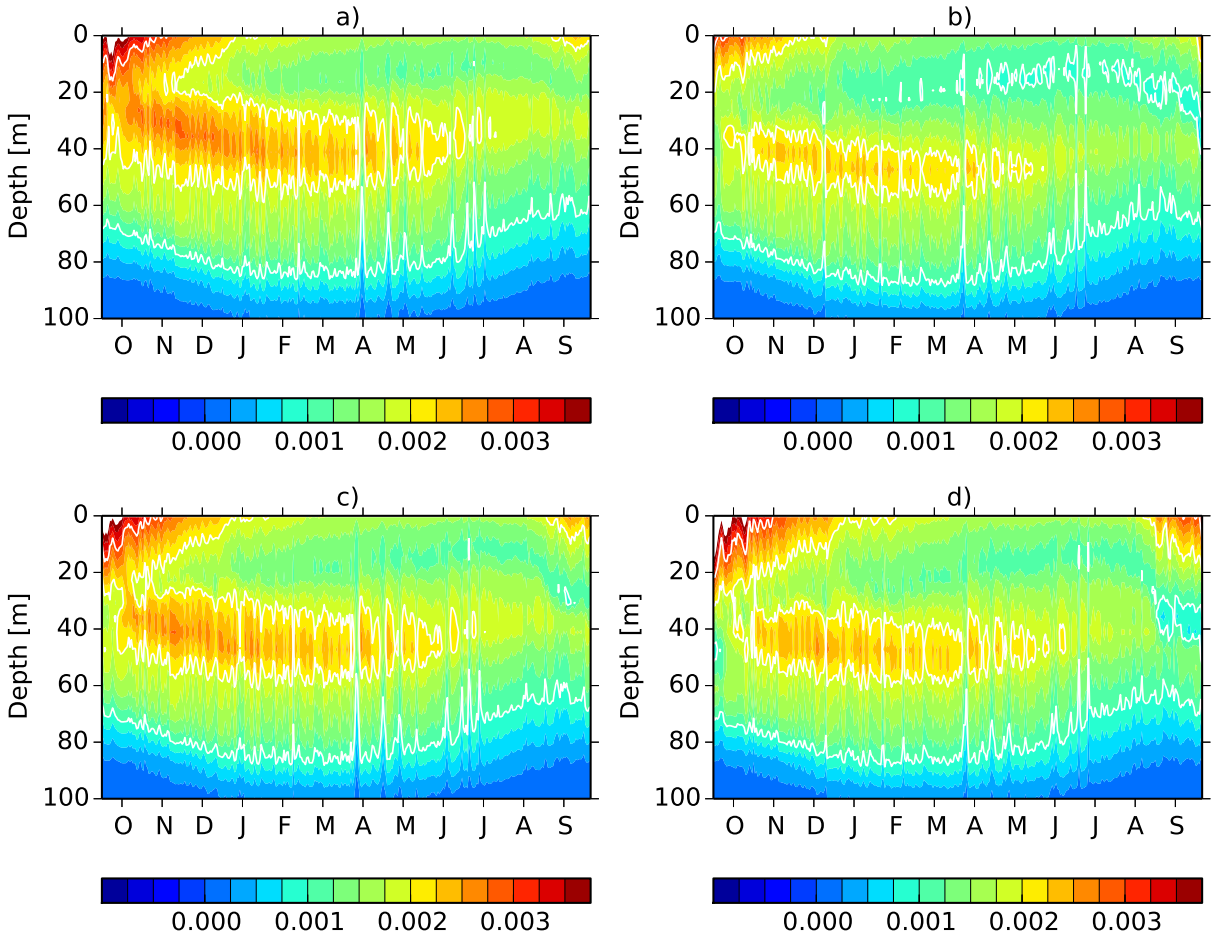

Figure 5.3: Simulated phosphate uptake rates [mmol P m^{-3} d^{-1}] for station (a) N1DB01, (b) N1DB02, (c) N1DB03 and (d) N1DB04.

5.45×10^{-3} mmol P m^{-3} d^{-1}. Annual mean phosphate uptake rates are lower at station N1DB02–3 than the offshore station (N1DB04) off Walvis Bay. The annual mean phosphate uptake rates at station N1DB01 are higher (1.60×10^{-3} mmol P m^{-2} d^{-1}) than at other stations. Annual mean phosphate uptake rates were 1.56×10^{-3} mmol P m^{-2} d^{-1} for station N1DB03. Phosphate uptake rates of 1.32×10^{-3} and 1.57×10^{-3} mmol P m^{-2} d^{-1} occurred at station N1DB02 and N1DB04 respectively. The increased uptake rates at stations N1DB03 and N1DB04 than N1DB02 can be attributed to competitive phytoplankton growth at offshore stations (Table 5.1). Phytoplankton concentrations at these stations differ slightly for diatoms, nanoflagellates and picophytoplankton. Growth of nanoflagellates and picophytoplankton at the offshore station (N1DB04) was slightly higher than at the shallow coastal station (N1DB01). This can be be partly attributed to succession of

picophytoplankton in oligotrophic stations. This succession has been linked to phosphorus limitation in the North Pacific subtropical gyre (Karl and Bjorkman, 2001).

Nausch and Nausch (2014) reported that phosphate uptake rates ranged between 5.28×10^{-3} and 1.46×10^{-1} μM d^{-1} during winter. The phosphate uptake rates in the above–mentioned study increased with distance from the coast to 110 km then decreased, consistent with findings in this study. The simulated phosphate uptake rates in this study are within range of these observations. However low the uptake rates, phosphate is not considered a limiting nutrient in the Benguela upwelling system. Addition of phosphate (2 μM) in experimental tanks of water samples obtained off northern Namibia (20–21°S) stimulated further growth of diatoms, indicating luxury uptake of phosphate (Wasmund et al., 2014). Despite the stimulation of uptake rates by diatoms after phosphate addition, the study concluded that phosphate was not a limiting nutrient in comparison with nitrogen due to early exhaustion of nitrate in the experiments.

Table 5.1: Depth–integrated annual mean concentrations [10^{-3} mmol P m^{-2}] of diatoms, nanoflagellates, picophytoplankton and large phytoplankton at the stations. The annual mean concentrations are integrated over the upper 100 m.

Station	Diatoms	Nanoflagellates	Picophytoplankton	Large phytoplankton
N1DB01	6.11	4.70	4.20	0.00025
N1DB02	3.71	5.05	4.03	0.03182
N1DB03	4.90	4.71	4.10	0.00055
N1DB04	4.45	4.77	4.14	0.00095

A previous study determined nutrient uptake rates through Redfield ratios in experimental tanks and reported higher nitrogen than phosphate uptake leading to nitrate exhaustion (Wasmund et al., 2014). Nitrogen uptake rates in this study are higher than phosphate corresponding with findings in these observations. Simulated phytoplankton concentrations at the stations varies with distance from the coast (Table 5.1). A strong phosphate uptake by diatoms is shown at station N1DB01 and N1DB03 at 21° than off Walvis Bay. Off Walvis Bay, station N1DB02 and N1DB04 show high phosphate uptake by nanoflagellates and picophytoplankton. Large phytoplankton contribute less to the phosphate uptake

at all stations. The increased phosphate uptake at station N1DB01 by diatoms can be attributed to high primary production on the shallow coast. A previous study found that phytoplankton contributed 72% on average to phosphate uptake in the Benguela (Nausch and Nausch, 2014). Picoplankton in the above–mentioned study accounted for 91.2% of the total phosphate uptake.

5.3.2 Nitrate and phosphate stoichiometry

Nitrate and phosphate stoichiometry in comparison with the classic Redfield ratio in the Benguela is investigated. The scatter plot of simulated N:P ratios is presented in figure 5.4. Station N1DB01 showed low N:P ratios at 0–100 m (not shown). Below 150 m, N:P ratios increase in suboxic waters of station N1DB01. Station N1DB03 exhibited N:P stoichimetry close to the Redfield ratio in the top 100 m and high ratios at 200–300 m. Similar to station N1DB01, low N:P ratios occurred in suboxic waters of station N1DB03. Station N1DB02 and N1DB04 followed a similar profile of high N:P ratios at 0–250 m and 0–400 m respectively. Low N:P ratios occur in suboxic waters below 300 m at station N1DB02. A signal of low N:P waters at 400–600 m and below 600 m is observed at station N1DB04. The N:P ratios follow a latitudinal pattern. At 21°S, integrated N:P ratios at stations N1DB01 (17:1, R^2 = 0.97, n = 33) and N1DB03 (16:1, R^2 = 0.97, n = 39) were similar to the Redfield ratio. Off Walvis Bay, station N1DB02 (13:1, R^2 = 0.93, n = 39) and N1DB04 (12:1, R^2 = 0.95, n = 52) exhibited low N:P ratios. In comparison with the CARS climatology, station N1DB01 (CARS: 18:1, R^2 = 0.96, n = 33) and N1DB03 (CARS: 17:1, R^2 = 0.98, n = 39) N:P ratios were slightly lower. Station N1DB02 (CARS: 16:1, R^2 = 0.98, n = 39) and N1DB04 (CARS: 17:1, R^2 = 0.98, n = 52) ratios appear to have been underestimated due to simulated autumn–winter nitrate bias and phosphate overestimation off Walvis. The nitrate and phosphate biases as discussed earlier did not significantly impact on the N:P ratios at stations N1DB01 and N1DB03 at 21°S. The Redfield ratios off Walvis Bay deviate from the CARS climatology.

Nitrate and phosphate stoichiometry less than or above the Redfield ratio is assumed to indicate nitrate and phosphate limitation respectively. The simulated N:P concentrations in the Benguela scatter to both sides of the reference Redfield ratio. A previous study also reported similar nitrate and phosphate concentrations that scattered to both sides of the Redfield ratio (Flohr et al., 2014). The simulated N:P ratios at 21°S (N1DB01 and N1DB03) are both equal to and above the Redfield ratio. Off Walvis Bay, the stations

(N1DB02 and N1DB04) showed nitrate concentrations below the Redfield ratio at deeper depths. The N:P ratios above and close to Redfield at 21°S can be attributed to the dominance of the nutrient rich, oxygen–depleted SACW and remineralization in the deeper station (N1DB03). The N:P ratios off the Benguela shelf have been reported to be restored to the Redfield stoichiometry corresponding with this study (Flohr et al., 2014). The effect of the well–oxygenated SACW is also observed at station N1DB02 and N1DB04 off Walvis Bay. Low N:P ratios in the Benguela were reported by Tyrrell and Lucas (2002) and were attributed to denitrification and phosphate accumulation. Hence the implications of denitrification on phosphate release are explored in subsequent sections. Due to both low and high N:P ratios, the Benguela is regarded as a system that produces both positive and negative deviations from the Redfield ratio (Flohr et al., 2014).

The N* concentrations off Walvis Bay and at 21°S from the model and CARS climatology are presented in figures 5.5a and c. The model captured the N* concentrations observed in the CARS data. The N* profiles at the stations showed low concentrations at the surface, increased at mid–depths and decreased in bottom waters except for station N1DB01 (figure 5.5a). A latitudinal difference in N* profiles is observed between the stations. Station N1DB01 and N1DB03 at 21°S showed low N* concentrations in surface waters than off Walvis Bay. Additionally, station N1DB01 also exhibited lowest N* concentrations (~ -1.39 mmol N m^{-3}) around 150 m than other stations. In contrast to station N1DB01, N1DB03 showed high N* concentrations at the same depth. Off Walvis Bay, stations N1DB02 and N1DB04 exhibited high N* concentrations in surface and subsurface waters. The N* concentrations at station N1DB02 and N1DB04 ranged between 7–10 mmol N m^{-3} at 0–100 m depths. Below 100m, positive N* concentrations (0–10 mmol N $^{-3}$) were observed at the stations except for station N1DB01. Negative N* concentrations are associated with low oxygen at station N1DB01 (100–200 m), N1DB02 (300–400 m) and N1DB03 (300–400 m). Positive N* concentrations in subsurface waters are commonly attributed to nitrogen fixation (Gruber and Sarmiento, 1997). Previous studies reported both positive and negative N* concentrations in suboxic and bottom waters off the coast of Namibia (Flohr et al., 2014; Kuypers et al., 2005). N* concentrations in Flohr et al. (2014) were generally positive in the location of station N1DB04 off Walvis Bay corresponding with this study. Similarly, positive and negative N* concentrations in the above–mentioned study were observed in surface and bottom suboxic waters in the region of station N1DB02 respectively. Pronounced negative

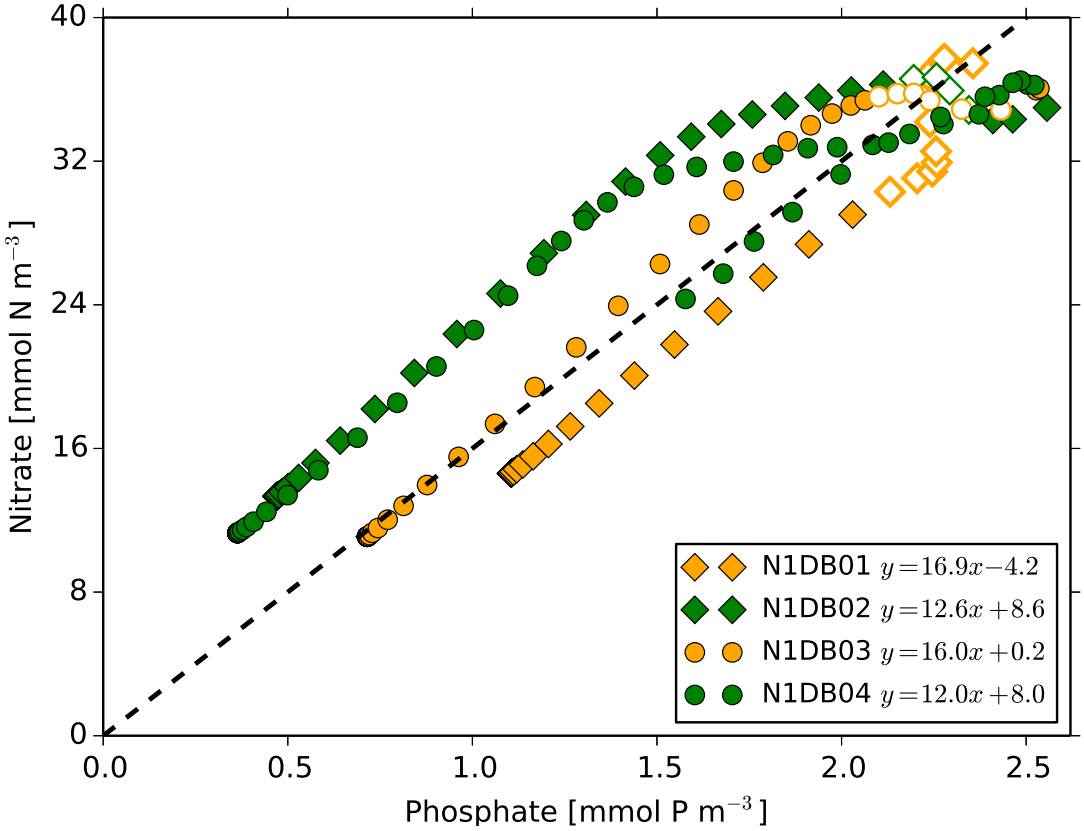

Figure 5.4: Scatter plot of simulated, annual mean nitrate versus phosphate concentrations at the stations. Orange and green markers represent stations at 21°S (N1DB01 and N1DB03) and off Walvis Bay (N1DB02 and N1DB04) respectively. Open markers show nitrate and phosphate concentrations in the OMZ. The dashed line show the Redfield ratio of N:P = 16:1. Station best fits are determined by least squares regression.

N* concentrations have been reported in coastal bottom waters in the region of station N1DB01 (Tyrrell and Lucas, 2002). Flohr et al. (2014) suggested that variability in nutrient ratios of the SACW control the inter–annual variability of N* concentrations in the northern Benguela. The ESACW is assumed to contribute to low N* concentrations in the region due to the absence of nitrogen fixation in the southern Benguela.

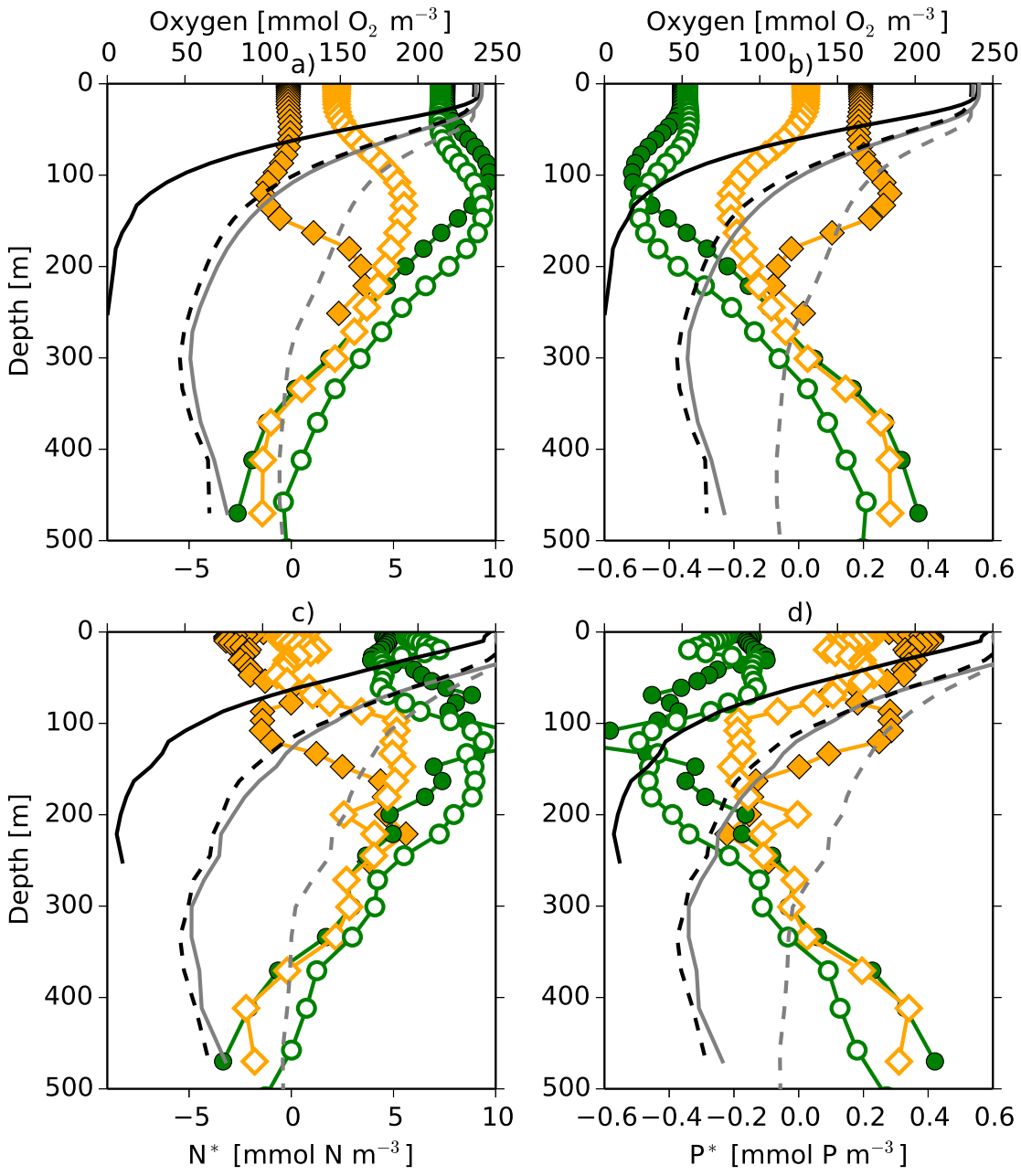

Figure 5.5: Annual mean N*, P* and dissolved oxygen concentrations at the stations for the model (top panel) and CARS October data (bottom panel). Orange and green markers represent stations at 21°S (N1DB01–closed and N1DB03–open) and off Walvis Bay (N1DB02–closed and N1B04–open) respectively. Black solid (N1DB01) and dashed (N1DB03) lines represent oxygen concentrations for stations at 21°S. The gray solid (N1DB02) and dashed (N1DB04) lines represent oxygen concentrations for stations off Walvis Bay.

P* concentrations from the model and CARS data in the Benguela follow a different profile to N* (Figure 5.5b). High P* concentrations were shown at 21°S than off Walvis Bay. Positive P* concentrations occurred throughout the water depth at station N1DB01. Maximum P* concentrations (0.28 mmol P m^{-3}) at this station occurred around 150 m. Simulated negative P* concentrations occurred at 0–300 m at stations N1DB02, N1DB03 and N1DB04. For station N1DB03, this is in contrast to the CARS data which showed positive P* concentrations at 0–100 m. Below 300 m positive P* concentrations were shown at these stations. The low P* concentrations in surface waters at the stations can be attributed to phosphate uptake. Phosphate in the ocean is usually depleted in surface waters because of biological uptake and increase at depth as a result of regeneration (Paytan and McLaughlin, 2007). The strong simulated P* peak at station N1DB01 appears to be limited to the shallow coast. This peak is not observed at stations N1DB02–4 and has been linked to spatio–temporal variability of phosphate controlled by interplay between physical and biological processes in coastal waters (Ruttenberg and Dyhrman, 2005). Flohr et al. (2014) calculated excess P* of 0.3 ± 0.01 μmol kg^{-1} within the 0–20 m depth off Walvis Bay. This excess P* was exported offshore suggesting that the northern Benguela is a source of phosphate to the south Atlantic. Results from this study showed similar P* concentrations at stations N1DB04 and N1DB02 at the reported depths despite a ∼77 km distance. This supports findings that the Benguela is a source of P* to the South Atlantic.

The simulated low P* concentrations in surface waters of station N1DB02, N1DB03 and N1DB04 also indicate that phosphate is removed from the surface and accumulates in bottom waters. This results in increased N* in surface waters of these stations since phosphate occurs at lower concentrations relative to nitrate. In contrast, increased nitrate consumption occurs at station N1DB01 resulting in low N* concentrations at 0–200 m. P* concentrations increase at this depth as nitrate is consumed at a higher rate than phosphate. Below 200 m, nitrate is remineralized at station N1DB01 increasing the N* concentrations relative to P*. The high P* concentrations below 300 m at station N1DB02, N1BD03 and N1DB04 can be attributed to phosphate exported with organic matter and regeneration at deeper depths (Paytan and McLaughlin, 2007). At station N1DB01, pronounced negative N* concentrations and high P* concentrations can be attributed to high denitrification rates under low oxygen conditions (Figure 5.6a–b). Phosphate is released at a high rate under low oxygen (< 50 μM) and low organic matter oxidation (< 1 mmol m^{-2} d^{-1}) (McManus et al., 1997). Under these conditions at station N1DB01, phosphate may be released at

a higher rate than through regeneration from oxidation of organic matter as observed at bottom depths of station N1DB02, N1DB03 and N1DB04. Phosphate release under high oxygen bottom waters and organic matter decomposition ($\sim$ 7 mmol m^{-2} d^{-1}) are similar to rates expected from decomposition of organic debris (Berelson et al., 2003; McManus et al., 1997). The bottom waters off Walvis Bay are dominated by high P* and reduced N* concentrations (Flohr et al., 2014). Results from this study correspond with observations from Flohr et al. (2014) that the Namibian shelf is a region of P* generation via nitrogen loss (denitrification and anammox) and phosphate efflux.

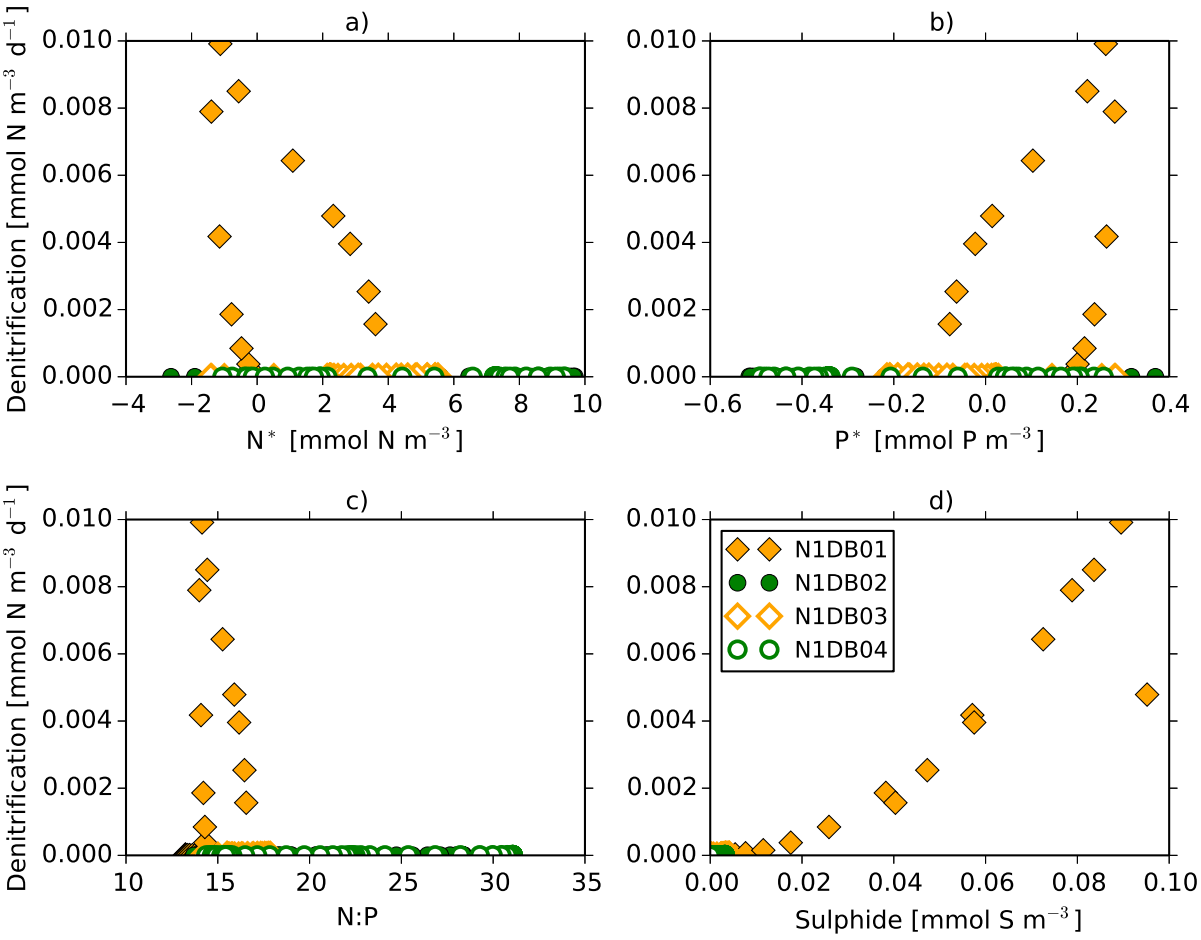

Figure 5.6: Annual mean simulated denitrification rates versus (a) N*, (b) P*, (c) N:P ratios and (d) sulphide production for the stations.

Simulated denitrification rates off Walvis Bay and at 21°S are presented in figure 5.6. The annual mean denitrification rates at 21°S were 1.614 and 0.010×10^{-3} mmol N m^{-2} d^{-1} for station N1DB01 and N1DB03 respectively. Off Walvis Bay, the denitrification rates were 0.007×10^{-3} and 0.003×10^{-3} mmol N m^{-2} d^{-1} for station N1DB02 and N1DB04 respectively. Maximum denitrification rates at station N1DB01 are within range of the BioEBUS model (Table 4.1). The high denitrification rates at station N1DB01 lead to low N* concentrations and P* concentrations as discussed earlier. The high denitrification rates drive the N:P ratios to below the Redfield ratio under suboxic and anoxic conditions (Figure 5.6c). Sulphide production increased to 0.09 mmol S m^{-3} under maximum denitrification rates at station N1DB01 (Figure 5.6d). Sulphide concentrations at other stations were below 0.004 mmol S m^{-3}.

Sulphide flux into the suboxic zone off the Namibian coast (24°S) has been reported to occur at a rate of $\sim$ 2.3 mmol m^{-2} d^{-1} (Lavik et al., 2009). The above–mentioned study also reported an overlap between nitrate and sulphide at 86–90 m with denitrification as the main nitrogen loss mechanism. Results from this study suggest that sulphide production under suboxic and anoxic conditions enhances denitrification as formulated in the BFM model. Nitrate is used up as an electron acceptor during this process leading to its depletion. Low N* concentrations occur under these conditions as observed at station N1DB01. This further suggests that denitrification and sulphide production under suboxic and anoxic conditions are coupled to phosphate release. Nitrogen loss under these conditions appears to not impact negatively on phosphate concentrations. The nitrogen loss through denitrification is favorable for phosphate release in the Benguela shelf waters.

5.3.3 Nitrogen fixation

Simulated nitrogen and phosphate uptake rates were used to estimate nitrogen fixation at the stations using the fundamental assumption of Deutsch et al. (2007) as described in equation 5.3. The estimated nitrogen fixation patterns integrated over the top 100 m are suggested in figures 5.7a–d. Station N1DB01 and N1DB03 21°S followed nitrogen fixation pattern that are different to the stations at 21°S. At 21°S station N1DB01 and N1DB03 exhibited annual mean nitrogen fixation rates of 2.34×10^{-2} and 2.50×10^{-2} mmol N m^{-2} d^{-1} respectively. Increased P* supply is shown at station N1DB01 due to release under suboxic conditions as discussed earlier. At station N1DB03 nutrient supply is close to

Redfield ratios as reported in section 5.3.2. It is suggested that in addition to phosphate release under suboxic conditions, the excess P* at station N1DB01 is not taken up due to low nitrogen fixation rates. The low nitrogen fixation and phosphate uptake rates are assumed to result in excess P* concentrations at station N1DB01 (0.13–0.87 mmol P m^{-3}) and N1DB03 (-0.20 to 0.01 mmol P m^{-3}). In regions where increased phosphate supply occurs due to physical and biological processes, increased phosphate uptake is required to bring concentrations back to Redfield ratios Deutsch et al. (2007). The excess P* that is not taken up at these stations is assumed to contribute to the fraction exported offshore.

Station N1DB02 and N1DB04 off Walvis Bay exhibited slightly lower and higher estimated nitrogen fixation rates than the stations at 21°S respectively. Stations N1DB02 and N1DB04 exhibited annual mean nitrogen fixation rates of 2.10×10^{-2} and 2.62×10^{-2} mmol N m^{-2} d^{-1} respectively. These stations are characterized by nutrient supply below the Redfield ratio. This has a potential to stimulate estimated nitrogen fixation and potentially increase integrated phosphate uptake rates for station N1DB02 and N1DB04. Low nitrate concentrations also occurred at station N1DB04 since its located further offshore. Nitrogen fixation is linked to nitrogen–deficit waters in high denitrification zones indicating that this process is stimulated to restore the nitrogen inventory (Deutsch et al., 2007). Estimated nitrogen fixation and the increased phosphate uptake rates from picophytoplankton can result in negative P* concentrations as shown at station N1DBO2 (-0.54 to -0.36 mmol P m^{-2}) and N1DB04 (-0.47 to -0.34 mmol P m^{-2}). The depletion of phosphate coupled with relatively low nitrogen fixation rates draw the N:P ratio to below the Redfield ratio (Deutsch et al., 2007). This is suggested in surface waters of station N1DB02 and N1DB04 off Walvis Bay. Since these stations are located further offshore, reduced phosphate supply also contributes to the negative P* concentrations.

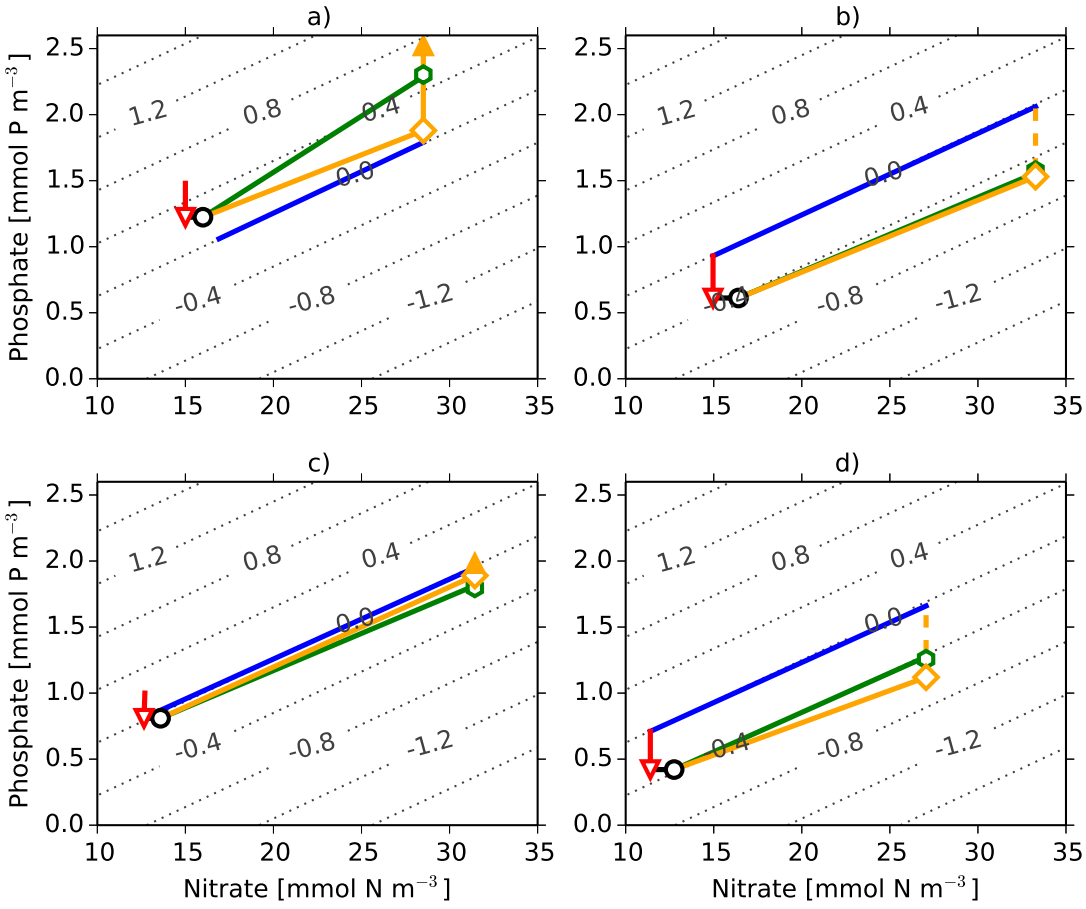

Figure 5.7: Simulated phosphate versus nitrate concentrations at stations (a) N1DB01, (b) N1DB02, (c) N1DB03 and (d) N1DB04. The blue lines show the reference Redfield ratio. Black lines and circles represent estimated annual mean nitrogen fixation rates [mmol N m^{-2} d^{-1}] and nutrient concentrations respectively. Green lines and markers show nutrient supply and maximum nitrate and phosphate concentrations from physical processes respectively. Background contour lines show P* concentrations [mmol P m^{-3}]. The orange lines show minimum (diamond) and maximum (arrow) P* concentrations. Dashed lines indicate a P* deficit.

Average nitrogen fixation rates of -0.010±0.136 μmol m^{-2} h^{-1} and -0.049 μmol m^{-2} h^{-1} were calculated from incubations and station data (integrated over the upper 40 m) off northern Namibia respectively (Wasmund et al., 2015). No specific depth distribution pattern of nitrogen fixation was found in the above–mentioned study. The nitrogen fixation rates calculated in this study correspond with these estimations. In addition, the estimated nitrogen fixation rates in this study decreased with depth and are centered around zero below $\sim$ 80 m for station N1DB01 and N1DB02 (not shown). Nitrogen fixation depth increased to $\sim$ 50 m at stations N1DB03 and N1DB04 respectively. This suggests that the estimated nitrogen fixation rate depth in the Benguela increases with distance from the coast. Rapid production and degradation of dissolved organic phosphate in highly productive regions has been found to reduce phosphate uptake and enhancing it in the adjacent oligotrophic regions (Deutsch et al., 2007). This implies that nitrogen fixation is shifted from upwelling regions into the adjacent subtropical gyres. Results from this study agree with these findings since the estimated nitrogen fixation rates and depths increase with distance from the coast. Estimated nitrogen fixation rates (23–72 mmol N m^{-3}) in the Atlantic have been reported to be lower than in the subtropical Pacific ocean (Deutsch et al., 2007; Gruber and Sarmiento, 1997; Hansell et al., 2004). The Atlantic ocean is estimated to contribute 15% or less to the global nitrogen input through nitrogen fixation (Deutsch et al., 2007).

Nitrogen fixation in the ocean follows the distribution of the best–studied and perhaps the dominant *Trichodesmium* species which thrive in warm oligotrophic waters (Deutsch et al., 2007). Wasmund et al. (2015) reported the absence of *Trichodesmium* and abundance of picocyanobacteria from microscopic analyses of nitrogen fixers off the coast of Namibia and Angola. Despite the abundance of picocyanobacteria (*Prochlorococcus* and *Synechococcus*) coupled with improvement of conditions such as a warmer temperature, addition of phosphate and iron, nitrogen fixation was not induced during experiments performed in the above–mentioned study. The unicellular cyanobacterium UCYN-A was also found to be abundant in cooler waters and at a depth of 40–110 m Wasmund et al. (2015). Abundance of UCYN–A was negligible in the upper 20 m leading to low nitrogen fixation rates. The absence of *Trichodesmium* species contributed more significantly to the low nitrogen fixation in the study. In addition to ineffective picocyanobacteria, unfavorable conditions such as temperature could be limiting for nitrogen fixation to occur in the Benguela. Nitrogen fixation is widely known to be limited by low temperatures (below 20°C) and a shortage of

trace metals such as iron (Berman-Frank et al., 2007)

In agreement with this study, nitrogen fixation rates have been found to depend greatly on nutrient ratios (Deutsch et al., 2007). Deutsch et al. (2007) also suggested that N* deficit waters generated in suboxic zones of the Pacific and Indian oceans provide a stimulus for nitrogen fixation when transported to the surface. Similarly, estimated nitrogen fixation rates from this study are slightly higher in surface, low N* waters off Walvis Bay than at 21°S. This suggests that the N* deficit creates a negative feedback which should be countered by an increase in nitrogen fixation to restore Redfield ratios. Iron is not considered a limiting factor for nitrogen fixation in the Benguela. Iron supply is higher in the Atlantic than the Pacific but nitrogen fixation rates are still low (Mahowald et al., 1999). This points to a combination of processes, as mentioned, that limit nitrogen fixation in the Benguela.

5.4 Conclusions

The coupled physical–biogeochemical model (BFM) was used to study nutrient uptake rates, N:P stoichiometry and the implications of these on estimated nitrogen fixation in the Benguela. The interactions between nitrogen and phosphate were investigated at selected stations at 21°S and off Walvis Bay. Higher nitrogen than phosphate uptake rates are shown at the stations at 21°S indicating luxury uptake of nitrogen by phytoplankton. This can also be attributed to demand for nitrate in phytoplankton since it is considered as the proximate limiting nutrient for instantaneous growth (Tyrrell, 1999). Phosphate uptake is dominated by diatoms and nanoflagellates at 21°S and off Walvis Bay respectively. The phosphate uptake rates at station N1DB02–4 increase with distance from the coast partly due to the succession of picophytoplankton in oligotrophic waters. A strong phosphate uptake is shown for nanoflagellates and picophytoplankton at these stations. Phosphate uptake is weak for large phytoplankton suggesting that they contribute less to the phosphate uptake in the Benguela. Nitrate and phosphate concentrations in the Benguela scatter to both sides of the Redfield ratio, indicating that the system produces both N* and P* excess and deficits as previously reported (Flohr et al., 2014). Nitrogen loss through denitrification results in increased phosphate release under suboxic and anoxic conditions. Nitrate consumption is high under these conditions resulting in low N* concentrations relative to P*. As such, phosphate release is accelerated under oxygen concentrations below 50 mmol O_2 m^{-3} (McManus et al., 1997).

Estimated nitrogen fixation is very low in the Benguela upwelling system. Estimated, depth–integrated nitrogen fixation rates are slightly higher at offshore stations. The slightly higher nitrogen fixation rates off Walvis Bay are attributed to nutrient supply below the Redfield ratio. It has been reported that nitrogen fixation is stimulated in oligotrophic regions adjacent to upwelling systems demonstrated by increasing estimated nitrogen fixation rates with distance from the coast in this study. At 21°S the estimated nitrogen fixation rates are slightly lower than off Walvis Bay and this is attributed to high nitrate concentrations from the nutrient–rich SACW. Therefore, in addition to low temperatures and an absence of *Trichodesmium* it is suggested that high N:P ratios in the shallow coastal waters of the Benguela limit nitrogen fixation. This results in excess phosphate not being taken up by nitrogen fixers and transported into the South Atlantic (Flohr et al., 2014).

6 | Silica cycling in the Benguela upwelling system

Abstract

Silica dynamics including uptake rates, growth of diatoms in different silicate concentrations, Si:N stoichiometry and dissolution are investigated in this chapter. The coupled NEMO–BFM 1D model is applied in the selected stations to understand these dynamics. Annual mean, depth–integrated silicate uptake rates are higher at the stations at 21°S (N1DB01 - 3.34×10^{-3} and N1DB03 - 2.83×10^{-3} mmol Si m^{-2} d^{-1}) than off Walvis Bay (N1DB02 - 2.07×10^{-3} and N1DB04 - 2.58×10^{-3} mmol Si m^{-2} d^{-1}). The high uptake rates at 21°S are attributed to increased primary production at the shallow station (N1DB01). A strong diatom subsurface maxima corresponding with the high silicate uptake rates is shown at the stations. Maximum diatom growth at offshore stations is reached at silicate concentrations between 2–3 mmol Si m^{-3}. In contrast, maximum diatom growth on the shallow coast (station N1DB01) is reached at high silicate concentrations ($\sim$ 10 mmol Si m^{-3}). These results agree with findings that diatoms have the ability to dominate phytoplankton communities in regions where silicate concentrations exceed 2 mmol Si m^{-3}. Simulated Si:N ratios in subsurface waters in the Benguela show excess nitrate relative to silicate. At station N1DB01, a secondary Si:N peak attributed to nitrogen loss through denitrification is observed under suboxic conditions. Despite the high denitrification rates at the shallow coast, the results suggest that the Benguela is a system characterized by lower silicate concentrations relative to nitrate. This excess nitrate is attributed to nutrient–rich SACW at the stations at 21°S. Silicate concentrations between 0–10 mmol Si m^{-3} at stations N1DB01, N1DB02 and N1DB03 correspond with increased oxygen ($\geq$ 60 mmol O_2 m^{-3}). In contrast, high silicate concentrations at these stations occur at suboxic conditions and can be attributed to organic matter degradation. The offshore station (N1DB04) exhibits high silicate concentrations in deeper, well–oxygenated waters due to exported particles. Dissolution of biogenic silica particles is high in warm surface waters and decreases in cold, deeper waters. Decreased dissolution results in high silicate concentrations in bottom, cold waters of station N1DB04. High biogenic silica production on the shallow coast (N1DB01) results in increased carbon export estimated to be 2.94 mg C m^{-2} d^{-1}. As such carbon export at this station is linked to increased ballasting of diatom biomass produced on the shallow coast.

6.1 Introduction

Silica is a key nutrient element in the ocean, it is required for the growth of diatoms and some sponges. It is also utilized by radiolarians, silicoflagellates, several species of choanoflagellates and some picocyanobacteria. Despite the long interest in siliceous organisms, only during the late 20th century have processes controlling silica marine biogeochemistry been quantified (Treguer et al., 1995). The silica budgets for the world oceans have also been constructed to improve understanding on cycling of this element (Treguer et al., 1995; Laruelle et al., 2009). These studies reveal that the silica cycle is strongly connected with other major biogeochemical cycles such as those of carbon and nitrogen. It is therefore closely related to marine primary production and the export of carbon to the deep sea (Pondaven et al., 2000). For nearly 20 years, the marine silica budget with its evaluation of reservoirs, processes, sources and sinks has been documented and provided important information for understanding the silica cycle (Treguer et al., 1995). Recently, the budget has been revised to incorporate new findings and changes that occurred over the years. The revisited silica cycle notes that the recycling of silica mostly occur at the sediment–water interface level and not during the sinking of silica particles through deep waters as previously understood (Honjo et al., 2008; Nelson et al., 2002).

Siliceous organisms biochemically produce biogenic silica in the photic zone of the ocean. This silica is directly recycled in the ocean surface and part of it is exported to the deep ocean. The biogenic silica continues to dissolve throughout the water column as particles sink through the deep ocean thus regenerating silica in the process (Tréguer and De La Rocha, 2013). The silica that passes through the water column untransformed accumulates at the water–sediment interface, where dissolution continues. The gross production of biogenic silica from primary production in the ocean is mainly attributed to diatoms (Nelson et al., 1995). Contribution by other siliceous protists such as silicoflagellates and radiolarians has been considered (Tréguer and De La Rocha, 2013). However, these organisms are not well known, and their contribution is likely to be less than that of diatoms. For example Adjou et al. (2011) estimated the production of biogenic silica by radiolarians to account for $\sim$ 1 to 6 mmol m^{-2} d^{-1} in the upper 120 m of the eastern equatorial Pacific. A recent study reported that silica–containing picoplankton may be responsible for up to 60% of the biogenic silica in the water column (Baines et al., 2012). Validation of these findings could add more perspective and understanding of the biogenic

silica cycle (Tréguer and De La Rocha, 2013).

Major silica production in the coastal zones is attributed to diatoms as they are the major component of phytoplankton. Estimated silica production is 6 Tmol Si y^{-1} and 74 Tmol Si y^{-1} for major upwelling zones and EBCs outside major upwelling zones respectively (Shipe and Brzezinski, 2001). If the estimated 56 Tmol Si y^{-1} from western boundary systems is added to EBCs estimates, the total biogenic silica production in the coastal zone is $\sim$ 136 Tmol Si y^{-1} (Brzezinski, 1985). Part of this production is recycled or lost in the surface layer through dissolution of the biogenic silica (Tréguer and De La Rocha, 2013). Time series located in the two large oligotrophic gyres of the Northern Hemisphere show that significantly larger fractions of biogenic silica are lost to dissolution in surface waters of North Atlantic as compared to the North Pacific (Tréguer and De La Rocha, 2013). The smaller losses in the North Pacific are linked to increased export efficiency of silica (Brzezinski et al., 2011). The undissolved biogenic silica fraction is exported towards the ocean interior in sinking particles. Export flux of biogenic silica into sediment traps in the North Atlantic at 2 km depth averages 0.006 mol Si m^{-2} yr^{-1} (Honjo et al., 2008). The average silica fluxes in the Atlantic (0.039 mol Si m^{-2} yr^{-1}) and warm Pacific pool (0.007 mol Si m^{-2} yr^{-1}) have been reported to be smaller compared to the North Pacific polar front (0.578 mol Si m^{-2} yr^{-1}) and the Southern Ocean (0.409 mol Si m^{-2} yr^{-1}) (Honjo et al., 2008). The total global export of biogenic silica to the bathypelagic zone is estimated at 34.4 $\pm$ 2.6 Tmol Si yr^{-1} (Honjo et al., 2008). However, this total flux is considered to be an underestimate as it excludes coastal zones and continental shelves, which tend to have higher export fluxes (Collins et al., 2011; Tréguer and De La Rocha, 2013).

Burial of biogenic silica in sediments results in permanent removal of silica from the water column. Dissolution of biogenic silica deposited at the sediment–water interface continues until a saturation concentration is reached (Tréguer and De La Rocha, 2013). This implies that silica "rain" rates exceed long term burial rates. The long term burial of biogenic silica occurs below the upper 10–20 cm of sediment (Tréguer and De La Rocha, 2013).The largest long term burial rates of biogenic silica are associated with continental margins, the North Pacific, the equatorial Pacific, and the Southern Ocean (DeMaster, 2002; Tréguer and De La Rocha, 2013). Few silica burial rates have been reported for the coastal zone and continental margins, as such, it has been suggested that the burial of silica is related to inorganic carbon (DeMaster, 2002). Due to downslope transport, not all biogenic

silica produced on the continental margin remains there (Tréguer and De La Rocha, 2013). As a result a Si:C ratio and downslope transport of particulate organic carbon is used to estimate downslope transport of biogenic silica from the continental margin to the deep sea (Chen, 2010; Ragueneau et al., 2009).

At low temperatures the dissolution of seafloor basalt and terrigenous silica deposited in sediments act as an additional external source of dissolved silica to the ocean. Earlier silica budgets of 0.4 ± 0.3 Tmol Si y^{-1} from seafloor basalt have been reported (Treguer et al., 1995; Wollast, 1983). These estimates of silica from seafloor basalt excluded dissolution of terrigenous sediments. Benthic silica effluxes as high as 10–20 mmol Si m^{-2} y^{-1} have been reported for the biogenic silica deficient seafloor of the Southern Angola Basin (Van Bennekom and Berger, 1984). Few studies have investigated the dynamics of silica cycling in the Benguela upwelling system. (Romero et al., 2002) investigated seasonal fluxes of siliceous particles and biogenic opal in the central Benguela. A highly partitioned, 3D model was proposed by Giraudeau et al. (2000) to explain process that control biogenic silica production in the Benguela. Despite efforts from these studies, little is known about other aspects of silica dynamics such as uptake rates and dissolution in the system.

Recent studies suggest that the silica cycle in the coastal zone is highly sensitive to anthropogenic pressure (Bernard et al., 2011; Ittekkot et al., 2012; Laruelle et al., 2009). Increased dissolution of biogenic silica in the coastal zone is expected with warming (Tréguer and De La Rocha, 2013). This is further expected to decrease export of biogenic silica to deeper waters. Subsequent drastic changes in coastal primary production and to coastal systems are expected to result. Silica limitation of diatom growth in coastal oceans is likely to increase with warming (Tréguer and De La Rocha, 2013). Subsequently, primary production is likely to be dominated by non–siliceous phytoplankton. Since recent studies indicate that silica is recycled in the water–sediment interface and during sinking of particles, it may be more vulnerable as oxygen minimum zones expand in response to warming. Presently, dissolution of biogenic silica may be modified by the slowed degradation of organic matter observed in OMZs, and by a combination of warming and expanding OMZs in the future. It is therefore important to understand present silica feedback processes in response to OMZs in the Benguela. This will allow prediction of future changes in the silica cycle based on these present processes. The BFM model is applied in this chapter to understand these processes in the Benguela.

6.2 Results and discussion

Silicate concentrations during the MSM 19/1b cruise were depleted in surface waters due to uptake by diatoms and accumulated at depth (Figure 6.1). The silicate concentrations along the cruise track increased below 150 m in suboxic waters. High concentrations of up to 38 mmol Si m^{-3} accumulated in bottom waters of stations 1031–34. Off Walvis Bay, silicate concentrations increased on the continental shelf slope at stations 1042-43. At station 1029 corresponding to N1DB01 silicate concentrations ranged between 1.73–14.63 mmol Si m^{-3}. Station 1043 (N1DB02) and 1035 (N1DB03) exhibited silicate concentrations between 1.30–25.99 and 2.75–10.28 mmol Si m^{-3} respectively. Off Walvis Bay, station 1042 (N1DB04) showed silicate concentrations between 1.51–12.66 mmol Si m^{-3}. Distribution of silicate at depth in the model corresponds with the MSM 19/1b data as described in Section 3.3.2. Simulated silicate concentrations are within the observed range in the surface and increase at depth. Increased silicate concentrations below 100 m at station N1DB02 and N1DB03 in the model can be attributed to sinking silica particles. High silicate concentrations occur at suboxic conditions and accumulate on the shallow shelf both in the model and MSM 19/1b data. Off Walvis Bay, simulated silicate concentrations at station N1DB02 and N1DB04 increased at depth corresponding with the MSM 19/1b data at station 1039–1044.

6.2.1 Silicate uptake by diatoms

The silicate uptake rates over the simulation period are presented in figure 6.2a–d. Net silicate uptake rates at the stations are lower than nitrogen and higher than phosphate uptake. In contrast, the depth of increased silicate uptake is deeper than nitrogen due to uptake by heavy diatoms. Silicate uptake in surface waters increased during spring at all stations in correspondence with nitrogen and phosphate. Maximum silicate uptake rates in surface waters occur at station N1DB01 during October. Increased silicate uptake in subsurface waters was also noted at 40–100 m at all stations. Similar to nitrogen and phosphate, subsurface silicate uptake remained fairly constant throughout spring to autumn. Station N1DB01 on the shallow coast showed higher silicate uptake rates than other stations. The high silicate uptake at this station is attributed to high primary

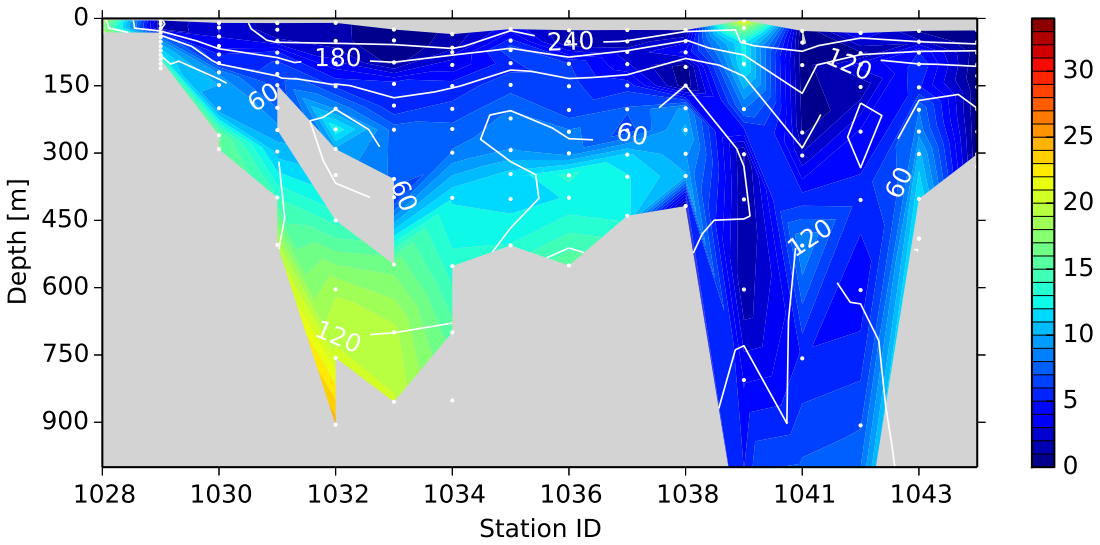

Figure 6.1: Section of silicate concentrations [mmol Si m^{-3}] in the Benguela shelf waters. The vertical dotted white lines denote the CTD casts where silicate samples for measurements were taken during the MSM 19/1b cruise. White contours represent oxygen concentrations [mmol O_2 m^{-3}].

production on the shallow coast. In correspondence with nitrogen and phosphate, silicate uptake rates also decrease significantly below 100 m.

Maximum silicate uptake rates at the stations ranged from 7.40×10^{-3} to 9.04×10^{-3} mmol Si m^{-3} d^{-1}. Annual mean silicate uptake rates were 3.34×10^{-3} and 2.83×10^{-3} mmol Si m^{-2} d^{-1} for stations N1DB01 and N1DB03 respectively. Off Walvis Bay, the annual mean silicate uptake rates were 2.07×10^{-3} and 2.58×10^{-3} mmol Si m^{-2} d^{-1} for stations N1DB02 and N1DB04 respectively. These uptake rates decrease with distance from the coast. High silicate uptake rates at station N1DB01 can be attributed to increased primary production on the shallow coast. Measurements of silicate uptake rates in the Benguela are not well–documented. However, diatoms in continental shelf reefs have been reported to utilize silicate at rates (0.01–0.9 mmol Si m^{-2}) similar to sponges (Maldonado et al., 2011). Franck et al. (2005) reported size–fractionated silicic acid uptake rates that ranged from 0.46–2.47 and 0.17–1.10 μmol $Si(OH)_4$ L^{-1} d^{-1} in the Monterey Bay and eastern tropical Pacific waters respectively. Silicate uptake rates in this study are lower compared to these studies.

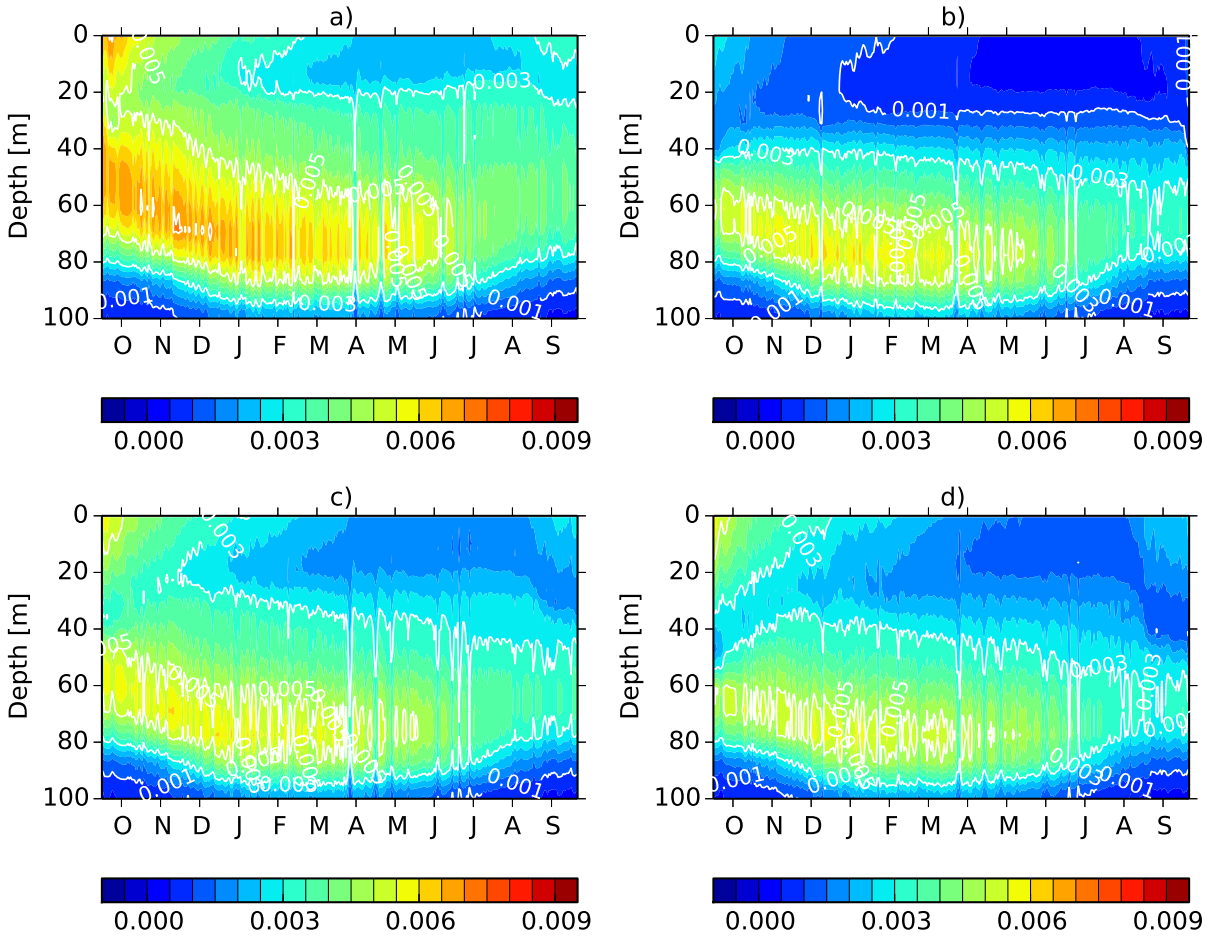

Figure 6.2: Simulated silicate uptake rates [mmol Si m^{-3} d^{-1}] for station (a) N1DB01, (b) N1DB02, (c) N1DB03 and (d) N1DB04.

Simulated diatom concentrations in the Benguela stations are presented in figure 6.3a–d. The diatoms seasonal growth at the stations is consistent with silicate uptake rates in surface and subsurface waters. In surface waters, diatom concentrations reached 0.06 mmol Si m^{-3} at station N1DB01 during October. Stations N1DB02, N1DB03 and N1DB04 showed low diatom concentrations in surface waters during February to August. A strong subsurface diatom maxima was also observed at station N1DB01. The maximum diatom concentrations in subsurface waters did not exceed 0.10 mmol Si m^{-3} at stations N1DB02–4. Diatom growth occurred throughout spring to autumn and decreased during late winter except at station N1DB01. This station showed higher diatom concentrations during winter compared to other stations. The concentration of diatoms at the stations decrease with distance from the coast. Increased diatom growth at station N1DB01 is attributed to high nutrient

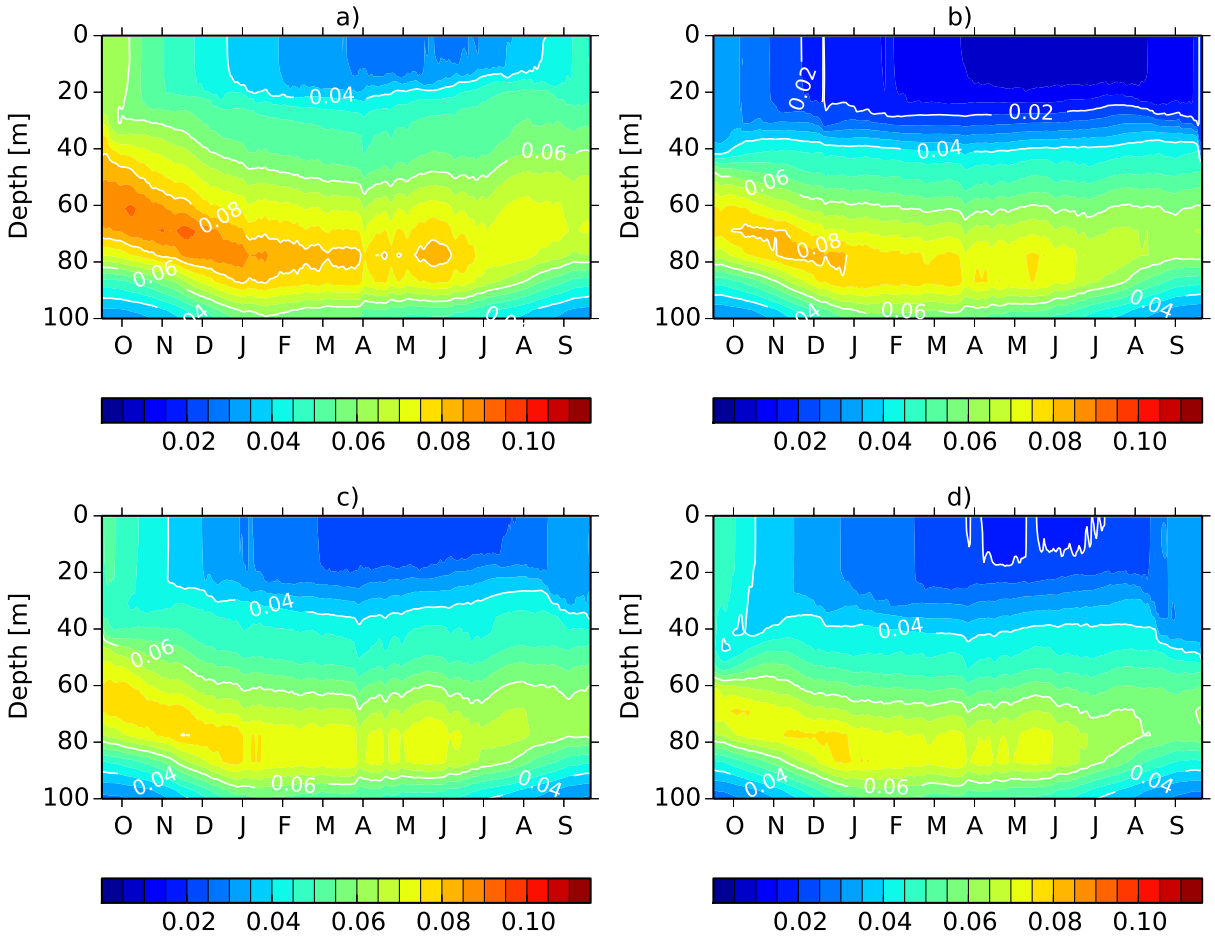

Figure 6.3: Simulated diatoms concentrations [mmol Si m^{-3}] for station (a) N1DB01, (b) N1DB02, (c) N1DB03 and (d) N1DB04.

concentrations on the shallow coast. At offshore stations, limited growth of diatoms can be linked to low nutrient concentrations and decreased primary production in surface waters.

A previous study in the pelagic central Benguela (29°S, 13°E) found diatoms to be the dominant siliceous species throughout the year compared to silicoflagellates, radiolarians, phytoliths and dinoflagellates (Romero et al., 2002). Diatom abundance in the above–mentioned study increased in mid–winter and summer which is consistent with simulated results at station N1DB01. At station N1DB02, N1DB03 and N1DB04 low diatom concentrations occur during winter and can be attributed to horizontal processes such as offshore transport of chlorophyll particles. Winter diatom peak in the central Benguela has been linked to strong water column mixing and offshore transport of chlorophyll

filaments (Romero et al., 2002). The surface, simulated chlorophyll concentrations in this study are underestimated due to the missing offshore transport (Figure 6.7 – Appendix). Therefore, in addition to low nutrient concentrations and primary production, the low diatom concentrations during winter at offshore stations can be explained by the absence of offshore particulate transport.

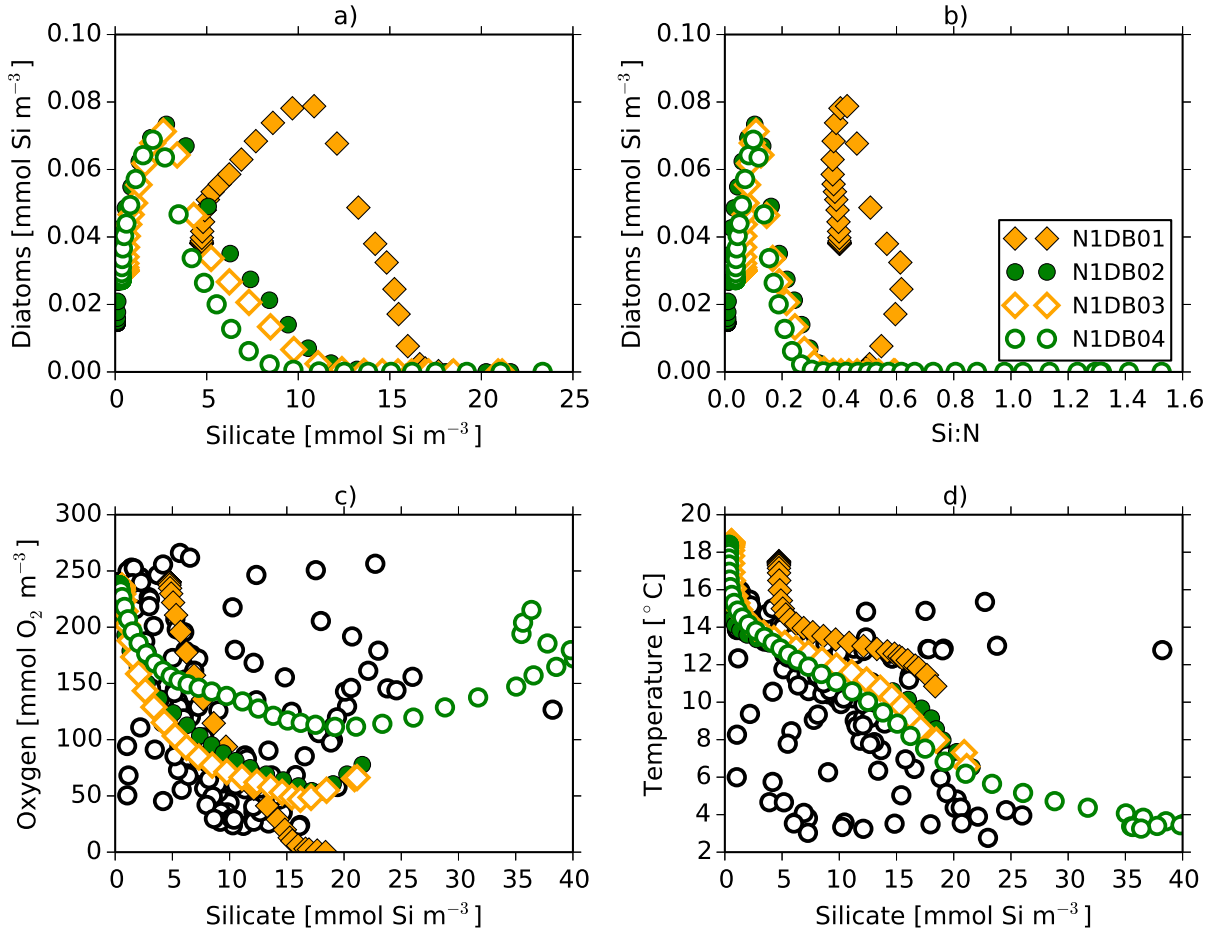

Figure 6.4: Annual mean simulated silicate concentrations (a) and (b) Si:N ratios versus diatom concentrations for the stations. Silicate versus (c) oxygen and (d) temperature is also shown. Black open markers indicate silicate concentrations during the MSM 19/1b cruise.

6.2.2 Si:N stoichiometry and silicate dissolution

Annual mean diatom concentrations at station N1DB02, N1DB03 and N1DB04 reach up to 0.08 mmol Si m^{-3} coincident with silicate concentrations between 2–3 mmol Si m^{-3} (Figure 6.4a). The maximum diatom growth occurs in subsurface waters at these stations

as indicated earlier. Station N1DB01 showed increased diatom concentrations at higher silicate concentrations ($\sim$ 5 mmol Si m^{-3}). Annual mean diatom concentrations at this station exceeded 0.08 mmol Si m^{-3} in silicate concentrations $\sim$ 10 mmol Si m^{-3}. Diatoms in mesocosm experiments have been reported to dominate phytoplankton communities in regions where silicate concentrations exceed 2 mmol Si m^{-3} (Egge and Aksnes, 1992). A steep slope at silicate concentrations $\leq$ 2 mmol Si m^{-3} has been reported for the relationship between silicate and sedimentary diatom abundance for the global oceans (Abrantes et al., 2016), which is consistent with results from station N1DB02, N1DB03 and N1DB04.

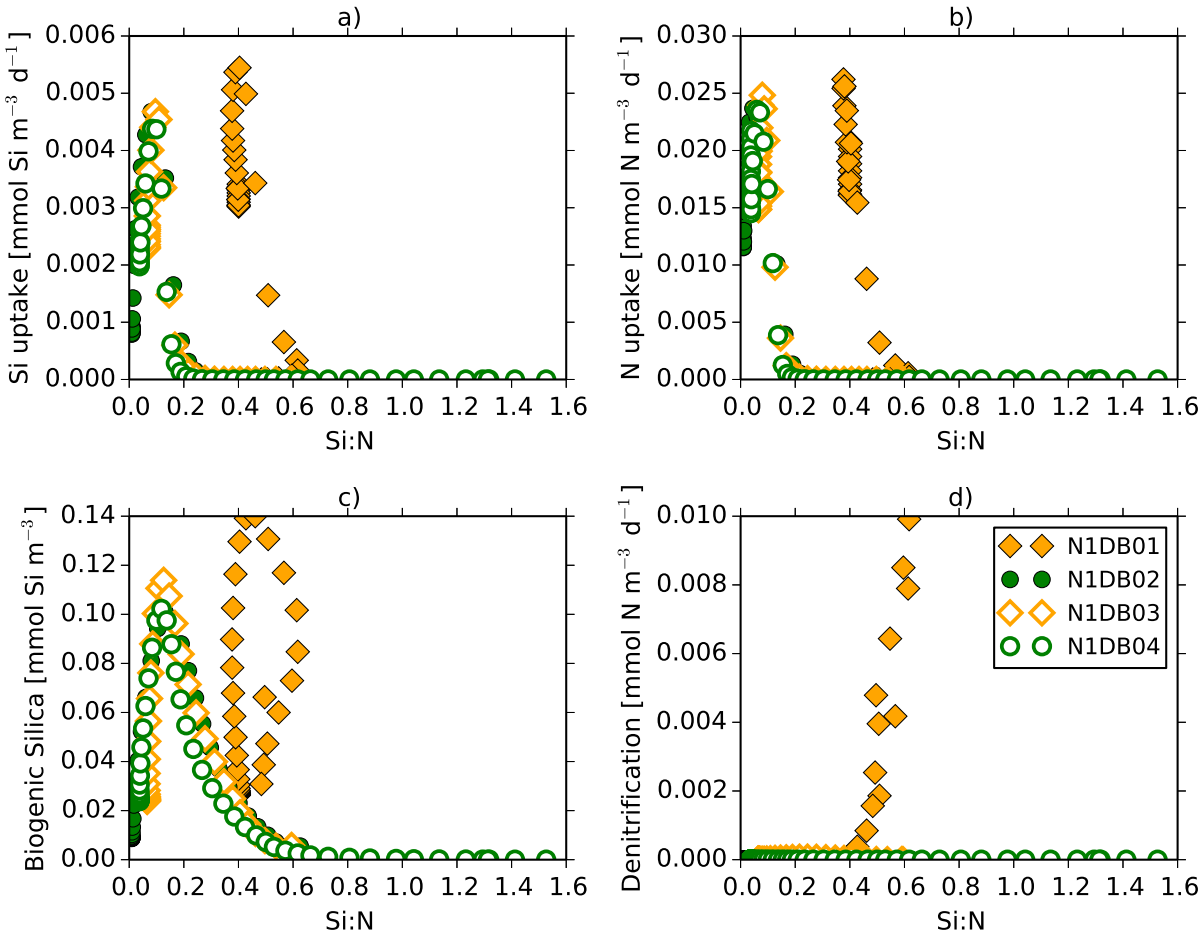

Figure 6.5: Annual mean simulated Si:N ratios versus (a) silica uptake rates, (b) nitrogen uptake rates, (c) biogenic silica and (d) denitrification rates for the stations.

Diatoms reached maximum growth in low Si:N ratios at station N1DB02, N1DB03 and N1DB04 (Figure 6.4b). Increased silicate uptake and diatom growth at these stations was

shown at Si:N concentrations ~ 0.1 in surface waters (Figure 6.5a). The Si:N ratios at station N1DB01, N1DB02 and N1DB03 did not exceed 0.6 in bottom waters. Station N1DB04 shows high Si:N ratios (≤ 1.5) in bottom waters. In contrast to other stations, diatoms at station N1DB01 reached maximum growth at higher Si:N ratios ~ 0.4 in subsurface waters. A secondary Si:N peak (≤ 0.6) is shown at station N1DB01 and is followed by a decline in bottom waters (Figure 6.4b). The low Si:N ratios at stations N1DB02, N1DB03 and N1DB04 indicate both depleted nitrate and silicate concentrations in surface waters. High Si:N ratios at station N1DB01 on the shallow coast are partly attributed to high denitrification rates (Figure 6.5d). The depletion of nitrate during denitrification coupled with increased biogenic silica concentrations lead to the secondary Si:N peak from low nitrate relative to silicate at this station (Figure 6.5c). Diatoms usually use silicate in a 1:1 ratio with nitrate under sufficient macronutrients and micronutrients (Brzezinski, 1985). Results from this study suggest that diatom at these stations use silicate with nitrate below this ratio.

Similar Si:N ratios have been reported in coastal California waters (Brzezinski et al., 2015). In that study, Si:N ratios between 1.0–2.0 and above 2.0 were assumed to represent nutrient–replete diatoms and excess silicate over nitrate relative to diatom demand (Brzezinski, 1985). Ratios below 1.0 were assumed to represent nitrate excess relative to silicate. Following this grouping, simulated Si:N ratios in subsurface waters show excess nitrate in relation to silicate. Si:N ratios above 1.0 at station N1DB04 can be attributed to exported silicate particles in deep waters. Simulated Si:N ratios at the stations do not exceed 2.0 suggesting diatoms in the Benguela stations grow under both excess nitrate and nutrient replete conditions. Preferential depletion of silicate by diatoms has been suggested to indicate iron stress in low Si:N waters (Brzezinski et al., 2015). Iron is not limiting in the Benguela. As such, low Si:N ratios in the Benguela can be attributed to the dominant presence of nitrate–rich SACW on the shallow coast at 21°S.

Silicate concentrations between 0–10 mmol Si m^{-3} at station N1DB01, N1DB02 and N1DB03 are present at high oxygen concentrations ($\geq$ 60 mmol O_2 m^{-3}) (Figure 6.4c). Silicate concentrations at these high oxygen levels were below 10 mmol Si m^{-3}. Silicate concentrations under suboxic and anoxic conditions at these stations ranged from 11–22 mmol Si m^{-3}. This can be attributed to the degradation of organic matter and oxygen consumed in the process. The offshore station, N1DB04 showed high silicate concentrations ($\sim$ 40 mmol Si m^{-3}) at high oxygen conditions ($\sim$ 150 mmol O_2 m^{-3}). The high silicate

concentrations at this station can be attributed to sinking particles in deeper waters. The relationship between silicate and oxygen from the model results is similar to the relationship observed during the MSM 19/1b cruise (Figure 6.4c). The silicate concentrations during the cruise increased under suboxic conditions. These results suggest that organic matter degradation in suboxic conditions leads to an increase in biogenic silica concentrations.

Silicate dissolution is shown at high temperatures and decreases in cold deeper waters (Figure 6.4d). Silicate concentrations $\sim$ 1 mmol Si m^{-3} are shown at high temperature (14–18°C) at station N1DB02, N1DB03 and N1DB04. The silicate concentrations ($\sim$ 5 mmol Si m^{-3}) were high at a similar temperature range at station N1DB01 on the shallow coast. These depleted silicate concentrations at high temperatures can be attributed to dissolution and uptake in surface and subsurface waters. Van Cappellen et al. (2002) reported that 50–60% of silica opal produced in the euphotic zone redissolves within the upper 100 m corresponding with results from this study. Silicate concentrations increased to $\sim$ 10 mmol Si m^{-3} for station N1DB01 and $\sim$ 22 mmol Si m^{-3} for station N1DB02 and N1DB03 in colder waters (8–14°C). Station N1DB04 showed high silicate concentrations of up to 40 mmol Si m^{-3} in bottom waters. The high silicate concentrations are from undissolved particles that pass through the water column and are exported towards the ocean interior. Dissolution of these particles continues at the water–sediment interface until a saturated state is reached (Tréguer and De La Rocha, 2013).

6.2.3 Biogenic silica production and carbon export in the Benguela

Biogenic silica concentrations at the stations are presented in figures 6.6a–d. Increased biogenic silica production occurs in surface waters. These increased concentrations also occur in subsurface waters from October to June and decrease significantly during late winter. Biogenic silica concentrations at the stations are higher at 21°S than off Walvis Bay and decrease with increasing distance from the coast. Maximum concentrations at the stations range between 0.13–0.18 mmol Si m^{-3}. Station N1DB01 on the shallow coast showed increased biogenic silica production than other stations. The average biogenic silica concentration in the global ocean has been estimated to be 0.2 mmol Si m^{-3} (in the upper 150 m) which is above the maximum concentration in this study (Van Cappellen et al., 2002). The estimation may not be realistic given the different oceanic regions and variability in silicate concentrations. In agreement however, the maximum concentrations in this study

occur in the upper 150 m of the water column.

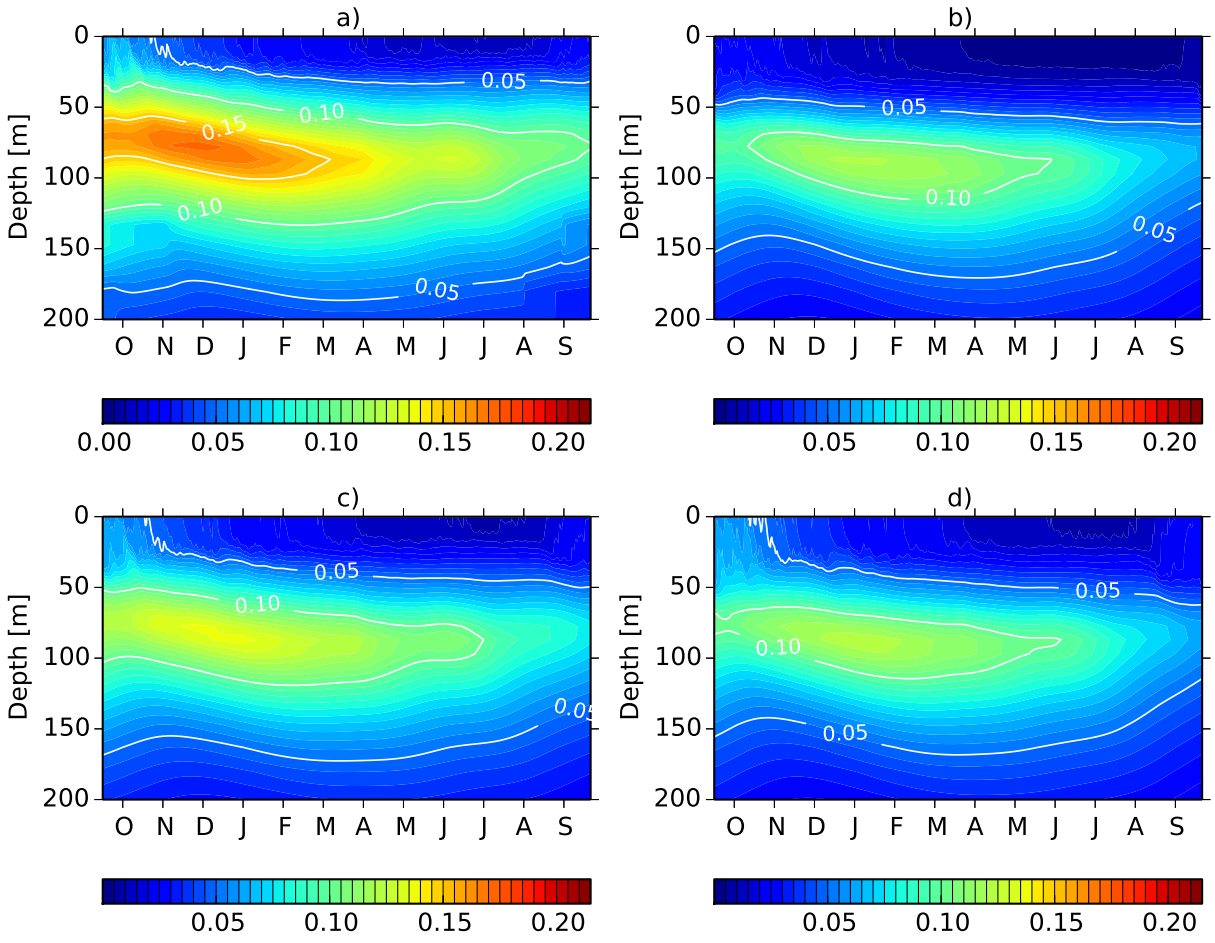

Figure 6.6: Simulated biogenic silica concentrations [mmol Si m^{-3}] for station (a) N1DB01, (b) N1DB02, (c) N1DB03 and (d) N1DB04.

Biogenic silica concentrations were reported to be high under low Si:N ratios (Brzezinski et al., 2015). In agreement, biogenic silica concentrations are high at station N1DB01 on the shallow coast. Stations N1DB02, N1DB03 and N1DB04 exhibited lower biogenic silica concentrations under low Si:N concentrations in comparison to this station. Gravitational export measurements at 100 m have been reported to show high average export of biogenic silica in the California current coastal waters (Brzezinski et al., 2015). This high export of biogenic silica at 100 m occurred below low Si:N waters. Results from this study are

in agreement since there is a strong biogenic silica maxima around 100 m at the stations. Biogenic silica export is high on the shallow coast (N1DB01) compared to offshore stations possibly due to the increased diatom biomass observed in coastal waters.

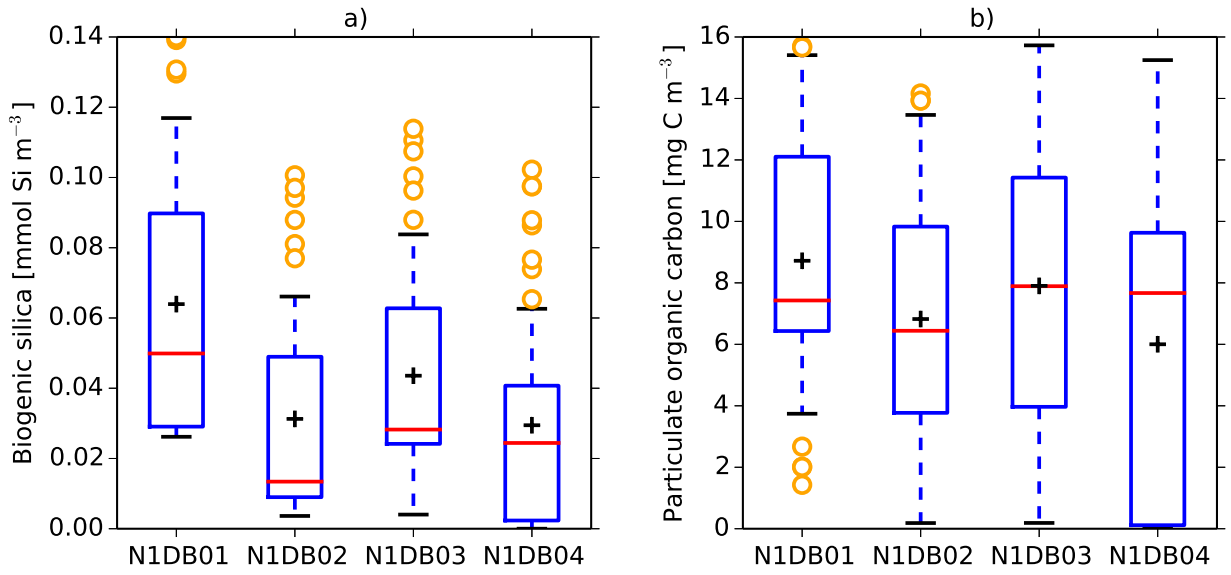

Figure 6.7: Box plots of simulated biogenic silica (a) and (b) particulate organic carbon concentrations. Red and black horizontal lines show medians and upper quartiles respectively. Black (+) and orange open circles indicate the mean and outliers. The outliers indicate high biogenic silica concentrations in subsurface waters (50–100 m).

Annual mean biogenic silica and POC concentrations at the stations are presented (Figure 6.7). Increased biogenic silica and POC production was high at the stations at 21°S than off Walvis Bay. The annual mean POC concentrations were 0.06 and 0.04 mg C m^{-2} for station N1DB01 and N1DB03 respectively. Off Walvis Bay, annual mean POC concentrations were 0.04 and 0.03 mg C m^{-3} for station N1DB02 and N1DB04 respectively. The POC concentrations off Walvis Bay correspond with low biogenic silica concentrations. Annual mean POC export at the stations decreased with distance from the coast. High POC export of 2.94 mg C m^{-2} d^{-1} was exhibited at station N1DB01. The simulated annual mean POC export was 0.29, 0.29 and 0.04 mg C m^{-2} d^{-1} for stations N1DB02, N1DB03 and N1DB04 respectively. Seasonal organic carbon fluxes in the central Benguela were reported to range between 0.8–10.9 mg m^{-2} d^{-1} corresponding with estimated concentrations from station

N1DB01 (Romero et al., 2002). Increased summer and winter organic carbon fluxes in the study were attributed to the offshore migration of chlorophyll filaments and increased in–situ production respectively. Carbon export has been found to be relatively high in low Si:N waters (Brzezinski et al., 2015). This enhanced export of biogenic silica and POC in low Si:N waters has been attributed to increased ballasting due to increased diatom biomass (Hutchins and Bruland, 1998). Diatoms have been reported to contribute significantly to carbon export in low Si:N waters (Brzezinski et al., 2015). Diatoms dominated the phytoplankton communities in this study and they are also considered to contribute significantly to the export of carbon (Table 6.2).

Silicate dissolution is high in Benguela surface waters as reported. In a scenario of increased warming in this region, silicate can be expected to be a limiting nutrient (Tréguer and De La Rocha, 2013). This is expected to decrease biogenic silica export into deeper waters thus affecting carbon burial as well. A shift in phytoplankton communities in this scenario could easily occur due to silicate limitation in the diatom assemblages. Non–siliceous phytoplankton are expected to dominate in such conditions. However, expansion of the OMZ is expected with warming and suboxic conditions are linked with slow organic matter degradation. This implies that high silicate dissolution will occur in surface waters and degradation of organic matter will be slowed at depth. So this creates difficulties in understanding and predicting changes for the silica cycle. If changes occur, it would be hard to detect because of high variability in coastal waters and it would have to be on a time–scale of decades to 100 years.

6.3 Conclusions

The BFM model was applied in the Benguela to understand the silica cycle. Silica dynamics including uptake rates, growth of diatoms in different silicate concentrations, Si:N stoichiometry, silica dissolution, biogenic silica production and its implications for carbon export were studied. High silicate uptake rates occur in subsurface waters on the shallow coast. Simulated silicate uptake rates are lower compared to previous studies and this can be attributed to generally depleted surface silicate concentrations and low primary production at offshore stations (Franck et al., 2005; Maldonado et al., 2011). A strong subsurface diatom maxima corresponding with high silicate uptake rates is observed at the stations. These maxima also occur during winter on the shallow coast but are depleted at offshore stations due to the omission of horizontal processes such as offshore transport of particles.

Diatoms were found to dominate phytoplankton communities where silicate concentrations exceed 2 mmol Si m^{-3} in agreement with previous studies (Egge and Aksnes, 1992). Maximum diatom growth is reached at higher Si:N ratios on the shallow coast than at offshore stations. A secondary Si:N peak is observed on the shallow coast (N1DB01) and partly attributed to nitrogen loss through denitrification. Denitrification on the shallow coast results in depletion of nitrate relative to silicate. Diatoms use silicate and nitrate below the 1:1 ratio this being the result of relatively depleted, surface silicate concentrations at the stations. From the Si:N ratios the Benguela can be classified as a region with excess nitrate concentrations relative to silicate. This is attributed to domination of the nutrient–rich SACW at 21°S.

Surface silicate concentrations between 0–10 mmol Si m^{-3} at the stations correspond with high oxygen levels. Increased silicate concentrations also occur under low oxygen and are attributed to organic matter remineralization. Silicate concentrations increase in well–oxygenated bottom waters at the offshore station (N1DB04) due to sinking particles. Silica dissolution is high in warm surface waters and decreases in colder, bottom waters. Biogenic silica production is high in subsurface waters at the stations. Biogenic silica export is also high on the shallow coast due to increased diatoms biomass. The high biogenic silica export results in increased annual mean POC export of 2.94 mg C m^{-2} d^{-1} in the shallow station. In agreement with previous studies, carbon export in the Benguela is high in low Si:N waters due to increased ballasting of diatom biomass.

Summary

This study investigated biogeochemical interactions in the Benguela upwelling system using coupled physical–biogeochemical models. The first objective of this study was to understand intermediary nitrogen process in the Benguela and the BioEBUS model was used in this respect. The BioEBUS model was also used in Chapter 4 to investigate nitrogen loss mechanisms and impats of the OMZ on nitrogen cycling in the system. The BFM model was then used to understand the effect of nitrogen loss through denitrification on the phosphorus cycle. The consequences of suboxic conditions on phosphate release and hydrogen sulphide production were also explored using the BFM model in Chapter 5. Chapter 6 aimed to understand silica dynamics including uptake rates, Si:N stoichiometry and biogenic silica dissolution. Silicate concentrations in oxic and suboxic conditions were explored in this chapter using the BFM model. Implications of biogenic silica export on carbon export was also investigated in Chapter 6.

One of the key findings from the BioEBUS model in Chapter 4 is that nitrite maxima accumulate in the ABF region OMZ due to high rates of denitrification. These nitrite maxima are consumed by high rates of anammox off Walvis Bay. Nitrous oxide production is high in the ABF as a result of increased nitrification and accelerated production under suboxic conditions. Nitrous oxide is produced in three different water masses in the ABF due to the steep slope. Nitrous oxide production in deeper water masses is missing off Walvis Bay because of the shallow shelf. High nitrogen fluxes in the Benguela are attributed to nitrification rather than anammox and denitrification. The simulated results show that denitrification is the dominant nitrogen loss mechanism in the Benguela OMZ.

In Chapter 5, The BFM model showed that phosphate release under suboxic conditions is coupled to denitrification and hydrogen sulphide production. This excess phosphate is released in suboxic bottom waters on the shallow coast. Phosphate remineralization is high under suboxic rather than well–oxygenated conditions. Due to low nitrogen fixation rates in the Benguela, it is suggested that the excess phosphate not taken up in coastal waters is transported into the South Atlantic. This is in agreement with a previous study that suggested the Benguela as a source of P* to the South Atlantic (Flohr et al., 2014). Simulated results suggest that in addition to absence of nitrogen fixing species and low

temperatures, the high nitrate concentrations associated with nutrient–rich SACW limit nitrogen fixation in coastal waters.

In Chapter 6, BFM results suggest that the Benguela is a system characterized by excess nitrate in relation to silicate. This has been inferred from the low Si:N ratios observed in the simulated stations. A secondary Si:N peak is shown in the shallow coast because of high denitrification rates in suboxic waters. High silicate concentrations also occur in suboxic conditions and can be attributed to organic matter remineralization. The high silicate concentrations at the well-oxygenated offshore stations are linked to sinking particles in deep waters. Increased silicate dissolution occurs in warm, surface waters and the particles that pass through the water column undissolved settle at the bottom where dissolution continues. From these results, it can be stated that increased warming in the Benguela coastal waters will result in silicate being a limiting nutrient. This could affect carbon export as it has been shown that increased POC export is high in coastal waters due to ballasting of diatom biomass.

Future work

The BioEBUS model has been extensively evaluated by (Gutknecht et al., 2013). It has been highlighted that there is a need to include oxygen consuming processes such as hydrogen sulphide to get the model to correctly simulate oxygen concentrations in the Benguela coastal region. This will greatly improve estimates of nitrogen fluxes in the region. The BFM 1D model performed fairly well in simulating biogeochemical interactions in the Benguela. There is a need to implement the adjustments made to the BFM model in this study in a 3D scenario. This will improve chlorophyll estimates since these are driven by horizontal processes such as offshore transport of blooms. Estimates of diatom concentrations in the Benguela can also be improved by the inclusion of advective processes. The winter nutrient bias observed in the analysis is mostly due to interchanges between the ESACW and SACW in the Benguela. Implementation of 3D physical processes in the model could improve these estimates significantly. As is the case in most modeling studies, there is a need for more in–situ observations to validate the calculated biogeochemical rates.

Bibliography

Abrantes, F., Cermeno, P., Lopes, C., Romero, O., Matos, L., Van Iperen, J., Rufino, M. M. and Magalhães, V. (2016), 'Diatoms si uptake capacity drives carbon export in coastal upwelling systems'.

Adjou, M., Tréguer, P., Dumousseaud, C., Corvaisier, R., Brzezinski, M. A. and Nelson, D. M. (2011), 'Particulate silica and si recycling in the surface waters of the eastern equatorial pacific', *Deep Sea Research Part II: Topical Studies in Oceanography* **58**(3), 449–461.

Aminot, A. and Kérouel, R. (2004), 'Dissolved organic carbon, nitrogen and phosphorus in the ne atlantic and the nw mediterranean with particular reference to non-refractory fractions and degradation', *Deep Sea Research Part I: Oceanographic Research Papers* **51**(12), 1975–1999.

Anderson, G. and Zeutschel, R. (1970), 'Release of dissolved organic matter by marine phytoplankton in coastal and offshore areas of the northeast pacific ocean', *Limnology and Oceanography* (3).

Andrews, W. and Hutchings, L. (1980), 'Upwelling in the southern benguela current', *Progress in Oceanography* **9**(1), 1–81.

Arrigo, K. R. (2005), 'Marine microorganisms and global nutrient cycles', *Nature* **437**(7057), 349–355.

Babbin, A. R., Bianchi, D., Jayakumar, A. and Ward, B. B. (2015), 'Rapid nitrous oxide cycling in the suboxic ocean', *Science* **348**(6239), 1127–1129.

Baines, S. B., Twining, B. S., Brzezinski, M. A., Krause, J. W., Vogt, S., Assael, D. and McDaniel, H. (2012), 'Significant silicon accumulation by marine picocyanobacteria', *Nature Geoscience* **5**(12), 886–891.

Bange, H. W. (2008), Gaseous nitrogen compounds (no, n₂o, n₂, nh₃) in the ocean, *in* D. G. Capone, D. Bronk, M. R. Mulholland and E. J. Carpenter, eds, 'Nitrogen in the Marine Environment', Elsevier, Amsterdam, pp. 51–94.
URL: *http://eprints.uni-kiel.de/2975/*

Bange, H. W. and Andreae, M. O. (1999), 'Nitrous oxide in the deep waters of the world's oceans', *Global biogeochemical cycles* **13**(4), 1127–1135.

Bange, H. W., Rapsomanikis, S. and Andreae, M. O. (2001), 'Nitrous oxide cycling in the arabian sea', *Journal of geophysical research* **106**, 1053–1066.

Baretta-Bekker, J., Baretta, J. and Ebenhöh, W. (1997), 'Microbial dynamics in the marine ecosystem model ersem ii with decoupled carbon assimilation and nutrient uptake', *Journal of Sea Research* **38**(3), 195–211.

Bender, M., Jahnke, R., Ray, W., Martin, W., Heggie, D. T., Orchardo, J. and Sowers, T. (1989), 'Organic carbon oxidation and benthic nitrogen and silica dynamics in san clemente basin, a continental borderland site', *Geochimica et Cosmochimica Acta* **53**(3), 685–697.

Benitez-Nelson, C. R. (2000), 'The biogeochemical cycling of phosphorus in marine systems', *Earth-Science Reviews* **51**(1), 109–135.

Berelson, W., McManus, J., Coale, K., Johnson, K., Burdige, D., Kilgore, T., Colodner, D., Chavez, F., Kudela, R. and Boucher, J. (2003), 'A time series of benthic flux measurements from monterey bay, ca', *Continental Shelf Research* **23**(5), 457–481.

Berman-Frank, I., Quigg, A., Finkel, Z. V., Irwin, A. J. and Haramaty, L. (2007), 'Nitrogen-fixation strategies and fe requirements in cyanobacteria', *Limnology and Oceanography* **52**(5), 2260–2269.

Bernard, C., Dürr, H., Heinze, C., Segschneider, J. and Maier-Reimer, E. (2011), 'Contribution of riverine nutrients to the silicon biogeochemistry of the global ocean–a model study', *Biogeosciences* **8**(3), 551–564.

Bianchi, D., Dunne, J. P., Sarmiento, J. L. and Galbraith, E. D. (2012), 'Data-based estimates of suboxia, denitrification, and n2o production in the ocean and their sensitivities to dissolved o2', *Global Biogeochemical Cycles* **26**(2).

Bidle, K. D. and Azam, F. (1999), 'Accelerated dissolution of diatom silica by marine bacterial assemblages', *Nature* **397**(6719), 508–512.

Broecker, W. S., Peng, T.-H. and Beng, Z. (1982), *Tracers in the Sea*, Lamont-Doherty Geological Observatory, Columbia University.

Brzezinski, M. A. (1985), 'The si: C: N ratio of marine diatoms: Interspecific variability and the effect of some environmental variables1', *Journal of Phycology* **21**(3), 347–357.

Brzezinski, M. A., Krause, J. W., Bundy, R. M., Barbeau, K. A., Franks, P., Goericke, R., Landry, M. R. and Stukel, M. R. (2015), 'Enhanced silica ballasting from iron stress sustains carbon export in a frontal zone within the california current', *Journal of Geophysical Research: Oceans* **120**(7), 4654–4669.

Brzezinski, M. A., Krause, J. W., Church, M. J., Karl, D. M., Li, B., Jones, J. L. and Updyke, B. (2011), 'The annual silica cycle of the north pacific subtropical gyre', *Deep Sea Research Part I: Oceanographic Research Papers* **58**(10), 988–1001.

Butler, J. H., Elkins, J. W., Thompson, T. M. and Egan, K. B. (1989), 'Tropospheric and dissolved n2o of the west pacific and east indian oceans during the el nino southern oscillation event of 1987', *Journal of Geophysical Research: Atmospheres (1984–2012)* **94**(D12), 14865–14877.

Capone, D. G. and Knapp, A. N. (2007), 'Oceanography: A marine nitrogen cycle fix?', *Nature* **445**(7124), 159–160.

Carr, M.-E. (2001), 'Estimation of potential productivity in eastern boundary currents using remote sensing', *Deep Sea Research Part II: Topical Studies in Oceanography* **49**(1), 59–80.

Carr, M.-E. and Kearns, E. J. (2003), 'Production regimes in four eastern boundary current systems', *Deep Sea Research Part II: Topical Studies in Oceanography* **50**(22), 3199–3221.

Carstensen, J., Andersen, J. H., Gustafsson, B. G. and Conley, D. J. (2014), 'Deoxygenation of the baltic sea during the last century', *Proceedings of the National Academy of Sciences* **111**(15), 5628–5633.

Casey, K. S. and Cornillon, P. (1999), 'A comparison of satellite and in situ-based sea surface temperature climatologies', *Journal of Climate* **12**(6), 1848–1863.

Chapman, P. and Shannon, L. (1985), 'The benguela ecosystem. ii: Chemistry and related processes', *Oceanography and marine biology* **23**, 183–251.

Chen, C.-T. A. (2010), Cross-boundary exchanges of carbon and nitrogen in continental margins1, *in* 'Carbon and Nutrient Fluxes in Continental Margins', Springer, pp. 561–574.

Clark, L. L., Ingall, E. D. and Benner, R. (1999), 'Marine organic phosphorus cycling: novel insights from nuclear magnetic resonance', *American Journal of Science* **299**(7-9), 724–737.

Codispoti, L. (1989), 'Phosphorus vs. nitrogen limitation of new and export production', *Productivity of the ocean: Present and past* **44**, 377–394.

Codispoti, L., Brandes, J. A., Christensen, J., Devol, A., Naqvi, S., Paerl, H. W. and Yoshinari, T. (2001), 'The oceanic fixed nitrogen and nitrous oxide budgets: Moving targets as we enter the anthropocene?', *Scientia Marina* **65**(S2), 85–105.

Codispoti, L. and Christensen, J. (1985), 'Nitrification, denitrification and nitrous oxide cycling in the eastern tropical south pacific ocean', *Marine Chemistry* **16**(4), 277–300.

Codispoti, L., Friederich, G., Packard, T., Glover, H., Kelly, P., Spinrad, R., Barber, R., Elkins, J., Ward, B., Lipschultz, F. et al. (1986), 'High nitrite levels off northern perú: a signal of instability in the marine denitrification rate', *Science* **233**(4769), 1200–1202.

Cohen, Y. and Gordon, L. I. (1978), 'Nitrous oxide in the oxygen minimum of the eastern tropical north pacific: Evidence for its consumption during denitrification and possible mechanisms for its production', *Deep Sea Research* **25**(6), 509–524.

Collins, L. E., Berelson, W., Hammond, D. E., Knapp, A., Schwartz, R. and Capone, D. (2011), 'Particle fluxes in san pedro basin, california: a four-year record of sedimentation and physical forcing', *Deep Sea Research Part I: Oceanographic Research Papers* **58**(8), 898–914.

Cotner, J. B. and Biddanda, B. A. (2002), 'Small players, large role: microbial influence on biogeochemical processes in pelagic aquatic ecosystems', *Ecosystems* **5**(2), 105–121.

Cotner, J. B. and Wetzel, R. G. (1992), 'Uptake of dissolved inorganic and organic bphosphorus compounds by phytoplankton and bacterioplankton', *Limnology and Oceanography* **37**(2), 232–243.

Da Silva, A., Young, C. and Levitus, S. (1994), 'Atlas of surface marine data 1994, vol. 1, algorithms and procedures, noaa atlas nesdis 6', *US Department of Commerce, NOAA, NESDIS, USA* .

Dalsgaard, T., Canfield, D. E., Petersen, J., Thamdrup, B. and Acuña-González, J. (2003), 'N2 production by the anammox reaction in the anoxic water column of golfo dulce, costa rica', *Nature* **422**(6932), 606–608.

Dalsgaard, T., Stewart, F. J., Thamdrup, B., De Brabandere, L., Revsbech, N. P., Ulloa, O., Canfield, D. E. and DeLong, E. F. (2014), 'Oxygen at nanomolar levels reversibly suppresses process rates and gene expression in anammox and denitrification in the oxygen minimum zone off northern chile', *MBio* **5**(6), e01966–14.

Dalsgaard, T., Thamdrup, B. and Canfield, D. E. (2005), 'Anaerobic ammonium oxidation (anammox) in the marine environment', *Research in Microbiology* **156**(4), 457–464.

Delaney, M. (1998), 'Phosphorus accumulation in marine sediments and the oceanic phosphorus cycle', *Global Biogeochemical Cycles* **12**(4), 563–572.

DeMaster, D. J. (2002), 'The accumulation and cycling of biogenic silica in the southern ocean: revisiting the marine silica budget', *Deep Sea Research Part II: Topical Studies in Oceanography* **49**(16), 3155–3167.

Deutsch, C., Gruber, N., Key, R. M., Sarmiento, J. L. and Ganachaud, A. (2001), 'Denitrification and n2 fixation in the pacific ocean', *Global Biogeochemical Cycles* **15**(2), 483–506.

Deutsch, C., Sarmiento, J. L., Sigman, D. M., Gruber, N. and Dunne, J. P. (2007), 'Spatial coupling of nitrogen inputs and losses in the ocean', *Nature* **445**(7124), 163–167.

Deutsch, C., Sigman, D. M., Thunell, R. C., Meckler, A. N. and Haug, G. H. (2004), 'Isotopic constraints on glacial/interglacial changes in the oceanic nitrogen budget', *Global Biogeochemical Cycles* **18**(4).

Devol, A. H. (2003), 'Nitrogen cycle: solution to a marine mystery', *Nature* **422**(6932), 575–576.

Devol, A., Uhlenhopp, A., Naqvi, S., Brandes, J., Jayakumar, D., Naik, H., Gaurin, S., Codispoti, L. and Yoshinari, T. (2006), 'Denitrification rates and excess nitrogen gas concentrations in the arabian sea oxygen deficient zone', *Deep Sea Research Part I: Oceanographic Research Papers* **53**(9), 1533–1547.

Dittmar, T. and Birkicht, M. (2001), 'Regeneration of nutrients in the northern benguela upwelling and the angola-benguela front areas: Benefit marine science', *South African Journal of Science* **97**(5 & 6), p–239.

Dore, J. E. and Karl, D. M. (1996), 'Nitrite distributions and dynamics at station aloha', *Deep Sea Research Part II: Topical Studies in Oceanography* **43**(2), 385–402.

Egge, J. and Aksnes, D. (1992), 'Silicate as regulating nutrient in phytoplankton competition.', *Marine ecology progress series. Oldendorf* **83**(2), 281–289.

Ekau, W., Auel, H., Pörtner, H.-O. and Gilbert, D. (2010), 'Impacts of hypoxia on the structure and processes in pelagic communities (zooplankton, macro-invertebrates and fish)', *Biogeosciences* **7**(5), 1669–1699.

EPA, A. (2015), Inventory of us greenhouse gas emissions and sinks: 1990-2013, Technical report, EPA 430-R-15-004.

Faul, K. L., Paytan, A. and Delaney, M. L. (2005), 'Phosphorus distribution in sinking oceanic particulate matter', *Marine Chemistry* **97**(3), 307–333.

Fenchel, T. and Finlay, B. J. (1995), *Ecology and evolution in anoxic worlds*, Oxford University Press; Oxford; New York: Oxford University Press, 1995.

Flohr, A., Van der Plas, A., Emeis, K., Mohrholz, V. and Rixen, T. (2014), 'Spatio-temporal patterns of c: N: P ratios in the northern benguela upwelling system', *Biogeosciences* **11**(3), 885–897.

Franck, V. M., Smith, G. J., Bruland, K. W. and Brzezinski, M. A. (2005), 'Comparison of size-dependent carbon, nitrate, and silicic acid uptake rates in high-and low-iron waters', *Limnology and Oceanography* **50**(3), 825–838.

Füssel, J., Lam, P., Lavik, G., Jensen, M. M., Holtappels, M., Günter, M. and Kuypers, M. M. (2012), 'Nitrite oxidation in the namibian oxygen minimum zone', *The ISME journal* **6**(6), 1200–1209.

Gibson, R. and Atkinson, R. (2003), 'Oxygen minimum zone benthos: adaptation and community response to hypoxia', *Oceanography and Marine Biology: An Annual Review* **41**, 1–45.

Giraudeau, J., Bailey, G. W. and Pujol, C. (2000), 'A high-resolution time-series analyses of particle fluxes in the northern benguela coastal upwelling system: carbonate record of changes in biogenic production and particle transfer processes', *Deep Sea Research Part II: Topical Studies in Oceanography* **47**(9), 1999–2028.

Glaubitz, S., Labrenz, M., Jost, G. and Jürgens, K. (2010), 'Diversity of active chemolithoautotrophic prokaryotes in the sulfidic zone of a black sea pelagic redoxcline as determined by rrna-based stable isotope probing', *FEMS microbiology ecology* **74**(1), 32–41.

Glaubitz, S., Lueders, T., Abraham, W.-R., Jost, G., Jürgens, K. and Labrenz, M. (2009), '13c-isotope analyses reveal that chemolithoautotrophic gamma-and epsilonproteobacteria feed a microbial food web in a pelagic redoxcline of the central baltic sea', *Environmental microbiology* **11**(2), 326–337.

Goreau, T. J., Kaplan, W. A., Wofsy, S. C., McElroy, M. B., Valois, F. W. and Watson, S. W. (1980), 'Production of no2-and n2o by nitrifying bacteria at reduced concentrations of oxygen', *Applied and Environmental Microbiology* **40**(3), 526–532.

Gruber, N. (2004), The dynamics of the marine nitrogen cycle and its influence on atmospheric co2 variations, *in* 'The ocean carbon cycle and climate', Springer, pp. 97–148.

Gruber, N. (2008), 'The marine nitrogen cycle: overview and challenges', *Nitrogen in the marine environment* pp. 1–50.

Gruber, N. and Sarmiento, J. L. (1997), 'Global patterns of marine nitrogen fixation and denitrification', *Global Biogeochemical Cycles* **11**(2), 235–266.

Gutknecht, E., Dadou, I., Marchesiello, P., Cambon, G., Le Vu, B., Sudre, J., Garçon, V., Machu, E., Rixen, T., Kock, A. et al. (2013), 'Nitrogen transfers off walvis bay: a 3-d coupled physical/biogeochemical modeling approach in the namibian upwelling system', *Biogeosciences* **10**, 4117–4135.

Hamersley, M. R., Lavik, G., Woebken, D., Rattray, J. E., Lam, P., Hopmans, E. C., Damsté, J. S. S., Krüger, S., Graco, M., Gutiérrez, D. et al. (2007), 'Anaerobic ammonium oxidation in the peruvian oxygen minimum zone', *Limnology and Oceanography* **52**(3), 923–933.

Hamersley, M. R., Woebken, D., Boehrer, B., Schultze, M., Lavik, G. and Kuypers, M. M. (2009), 'Water column anammox and denitrification in a temperate permanently stratified lake (lake rassnitzer, germany)', *Systematic and applied microbiology* **32**(8), 571–582.

Hansell, D. A., Bates, N. R. and Olson, D. B. (2004), 'Excess nitrate and nitrogen fixation in the north atlantic ocean', *Marine Chemistry* **84**(3), 243–265.

Herbland, A. and Voituriez, B. (1979), 'Hydrological structure analysis for estimating the primary production in the tropical atlantic ocean', *Journal of Marine Research* **37**(1), 87–101.

Honjo, S., Manganini, S. J., Krishfield, R. A. and Francois, R. (2008), 'Particulate organic carbon fluxes to the ocean interior and factors controlling the biological pump: A synthesis of global sediment trap programs since 1983', *Progress in Oceanography* **76**(3), 217–285.

Hutchins, D. A. and Bruland, K. W. (1998), 'Iron-limited diatom growth and si: N uptake ratios in a coastal upwelling regime', *Nature* **393**(6685), 561–564.

Ittekkot, V., Unger, D., Humborg, C. and An, N. T. (2012), *The silicon cycle: human perturbations and impacts on aquatic systems*, Vol. 66, Island Press.

Jarre, A., Hutchings, L., Crichton, M., Wieland, K., Lamont, T., Blamey, L., Illert, C., Hill, E. and Berg, M. (2015), 'Oxygen-depleted bottom waters along the west coast of south africa, 1950–2011', *Fisheries Oceanography* **24**(S1), 56–73.

Jassby, A. D. and Platt, T. (1976), 'Mathematical formulation of the relationship between photosynthesis and light for phytoplankton'.

Jayakumar, D. A., Francis, C. A., Naqvi, S. W. A. and Ward, B. B. (2004), 'Diversity of nitrite reductase genes (nirs) in the denitrifying water column of the coastal arabian sea', *Aquatic Microbial Ecology* **34**(1), 69–78.

Ji, Q., Babbin, A. R., Jayakumar, A., Oleynik, S. and Ward, B. B. (2015), 'Nitrous oxide production by nitrification and denitrification in the eastern tropical south pacific oxygen minimum zone', *Geophysical Research Letters* **42**(24).

Karl, D. and Bjorkman, K. (2001), 'I 13 phosphorus cycle in seawater: Dissolved and particulate pool inventories and selected phosphorus fluxes', *Marine Microbiology* **30**, 239.

Kartal, B., Kuypers, M. M., Lavik, G., Schalk, J., Op den Camp, H. J., Jetten, M. S. and Strous, M. (2007), 'Anammox bacteria disguised as denitrifiers: nitrate reduction to dinitrogen gas via nitrite and ammonium', *Environmental microbiology* **9**(3), 635–642.

Keeling, R. F., Stephens, B. B., Najjar, R. G., Doney, S. C., Archer, D. and Heimann, M. (1998), 'Seasonal variations in the atmospheric o2/n2 ratio in relation to the kinetics of air-sea gas exchange', *Global Biogeochemical Cycles* **12**(1), 141–163.

Kolowith, L. C., Ingall, E. D. and Benner, R. (2001), 'Composition and cycling of marine organic phosphorus', *Limnology and Oceanography* **46**(2), 309–320.

Koné, n. V., Machu, E., Penven, P., Andersen, V., Garçon, V., Fréon, P. and Demarcq, H. (2005), 'Modeling the primary and secondary productions of the southern benguela upwelling system: A comparative study through two biogeochemical models', *Global Biogeochemical Cycles* **19**(4).

Kuypers, M. M., Lavik, G., Woebken, D., Schmid, M., Fuchs, B. M., Amann, R., Jørgensen, B. B. and Jetten, M. S. (2005), 'Massive nitrogen loss from the benguela upwelling system through anaerobic ammonium oxidation', *Proceedings of the National Academy of Sciences of the United States of America* **102**(18), 6478–6483.

Kuypers, M. M., Sliekers, A. O., Lavik, G., Schmid, M., Jørgensen, B. B., Kuenen, J. G., Damsté, J. S. S., Strous, M. and Jetten, M. S. (2003), 'Anaerobic ammonium oxidation by anammox bacteria in the black sea', *Nature* **422**(6932), 608–611.

Lachkar, Z. and Gruber, N. (2012), 'A comparative study of biological production in eastern boundary upwelling systems using an artificial neural network', *Biogeosciences* **9**(1), 293.

Lam, P., Jensen, M. M., Lavik, G., McGinnis, D. F., Müller, B., Schubert, C. J., Amann, R., Thamdrup, B. and Kuypers, M. M. (2007), 'Linking crenarchaeal and bacterial nitrification to anammox in the black sea', *Proceedings of the National Academy of Sciences* **104**(17), 7104–7109.

Lam, P., Lavik, G., Jensen, M. M., van de Vossenberg, J., Schmid, M., Woebken, D., Gutiérrez, D., Amann, R., Jetten, M. S. and Kuypers, M. M. (2009), 'Revising the nitrogen cycle in the peruvian oxygen minimum zone', *Proceedings of the National Academy of Sciences* **106**(12), 4752–4757.

Lampitt, R., Boorman, B., Brown, L., Lucas, M., Salter, I., Sanders, R., Saw, K., Seeyave, S., Thomalla, S. and Turnewitsch, R. (2008), 'Particle export from the euphotic zone: estimates using a novel drifting sediment trap, 234 th and new production', *Deep Sea Research Part I: Oceanographic Research Papers* **55**(11), 1484–1502.

Large, W. G., McWilliams, J. C. and Doney, S. C. (1994), 'Oceanic vertical mixing: A review and a model with a nonlocal boundary layer parameterization', *Reviews of Geophysics* **32**(4), 363–403.

Laruelle, G. G., Roubeix, V., Sferratore, A., Brodherr, B., Ciuffa, D., Conley, D., Dürr, H., Garnier, J., Lancelot, C., Le Thi Phuong, Q. et al. (2009), 'Anthropogenic perturbations of the silicon cycle at the global scale: Key role of the land-ocean transition', *Global biogeochemical cycles* **23**(4).

Lavik, G., Stührmann, T., Brüchert, V., Van der Plas, A., Mohrholz, V., Lam, P., Mußmann, M., Fuchs, B. M., Amann, R., Lass, U. et al. (2009), 'Detoxification of sulphidic african shelf waters by blooming chemolithotrophs', *Nature* **457**(7229), 581–584.

Lipschultz, F., Wofsy, S., Ward, B., Codispoti, L., Friedrich, G. and Elkins, J. (1990), 'Bacterial transformations of inorganic nitrogen in the oxygen-deficient waters of the eastern tropical south pacific ocean', *Deep Sea Research Part A. Oceanographic Research Papers* **37**(10), 1513–1541.

Lipschultz, F., Zafiriou, O. and Ball, L. (1996), 'Seasonal fluctuations of nitrite concentrations in the deep oligotrophic ocean', *Deep Sea Research Part II: Topical Studies in Oceanography* **43**(2), 403–419.

Liu, K.-K., Atkinson, L., Quiñones, R. A. and Talaue-McManus, L. (2010), Biogeochemistry of continental margins in a global context, *in* 'Carbon and Nutrient Fluxes in Continental Margins', Springer, pp. 3–24.

Liu, W. T., Tang, W. and Polito, P. S. (1998), 'Nasa scatterometer provides global ocean-surface wind fields with more structures than numerical weather prediction', *Geophysical Research Letters* **25**(6), 761–764.

Lomas, M. W. and Lipschultz, F. (2006), 'Forming the primary nitrite maximum: Nitrifiers or phytoplankton?', *Limnology and Oceanography* **51**(5), 2453–2467.

Longhurst, A. R. (1991), 'Role of the marine biosphere in the global carbon cycle', *Limnology and Oceanography* **36**(8), 1507–1526.

Madec, G. (2012), 'the nemo team. nemo ocean engine', *Note du Pôle de modélisation, Institut Pierre-Simon Laplace (IPSL), France* (27).

Mahowald, N., Kohfeld, K., Hansson, M., Balkanski, Y., Harrison, S. P., Prentice, I. C., Schulz, M. and Rodhe, H. (1999), 'Dust sources and deposition during the last glacial maximum and current climate: A comparison of model results with paleodata from ice cores and marine sediments', *Journal of Geophysical Research: Atmospheres* **104**(D13), 15895–15916.

Maldonado, M., Navarro, L., Grasa, A., Gonzalez, A. and Vaquerizo, I. (2011), 'Silicon uptake by sponges: a twist to understanding nutrient cycling on continental margins', *Scientific reports* **1**.

McManus, J., Berelson, W. M., Coale, K. H., Johnson, K. S. and Kilgore, T. E. (1997), 'Phosphorus regeneration in continental margin sediments', *Geochimica et Cosmochimica Acta* **61**(14), 2891–2907.

Mohrholz, V., Bartholomae, C., Van der Plas, A. and Lass, H. (2008), 'The seasonal variability of the northern benguela undercurrent and its relation to the oxygen budget on the shelf', *Continental Shelf Research* **28**(3), 424–441.

Mohrholz, V., Schmidt, M. and Lutjeharms, J. (2001), 'The hydrography and dynamics of the angola-benguela frontal zone and environment in april 1999: Benefit marine science', *South African Journal of Science* **97**(5 & 6), p–199.

Monteiro, P. M. and Roychoudhury, A. N. (2005), 'Spatial characteristics of sediment trace metals in an eastern boundary upwelling retention area (st. helena bay, south africa): A hydrodynamic–biological pump hypothesis', *Estuarine, Coastal and Shelf Science* **65**(1), 123–134.

Monteiro, P. M. and van der Plas, A. K. (2006), '5 low oxygen water (low) variability in the benguela system: Key processes and forcing scales relevant to forecasting', *Large Marine Ecosystems* **14**, 71–90.

Monteiro, P., Van Der Plas, A., Melice, J.-L. and Florenchie, P. (2008), 'Interannual hypoxia variability in a coastal upwelling system: Ocean–shelf exchange, climate and ecosystem-

state implications', *Deep Sea Research Part I: Oceanographic Research Papers* **55**(4), 435–450.

Mulder, A., van de Graaf, A. A., Robertson, L. and Kuenen, J. (1995), 'Anaerobic ammonium oxidation discovered in a denitrifying fluidized bed reactor', *FEMS Microbiology Ecology* **16**(3), 177–183.

Muller-Karger, F. E., Varela, R., Thunell, R., Luerssen, R., Hu, C. and Walsh, J. J. (2005), 'The importance of continental margins in the global carbon cycle', *Geophysical Research Letters* **32**(1).

Murphy, J. and Riley, J. P. (1962), 'A modified single solution method for the determination of phosphate in natural waters', *Analytica chimica acta* **27**, 31–36.

Naqvi, S., Yoshinari, T., Brandes, J., Devol, A., Jayakumar, D., Narvekar, P., Altabet, M. and Codispoti, L. (1998), 'Nitrogen isotopic studies in the suboxic arabian sea', *Proceedings of the Indian Academy of Sciences-Earth and Planetary Sciences* **107**(4), 367–378.

Nausch, M. and Nausch, G. (2014), 'Phosphorus speciation and transformation along transects in the benguela upwelling region', *Journal of Marine Systems* **140**, 111–122.

Nelson, D. M., Anderson, R. F., Barber, R. T., Brzezinski, M. A., Buesseler, K. O., Chase, Z., Collier, R. W., Dickson, M.-L., François, R., Hiscock, M. R. et al. (2002), 'Vertical budgets for organic carbon and biogenic silica in the pacific sector of the southern ocean, 1996–1998', *Deep Sea Research Part II: Topical Studies in Oceanography* **49**(9), 1645–1674.

Nelson, D. M., Tréguer, P., Brzezinski, M. A., Leynaert, A. and Quéguiner, B. (1995), 'Production and dissolution of biogenic silica in the ocean: revised global estimates, comparison with regional data and relationship to biogenic sedimentation', *Global Biogeochemical Cycles* **9**(3), 359–372.

Nelson, G. and Hutchings, L. (1983), 'The benguela upwelling area', *Progress in Oceanography* **12**(3), 333–356.

Nevison, C., Butler, J. H. and Elkins, J. (2003), 'Global distribution of n2o and the δn2o-aou yield in the subsurface ocean', *Global Biogeochemical Cycles* **17**(4).

Ostrom, N. E., Russ, M. E., Popp, B., Rust, T. M. and Karl, D. M. (2000), 'Mechanisms of nitrous oxide production in the subtropical north pacific based on determinations of the

isotopic abundances of nitrous oxide and di-oxygen', *Chemosphere-Global Change Science* **2**(3), 281–290.

Oudot, C., Jean-Baptiste, P., Fourré, E., Mormiche, C., Guevel, M., Ternon, J.-F. and Le Corre, P. (2002), 'Transatlantic equatorial distribution of nitrous oxide and methane', *Deep Sea Research Part I: Oceanographic Research Papers* **49**(7), 1175–1193.

Paytan, A. and McLaughlin, K. (2007), 'The oceanic phosphorus cycle', *Chemical reviews* **107**(2), 563–576.

Penven, P., Lutjeharms, J. and Florenchie, P. (2006), 'Madagascar: A pacemaker for the agulhas current system?', *Geophysical Research Letters* **33**(17).

Pondaven, P., Ragueneau, O., Tréguer, P., Hauvespre, A., Dezileau, L. and Reyss, J. L. (2000), 'Resolving the opal paradoxin the southern ocean', *Nature* **405**(6783), 168–172.

Rae, C. D. (2005), 'A demonstration of the hydrographic partition of the benguela upwelling ecosystem at 26 40's', *African Journal of Marine Science* **27**(3), 617–628.

Ragueneau, O., Regaudie-de Gioux, A., Moriceau, B., Gallinari, M., Vangriesheim, A., Baurand, F. and Khripounoff, A. (2009), 'A benthic si mass balance on the congo margin: Origin of the 4000m dsi anomaly and implications for the transfer of si from land to ocean', *Deep Sea Research Part II: Topical Studies in Oceanography* **56**(23), 2197–2207.

Redfield, A., Ketchum, B. and Richards, F. (1963), 'The influence of organisms on the composition of seawater, the sea, the composition of sea water: Comparative and descriptive oceanography, 2 mn hill, 26–77'.

Reffray, G., Bourdalle-Badie, R. and Calone, C. (2015), 'Modelling turbulent vertical mixing sensitivity using a 1-d version of nemo', *Geoscientific Model Development* **8**(1), 69–86.

Richards, F. A. (1966), *Chemical observations in some anoxic, sulfide-bearing basins and fjords*, Department of Oceanography, University of Washington.

Risien, C. M. and Chelton, D. B. (2008), 'A global climatology of surface wind and wind stress fields from eight years of quikscat scatterometer data', *Journal of Physical Oceanography* **38**(11), 2379–2413.

Romero, O., Boeckel, B., Donner, B., Lavik, G., Fischer, G. and Wefer, G. (2002), 'Seasonal productivity dynamics in the pelagic central benguela system inferred from the flux of carbonate and silicate organisms', *Journal of Marine Systems* **37**(4), 259–278.

Ruttenberg, K. C. and Dyhrman, S. T. (2005), 'Temporal and spatial variability of dissolved organic and inorganic phosphorus, and metrics of phosphorus bioavailability in an upwelling-dominated coastal system', *Journal of Geophysical Research: Oceans* **110**(C10).

Ryther, J. H. and Dunstan, W. M. (1971), 'Nitrogen, phosphorus, and eutrophication in the coastal marine environment', *Science* **171**(3975), 1008–1013.

Sakshaug, E., Bricaud, A., Dandonneau, Y., Falkowski, P. G., Kiefer, D. A., Legendre, L., Morel, A., Parslow, J. and Takahashi, M. (1997), 'Parameters of photosynthesis: definitions, theory and interpretation of results', *Journal of Plankton Research* **19**(11), 1637–1670.

Salter, I., Lampitt, R. S., Sanders, R., Poulton, A., Kemp, A. E., Boorman, B., Saw, K. and Pearce, R. (2007), 'Estimating carbon, silica and diatom export from a naturally fertilised phytoplankton bloom in the southern ocean using pelagra: a novel drifting sediment trap', *Deep Sea Research Part II: Topical Studies in Oceanography* **54**(18), 2233–2259.

Schmid, M. C., Risgaard-Petersen, N., Van De Vossenberg, J., Kuypers, M. M., Lavik, G., Petersen, J., Hulth, S., Thamdrup, B., Canfield, D., Dalsgaard, T. et al. (2007), 'Anaerobic ammonium-oxidizing bacteria in marine environments: widespread occurrence but low diversity', *Environmental microbiology* **9**(6), 1476–1484.

Schmidtko, S., Stramma, L. and Visbeck, M. (2017), 'Decline in global oceanic oxygen content during the past five decades', *Nature* **542**(7641), 335–339.

Schunck, H., Lavik, G., Desai, D. K., Großkopf, T., Kalvelage, T., Löscher, C. R., Paulmier, A., Contreras, S., Siegel, H., Holtappels, M. et al. (2013), 'Giant hydrogen sulfide plume in the oxygen minimum zone off peru supports chemolithoautotrophy', *PLoS One* **8**(8), e68661.

Shannon, L. and Nelson, G. (1996), The benguela: large scale features and processes and system variability, *in* 'The South Atlantic', Springer, pp. 163–210.

Shannon, L. V. (1985), 'The benguela ecosystem. i: Evolution of the benguela physical features and processes', *Oceanography and Marine Biology* **23**, 105–182.

Shannon, V., Hempel, G., Moloney, C., Woods, J. D. and Malanotte-Rizzoli, P. (2006), *Benguela: predicting a large marine ecosystem*, Vol. 14, Elsevier.

Shchepetkin, A. F. and McWilliams, J. C. (2005), 'The regional oceanic modeling system (roms): a split-explicit, free-surface, topography-following-coordinate oceanic model', *Ocean Modelling* **9**(4), 347–404.

Shipe, R. F. and Brzezinski, M. A. (2001), 'A time series study of silica production and flux in an eastern boundary region: Santa barbara basin, california', *Global Biogeochemical Cycles* **15**(2), 517–531.

Steinberg, D. K. and Landry, M. R. (2017), 'Zooplankton and the ocean carbon cycle', *Annual Review of Marine Science* **9**, 413–444.

Stramma, L., Johnson, G. C., Sprintall, J. and Mohrholz, V. (2008), 'Expanding oxygen-minimum zones in the tropical oceans', *science* **320**(5876), 655–658.

Stramma, L., Schmidtko, S., Levin, L. A. and Johnson, G. C. (2010), 'Ocean oxygen minima expansions and their biological impacts', *Deep Sea Research Part I: Oceanographic Research Papers* **57**(4), 587–595.

Strickland, J. D. and Parsons, T. R. (1972), 'A practical handbook of seawater analysis'.

Strous, M., Van Gerven, E., Zheng, P., Kuenen, J. G. and Jetten, M. S. (1997), 'Ammonium removal from concentrated waste streams with the anaerobic ammonium oxidation (anammox) process in different reactor configurations', *Water Research* **31**(8), 1955–1962.

Suntharalingam, P., Buitenhuis, E., Le Quéré, C., Dentener, F., Nevison, C., Butler, J. H., Bange, H. W. and Forster, G. (2012), 'Quantifying the impact of anthropogenic nitrogen deposition on oceanic nitrous oxide', *Geophysical Research Letters* **39**(7).

Suntharalingam, P., Sarmiento, J. and Toggweiler, J. (2000), 'Global significance of nitrous-oxide production and transport from oceanic low-oxygen zones: A modeling study', *Global Biogeochemical Cycles* **14**(4), 1353–1370.

Sutka, R. L., Ostrom, N., Ostrom, P., Breznak, J., Gandhi, H., Pitt, A. and Li, F. (2006), 'Distinguishing nitrous oxide production from nitrification and denitrification on the basis of isotopomer abundances', *Applied and environmental microbiology* **72**(1), 638–644.

Taylor, K. E. (2001), 'Summarizing multiple aspects of model performance in a single diagram', *Journal of Geophysical Research: Atmospheres* **106**(D7), 7183–7192.

Thamdrup, B., Dalsgaard, T., Jensen, M. M., Ulloa, O., Farías, L. and Escribano, R. (2006), 'Anaerobic ammonium oxidation in the oxygen-deficient waters off northern chile', *Limnology and Oceanography* **51**(5), 2145–2156.

Tréguer, P. J. and De La Rocha, C. L. (2013), 'The world ocean silica cycle', *Annual review of marine science* **5**, 477–501.

Treguer, P., Nelson, D. M., Van Bennekom, A. J., DeMaster, D. J. et al. (1995), 'The silica balance in the world ocean: a reestimate', *Science* **268**(5209), 375.

Tyrrell, T. (1999), 'The relative influences of nitrogen and phosphorus on oceanic primary production', *Nature* **400**(6744), 525–531.

Tyrrell, T. and Lucas, M. I. (2002), 'Geochemical evidence of denitrification in the benguela upwelling system', *Continental Shelf Research* **22**(17), 2497–2511.

Van Bennekom, A. and Berger, G. (1984), 'Hydrography and silica budget of the angola basin', *Netherlands Journal of Sea Research* **17**(2-4), 149–200.

Van Cappellen, P., Dixit, S. and van Beusekom, J. (2002), 'Biogenic silica dissolution in the oceans: Reconciling experimental and field-based dissolution rates', *Global Biogeochemical Cycles* **16**(4).

Van de Graaf, A. A., Mulder, A., de Bruijn, P., Jetten, M., Robertson, L. A. and Kuenen, J. G. (1995), 'Anaerobic oxidation of ammonium is a biologically mediated process.', *Applied and environmental microbiology* **61**(4), 1246–1251.

Van Mooy, B. A., Keil, R. G. and Devol, A. H. (2002), 'Impact of suboxia on sinking particulate organic carbon: Enhanced carbon flux and preferential degradation of amino acids via denitrification', *Geochimica et Cosmochimica Acta* **66**(3), 457–465.

Veitch, J., Penven, P. and Shillington, F. (2009), 'The benguela: A laboratory for comparative modeling studies', *Progress in Oceanography* **83**(1), 296–302.

Vichi, M., Cossarini, G., Gutierrez, M., Lazzari, P., Lovato, T., Mattia, G., Masina, S., McKiver, W., Pinardi, N., Solidoro, C. et al. (2015), 'The biogeochemical flux model (bfm): Equation description and user manual', *BFM Consortium, Bologna, Italy* .

Vichi, M., Pinardi, N. and Masina, S. (2007), 'A generalized model of pelagic biogeochemistry for the global ocean ecosystem. part i: Theory', *Journal of Marine Systems* **64**(1), 89–109.

Wanninkhof, R. (1992), 'Relationship between wind speed and gas exchange over the ocean', *Journal of Geophysical Research: Oceans (1978–2012)* **97**(C5), 7373–7382.

Ward, B., Devol, A., Rich, J., Chang, B., Bulow, S., Naik, H., Pratihary, A. and Jayakumar, A. (2009), 'Denitrification as the dominant nitrogen loss process in the arabian sea', *Nature* **461**(7260), 78–81.

Ward, B., Olson, R. J. and Perry, M. J. (1982), 'Microbial nitrification rates in the primary nitrite maximum off southern california', *Deep Sea Research Part A. Oceanographic Research Papers* **29**(2), 247–255.

Wasmund, N., Nausch, G. and Hansen, A. (2014), 'Phytoplankton succession in an isolated upwelled benguela water body in relation to different initial nutrient conditions', *Journal of Marine Systems* **140**, 163–174.

Wasmund, N., Struck, U., Hansen, A., Flohr, A., Nausch, G., Grüttmüller, A. and Voss, M. (2015), 'Missing nitrogen fixation in the benguela region', *Deep Sea Research Part I: Oceanographic Research Papers* **106**, 30–41.

Weeks, S. J., Currie, B. and Bakun, A. (2002), 'Satellite imaging: Massive emissions of toxic gas in the atlantic', *Nature* **415**(6871), 493–494.

Woebken, D., Lam, P., Kuypers, M. M., Naqvi, S., Kartal, B., Strous, M., Jetten, M. S., Fuchs, B. M. and Amann, R. (2008), 'A microdiversity study of anammox bacteria reveals a novel candidatus scalindua phylotype in marine oxygen minimum zones', *Environmental Microbiology* **10**(11), 3106–3119.

Wollast, R. (1983), 'The global cycle of silica', *Silicon geochemistry and biogeochemistry* pp. 39–76.

Yakushev, E., Pollehne, F., Jost, G., Kuznetsov, I., Schneider, B. and Umlauf, L. (2007), 'Analysis of the water column oxic/anoxic interface in the black and baltic seas with a numerical model', *Marine Chemistry* **107**(3), 388–410.

Yakushev, E. V. and Neretin, L. N. (1997), 'One-dimensional modeling of nitrogen and sulfur cycles in the aphotic zones of the black and arabian seas', *Global Biogeochemical Cycles* **11**(3), 401–414.

Zehr, J. P., Waterbury, J. B., Turner, P. J., Montoya, J. P., Omoregie, E., Steward, G. F., Hansen, A. and Karl, D. M. (2001), 'Unicellular cyanobacteria fix n2 in the subtropical north pacific ocean', *Nature* **412**(6847), 635–638.

Zumft, W. G. (1997), 'Cell biology and molecular basis of denitrification.', *Microbiology and molecular biology reviews* **61**(4), 533–616.

Appendix

The variables and parameters presented here are for the BFM model and include the new variables introduced in this study. For full description of BioEBUS state variables and parameters please refer to Gutknecht et al. (2013) as these were not changed in this study.

Table 6.1: BFM biogeochemical state variables, initial values and used for the sumilation and depth scales as set in the BFM_general namelist.

Symbol	Variable	Units	Initial values	Scale depth [m]
N1p	Phosphate	mmol P m^{-3}	CARS[a]	
N2n	Nitrite	mmol N m^{-3}	0.6[d]	
N3n	Nitrate	mmol N m^{-3}	CARS[a]	
N4n	Ammonium	mmol N m^{-3}	0.1	
N5s	Silicate	mmol Si m^{-3}	CARS[a]	
N7f	Iron	μmol Fe m^{-3}	0.05	
O2n	Oxygen	mmol O_2 m^{-3}	CARS[a]	
O5n	Nitrous oxide	mmol N m^{-3}	$(f^o_{O^5})$[ab]	
O3c	Inorganic Carbon	mg C m^{-3}	WOA[c]	
O3h	Total Alkalinity	mmol Eq m^{-3}	WOA[c]	
P1c	Diatoms	mg C m^{-3}	0.01	
P2c	Nanoflagellates	mg C m^{-3}	0.01	
P3c	Picophytoplankton	mg C m^{-3}	0.01	
P4c	Large Phytoplankton	mg C m^{-3}	0.01	
Z3c	Carnivorous Mesozooplankton	mg C m^{-3}	0.01	
Z4c	Omnivorous Mesozooplankton	mg C m^{-3}	0.01	
Z5c	Microzooplankton	mg C m^{-3}	0.01	
Z6c	Heterotrophic flagellates	mg C m^{-3}	0.01	
B1c	Pelagic Bacteria	mg C m^{-3}	0.01	
R1c	Labile DOM	mg C m^{-3}	0.01	
R2c	Semi-labile DOM	mg C m^{-3}	0.01	
R3c	Semi-refractory DOM	mg C m^{-3}	0.01	
R6c	Particulate Organic Detritus	mg C m^{-3}	0.01	

[a] CARS 2009 data.

[ab] Computed as $(f^o_{O^5})$ of oxygen from CARS using the parametization of Suntharalingam et al. (2000).

[c] WOA PISCES data for ROMSTOOLS

[d] MSM 19/1b

Table 6.2: Description of phytoplankton parameters and values described in the BFM equations. These parameters are controlled with the Pelagic_Ecology namelist.

Symbol	Code	Variable	Units	Values P1 P2 P3 P4
$r0_p$	p_sum	Maximum specific photosynthetic rate	d^{-1}	2.0 2.5 3.0 0.75
h_p^n	p_lN4	Half saturation for NH_4 uptake	mmol N-NH4 m^{-3}	1.0 1.0 0.0 1.0
n_p^{min}	p_qnlc	minimum nitrogen quota	10^{-3} mmolN mgC^{-1}	4.193 4.193 4.193 6.870
n_p^{opt}	p_qncPPY	optimal nitrogen quota	10^{-2} mmolN mgC^{-1}	1.26 1.26 1.26 1.26
	p_xqn	Multiplication factor for luxury storage	-	2.0 2.0 2.0 2.0
	p_xqn*p_qncPPY	maximum nitrogen quota	10^{-2} mmolN mgC^{-1}	
n_p^{opt}	p_qncPPY	optimal nitrogen quota	10^{-2} mmolN mgC^{-1}	1.26 1.26 1.26 1.26
n_p^{opt}	p_qncPPY	optimal nitrogen quota	10^{-2} mmolN mgC^{-1}	1.26 1.26 1.26 1.26
a_1	p_qup	Specific affinity constant for P	m^3 mg C^{-1} d^{-1}	0.025 0.025 0.25 0.025
p_p^{min}	p_qplc	minimum phosphorus quota	10^{-4} mmolP mg C^{-1}	1.80 1.80 1.80 4.29
p_p^{opt}	p_qpcPPY	optimal phosphorus quota	10^{-4} mmolP mg C^{-1}	7.86 7.86 7.86 7.86
	p_xqp	Multiplication factor for luxury storage	-	2.0 2.0 2.0 2.0
	p_xqp*p_qpcPPY	maximum phosphorus quota	mmolP mg C^{-1}	
	p_switchSi	switch for parametization of silicate limitation	-	1 0 0 0
	p_xqp*p_qpcPPY	maximum phosphorus quota	mmolP mg C^{-1}	
s_p^{opt}	p_qscPPY	optimal Si:C ratio in silicifiers	mmolSi mg C^{-1}	0.01 0.0 0.0 0.0
α_{chl}^0	p_alpha_chl	maximum light utilization coefficient	10^{-5} mgC(mg chl)$^{-1}$ μE^{-1} m^2	1.38 0.46 1.52 0.68
v_p	p_ruELiPPY	Relaxation rate towards the optimal light	d−1	0.2 0.25 0.3 0.15

Table 6.3: Description of chemical stoichiometric coefficients and parameters associated with pelagic variables in BFM.

Symbol	Code	Variable	Units	Values
Ω_c^o	MW_C	Unit conversion factor and soichiometric coefficient	$mmolO_2\ mgC^{-1}$	
Ω_c^n	p_qon_nitri	Stoichiometric coefficient for nitrification	$mmolO_2\ mmolN^{-1}$	
$\tilde{\Omega}_n^O$	p_qon_dentri	Stoichiometric coefficient for denitrification	$mmolO_2\ mmolN^{-1}$	
Ω_n^r	p_qro	Stoichiometric coefficient for oxic-anoxic reaction	$mmolHS^-\ mmolO_2\ ^{-1}$	
Λ_{N4}^{nit}	-	Specific nitrification rate for NH_4	d^{-1}	0.9
Λ_{N2}^{nit}	-	Specific nitrification rate for NO_2	d^{-1}	2.5
Q_{10_n}	p_qro*p_qon_dentri	Q10 factor for nitrification/denitrification	-	
h_o	p_clO2o	Half saturation oxygen concentration for anoxic processes	$mmolO_2\ m^{-3}$	1.0
h_r	p_clN6r	Half saturation for chemical processes	$mmolHS^-\ m^{-3}$	1.0
Λ_{N3}^{denit}	p_sN3O4n	Specific denitrification rate	d^{-1}	0.35
$\mathscr{M}_o^*$	p_rPAo	Reference anoxic mineralization	$mmol\ O_2\ m^{-3}\ d^{-1}$	1.0
$_{N6}^{reox}$	p_rOS	Specific reoxidation rate reduction equivalents	d^{-1}	0.05

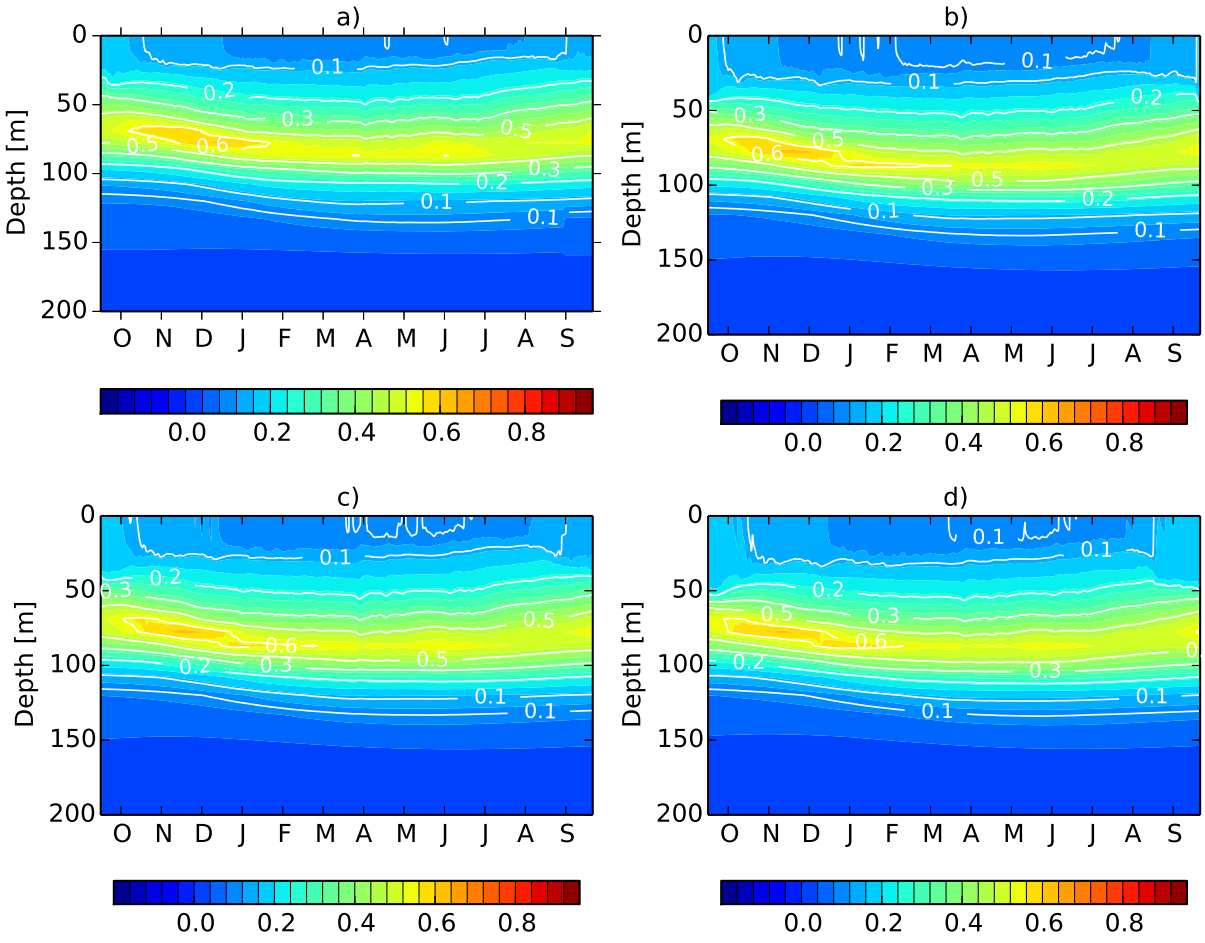

Figure 6.8: Simulated chlorophyll concentrations [mg Chl m^{-3}] for station (a) N1DB01, (b) N1DB02, (c) N1DB03 and (d) N1DB04.